Graz University of Technology

Institute for Computer Graphics and Vision, Graz University of Technology

Division of Vascular and Interventional Radiology, Medical University of Graz

Dissertation

Techniques for Interdisciplinary Validation by Visualization in Physiological Modeling Liver Radiofrequency Ablation

---

Judith K. Muehl

Graz, Austria, October 12, 2010

Thesis supervisors

Prof. Dr. Schmalstieg

Prof. Dr. Portugaller

To my father.
I would have loved to have been able to present this thesis to him in person.

Deutsche Fassung:
Beschluss der Curricula-Kommission für Bachelor-, Master- und Diplomstudien vom 10.11.2008
Genehmigung des Senates am 1.12.2008

EIDESSTATTLICHE ERKLÄRUNG

Ich erkläre an Eides statt, dass ich die vorliegende Arbeit selbstständig verfasst, andere als die angegebenen Quellen/Hilfsmittel nicht benutzt, und die den benutzten Quellen wörtlich und inhaltlich entnommene Stellen als solche kenntlich gemacht habe.

Graz, am ……. ……..
(Unterschrift)

Englische Fassung:

STATUTORY DECLARATION

I declare that I have authored this thesis independently, that I have not used other than the declared sources / resources, and that I have explicitly marked all material which has been quoted either literally or by content from the used sources.

……. ……..
date (signature)

Abstract

Radiofrequency ablation is a minimally invasive tumor therapy. In this intervention a needle electrode is inserted into the tumor and the tissue around it is heated up. The aim is to destroy the tumor with a safety margin, but with minimal damage to surrounding healthy tissue. Though the intervention is nowadays performed in clinical practice, its result is hard to predict and success can only be proven in follow-up examinations. Computer support in predicting the outcome of the intervention is therefore highly desirable.

The intervention is planned based on radiological images, with regard to patient anatomy, but it also depends highly on physiology. A prediction therefore demands a computational model solving a complex mathematical system of partial differential equations in three dimensions. For the application case the model used has to be validated to compute correctly. In other words, the model has to convince the medical community that it can predict the outcome of the intervention correctly. This thesis deals with the validation research question on the example of radiofrequecy ablation for liver tumors.

As the research question is highly interdisciplinary a concept for validation of the result is tackled by visual comparison of the prediction simulation to findings from an animal study. Single achievements presented in this thesis therefore concern a visualization tool for multi-volume raycasting (volumetric rendering), a mathematical model for the radiofrequency ablation process with prediction of effects for needle misplacement, a data acquisition protocol for the animal study which allows the use of state-of-the-art image processing tools to gain a virtual liver model suitable for the validation task. Furthermore, first results for comparing the outcome of the intervention as visible in histologies with its radiological equivalent are presented. The combination leads to an interdisciplinary validation tool chain for the research question approached.

Keywords: Radiofrequency ablation, virtual physiological liver, validation by visualization, mathematical modeling, computer oriented medical data acquisition

Acknowledgments

First I want to thank my primary thesis supervisor Dieter Schmalstieg for giving me the opportunity of working independently on a research subject of my choice. I was able to carry out the work in his research group and I thank him for such tolerance with regard to my chosen thesis topic.

Second, I thank my secondary supervisor Horst Portugaller for his support. He supported my desire to have an animal study for computational validation purposes although the study idea was mine. Horst performed the interventions on the pigs and was, so to speak, the main actor in the animal study. I also thank Philipp Stiegler for his efforts in organizing the animal study as well as the histology preparations. I did not know how much effort is involved in an animal study — let alone the histological sectioning — when I asked for the study. Philipp and Horst made it possible.

Many thanks to Rostislav Khlebnikov and Bernhard Kainz for all the support they gave in our joint work — to Rostislav also for helping me to handle some important figures needed at the last minute and to Bernhard for providing me with such a lot ancillary knowledge of so many details. I thank Philip Voglreiter and Johannes Fasching for their great support in the time consuming manual work. I also want to thank Eddie Fulford for copy editing my thesis. Furthermore, my thanks go to everybody who supported this work — Philipp Stiegler's helpful team, the medical assistants, and the interview partners.

I am indepted to my parents for their taking care of me and for backing me up in every idea I had. Nobody could have given me better support. I also thank my sister Ina Arndt-Fabian as well as Claudia Koegel, Peter Weinberger, Silke Rauterkus and Klaus Mueller for very many constructive discussions on the telephone. My heartfelt thanks; I do not know how I would have managed difficult times without their unstinted support.

The work presented here was funded by EU under contract number MRTN-CT-2004-512400 and also in the VPH initiative in FP7 under contract number 223877.

Contents

List of Figures

List of Tables

Chapter 1

Introduction

Contents

This thesis presents an interdisciplinary approach to validating a computational prediction for a medical intervention. As a sample application we chose radiofrequency ablation, as it is performed in clinical practice and is also an ongoing medical research topic. Our application case focuses on tumors occuring in the liver.

1.1 Computer support for medical interventions

In clinical practice, medical interventions are planned and performed with very limited support by computers. This is often mourned by all participants involved in the process. Patients would like to benefit from technological advances and look forward to better treatment. Physicians look forward to better tools to heal the patients. Health insurance agencies and governments are mainly interested in lowering costs. Computer scientists, mathematicians as well as biomedical engineers see an application area where their knowledge and contributions can impact real life. Support by computer can look very different in detail for very different application cases. From organizing a hospital, patient records,

and medical data on a chip card to supporting clinical interventions, very different application cases are under development. We focused on supporting the planning process for one intervention as performed in clinical practice. Ideally, the result of an intervention should be predictable before the intervention is performed.

Planning an intervention most often relies on general information about the patient as well as on medical images showing anatomical structures. There exists a wide variety of imaging techniques and possibilities — for which some use images of physiological aspects. In addition other measurements exist which allow examination of the patient and give an all inclusive overview of the patient. When the outcome of an intervention is in large part influenced by patient physiology and not anatomy alone, this physiological information has to be included in the planning process. This information is either provided by some measurement or else provided by the knowledge of the physician. Otherwise it presents a gap which hinders the intervention planning with a factor of unpredictability.

For an intervention which is planned nowadays based on anatomical images, planning with incorporated physiological aspects means including and processing additional information. From a technical, computer science, and engineering perspective, physiological planning means adding functionality to the imaged geometry. It also means adding interpretation of acquired images. This thesis contributes to planning the medical application of radiofrequency ablation performed on liver tumors. This intervention is planned using Computed Tomogram (CT) images. The outcome of the intervention is heavily influenced by factors not visible in anatomical images and is therefore hard to predict. The result cannot be seen in images acquired during patient treatment. The task of supporting this clinical intervention with an intervention prediction system involves specialists from very different research areas. It therefore demands a highly interdisciplinary approach.

1.2 The liver as a sample organ

The liver is an organ situated in the abdomen. On one side, it is involved in the metabolism cleansing the blood, on the other side, taking nutrients from the digestive system for further processing.

1.2.1 On a macroscopic scale

From an anatomical point of view the liver itself is supplied with oxygen rich blood through the hepatic artery. The nutritient rich blood from the digestive tract flows into the liver

through the portal vein. All blood flowing through the liver leaves the organ through the hepatic vein. So the organ has three blood vessel connections to the rest of the body and three vessel trees. One of the functions of the liver is the production of bile, which is needed in the digestive tract especially for fat metabolism. The bile produced is collected in the gall bladder and provided to the intestine on demand. So besides parenchyma and the three vessel trees, bile ducts also go through the whole liver. Figure 1.1 shows a schematic diagram of a human liver with all three vessel trees as well as the bile ducts with the gall bladder.

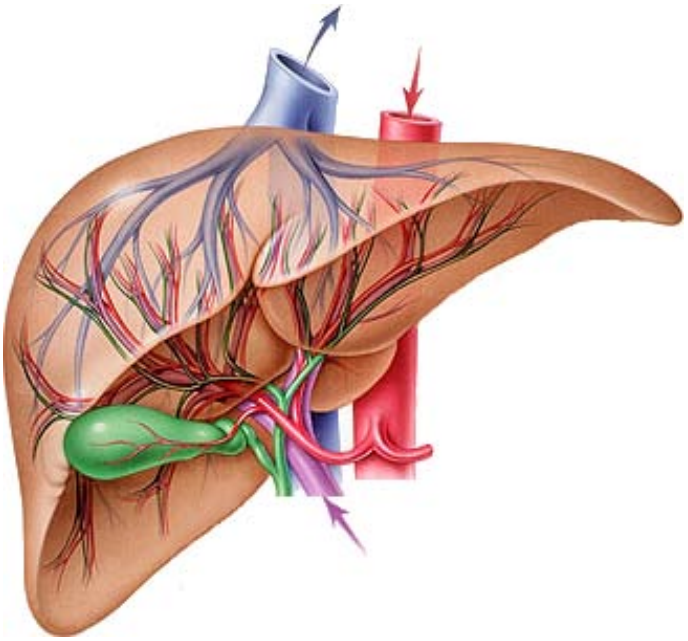

Figure 1.1: Liver schematic for a human liver: The organ has three vessel trees and the bile ducts. Image adapted from *mauritius images/Phototake*.

From an anatomical point of view, the liver is divided into eight liver segments. These segments are oriented on their connection to the portal vein. An anatomical resection aims at dissecting complete segments. For our target intervention — radiofrequency ablation — the orientation on liver segments is unimportant and merely serves as a description and communicates locations in the liver.

1.2.2 On a microscopic scale

On a microscopic scale, the liver appears different. Liver lobules consisting mainly of hepatocytes are separated by connective tissue. The blood vessels in the liver branch into

vessels with smaller diameters. At the vertices of the lobules, portal triads are located holding branches of the portal vein, together with bile ducts and branches of the hepatic artery. In the center of a lobule a branch of the hepatic vein is located. Figure 1.2 shows a schematic representation of liver tissue as seen under a microscope.

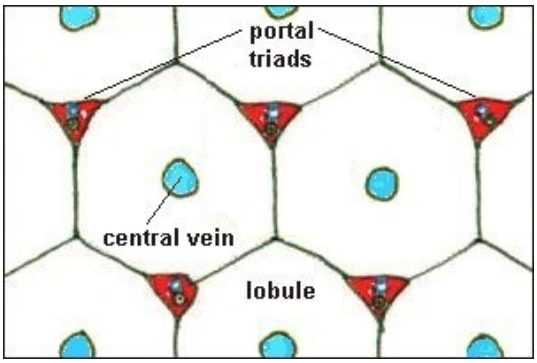

Figure 1.2: On a microscopic level the liver lobules are the basic structure of the liver tissue. The bile ducts, hepatic artery, and portal vein end in portal triads. The central veins lead back to the hepatic vein. Image adapted from *Pathophysiology of the Digestive System*[25].

So the same organ appears very different in visible structures on different scales. Combining information together from both scales in one computer model is therefore often desired. On the medical computer vision side this fusion has been researched many times before for different tissues.

1.3 Radiofrequency ablation of liver tumors

For tumors in the liver, Radiofrequency Ablation (RFA) presents an alternative treatment, if surgical therapy is not possible. It is a minimally invasive treatment and can be performed percutaneously. The interventionalist places a needle through the skin into the liver tumor and uses a Radiofrequency (RF) generator to coagulate the tissue around this electrode, thereby destroying the malignancy. For this treatment, a patient's stay in hospital rarely exceeds two days compared to more than one week when tumor resection is performed. The advantages are obvious: lower risks for the patients, no peri- or post-operative side-effects including scars, adhesions or even intra-operative death, and health insurance agencies face significantly shorter hospital stay. However, this form of therapy still has major drawbacks: the exact extension of the necrosis zone is hard to plan and almost impossible to monitor. Assessment of the results during or right after the procedure is very limited.

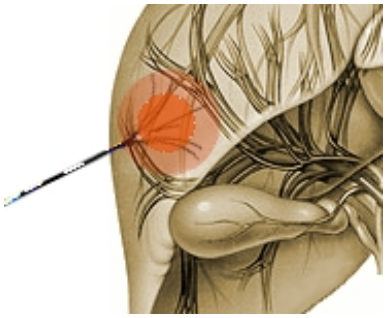

Figure 1.3: Diagram showing RFA in the liver: A needle electrode is placed inside the liver and the tissue is heated up.

In this intervention, the malignancy is destroyed through intensive heating. Heating has a strong influence on perfusion of tissue, reaction rates in chemical processes, as well as the organ's and overall system's health. Local hyperthermia can be used to kill a limited number of cells while keeping surrounding parts vital and healthy. RFA is used in clinical practice in a variety of organs (liver, kidneys, lung, bones, or brain). In this thesis we focus on the application in the liver.

Locally heating tissue by applying radiofrequency electromagnetic waves destroys a small volume of cells. The aim is to destroy the complete tumor with a safety margin, without destroying surrounding vital structures (heart, stomach, etc.) and without causing thrombosis in nearby blood vessels. Still, when the tissue is heated up, so are the vessels in the tissue and the blood they carry during the time of the intervention. The blood perfusion thereby takes away heat from the heated up area — the so called heat sink effect. When cells do not become hot enough over a sufficiently long time, they do not die. So parts of the tissue in the planned ablation zone might survive. The cooling effect is the major, but not the only effect determining size and shape of the coagulation and the resulting necrosis zone. Other factors consist, for example, of patient specific heat conductivity of the tissue. Predicting the outcome of the intervention can be achieved by computational simulation. Though different models for this process exist, none of them has been experimentally validated.

1.4 Research hypothesis

This thesis deals with elaborating a concept for the validation of treatment simulation for the complete medical procedure. We present implemented tools to solve the engineering challenges. So the overall research hypothesis presents itself as:

Hypothesis: *For a physiological intervention, such as RFA in the liver, where the result cannot be imaged or assembled from complete knowledge of single effects, the result can be predicted and the prediction validated by visually comparing the computational prediction with findings in an animal study.*

The research hypothesis in itself presents a highly interdisciplinary approach to the topic. This fact already raises major difficulties, where solutions have to be elaborated to communicate successfully in a group working on a task such as this. The major weakness of all prediction systems is the validation of the predictive power of the model. For an interdisciplinary research task, this validation has to be achieved convincingly for all participating disciplines. So a visual comparison of the computed prediction with the real intervention result is the best method of communication to convince every participant of the solution's advantages and drawbacks. The question of establishing a suitable biomedical model is not part of the hypothesis and lies out of the scope of this thesis.

1.5 Contributions

With this thesis we present for the first time a systematical evaluation of different research methodologies and inherent differences in an interdisciplinary project aiming at simulating the radiofrequency ablation process. The case study furthermore looks into the challenges for communication and collaboration arising from the interdisciplinary approach. The innovation also concerns solutions presented for the difficulties arising. This material is presented in Chapter 3.

Computationally predicting the result of an RFA intervention is an ongoing research question. Publications on this topic originate from different research groups with different foci. The Imppact project as an interdisciplinary approach to predicting and modeling RFA is a contribution in itself. Furthermore, the approach to gain validation in the interdisciplinary context of the complete model is unique and unseen in other projects concerning this topic. These innovations are presented in Chapter 4.

Experimental validation for the predictive power of a planning application demands comparison of the planning application's prediction with treatment results. Due to the interdisciplinary nature of the task, the validation can only convince researchers of all participating disciplines if the result is presented in a graphical visualization. So a tool allowing interactive visualization of volumes and intersecting polygonal structures has been created. The first innovative step in this direction was taken when the Multi-*

raycaster was envisioned, and the first solution elaborated. Further progress led to a unique, fast, and flexible multi-* raycasting system which allows processing of constructive solid geometry operations on volumes and polygonal models as well. These novelties form the basis for the visual validation step and are presented in Chapter 5.

A computational model for the RFA process has been elaborated. The model is based on an existing computational model, but enhanced to fit the RITA RFA system. It is the first model simulating the extendable RITA needle with its extension protocol. The model is furthermore applied to a real world situation of misplaced needle electrodes together with different perfusion rates for tumors and liver tissue. This examination is the first one on this topic. The model details and its application to examinations can be found in Chapter 6.

The experimental validation also demands establishing a reference model in an animal study, where the result of the medical intervention can be compared to the prediction. Building the reference model — the intervention specific virtual liver — from CT scans is another important contribution made in this thesis. This goal was achieved by changing an existing method in radiology (a standard CT protocol) due to engineering needs, thereby incorporating engineering methodology. So this is not only an example of interdisciplinary research as defined in the literature and explained in the context of interdisciplinarity (see Chapter 3), but is also a completely new and innovative approach to combine experimental validation as formed in natural sciences with the engineering methodology. We look into these steps and facts in Chapter 7.

While treatment planning is based on radiological images, the intervention's result concerns cell death in a tissue and can therefore only be determined by histological examinations. So it cannot be reliably imaged radiologically. We gain information on size and shape of the necrosis zone from histological examinations, by forming a 3D volume out of the sections. The computer oriented approach to fixing the tissue, producing a stack of histological sections each one a slightly different layer, the alternating coloring to gain information on more than one feature in the tissue block as well as the approach towards combining histological and CT volume data are innovations. Chapter 8 shows these aspects in detail.

Our very important research hypothesis is new and solved for the first time with this thesis. The validation across multiple disciplines ensures trust in the prediction system from all those participlating. All parts presented here together form the first joint interdisciplinary validation strategy and set of tools. Especially in medical treatment planning,

a validation of predicted results is mandatory but is rarely achieved satisfactorily.

1.6 Collaboration statement

This thesis has been accompanied by a project proposal and intermediate publications made along the way. Most important steps are presented in

- **Data Acquisition for Radiofrequency Ablation Simulation**, J. K. Muehl, in *New Technology Frontiers in Minimally Invasive Therapies*, Lupiensis Biomedical Publications, ISBN 978-88-902880-1-2, pp. 27–34, 2007: Describes a feasability study on how to gain the data required for model validation from normal patient treatment. This material is part of Chapter 7.

- **Constructing Verifiable Models for Radiofrequency Ablation Simulation**, J. K. Muehl, in *Minimally Invasive Technologies and Nanosystems for Diagnosis and Therapies*, Lupiensis Biomedical Publications, ISBN 978-88-902880-2-9, pp. 196–202, 2008: Describes the state-of-the-art modeling of the RFA intervention and the different effects to be modeled with a focus on the resulting measurement requirements. This material is part of Chapter 6.

- **Image-based Multi-scale Physiological Planning for Ablation Cancer Treatment**, Annex I - "Description of Work", Grant agreement no. 223877, *7th Framework Programme, VPH Initiative*: The proposal as accepted by the EU, judged with 13.5 points (out of 15) where the author of this thesis initiated and accomplished the project idea, concept, innovation, details on distribution among the disciplines of the consortium partners and the choice of partners as well as most of the writing. Marina Kolesnik contributed project management, managed the contact and communication to the partners, and organizational reading of the proposal text. Every consortium partner contributed their work package descriptions which are not used in the material presented in this thesis, as well as the state-of-the art description for their respective research domain. The material of this proposal was used in Chapter 4, the state-of-the art descriptions were partially used in Chapter 2.

- **Towards Validation for Physiological Models in Intervention Planning**, Judith K. Muehl, Rupert H. Portugaller, Philipp B. Stiegler, *Medicine Meets Virtual Reality 17*, pp. 207–209, 2009: Describes the idea of developing the animal study

and the respective imaging protocol according to the validation of a model and not relying on existing protocols. The main idea originates from and the text written by the author of this thesis. The co-authors contributed their ideas in group discussions on the final animal study protocol. This material was used in Chapter 7.

- **Computer Oriented Image Acquisition of the Liver: Toward a Better Numerical Model for Radiofrequency Ablation**, Judith K. Muehl, Bernhard K. Kainz, Horst R. Portugaller, Philipp B. Stiegler, and Christian H. Bauer *Procedings of the IEEE Engineering in Medicine and Biology Society Annual Conference., pp. 3755–3758, 2009*: Describes the imaging protocol used for the validation animal study as well as its evaluation by applying existing image processing tools. The study and the resulting imaging protocol was designed by the author of this thesis. Horst R. Portugaller provided knowledge on the exact imaging tools and protocol and implemented the imaging protocol. Bernhard Kainz operated the image processing software to evaluate the imaging protocol. Philipp Stiegler carried out the animal study. Christian Bauer implemented the used image processing software. This material can be found in Chapter 7.

- **The Future of Volume Graphics in Medical Virtual Reality**, Judith Muehl, Bernhard Kainz, Alexander Bornik, Markus Grabner, Stefan Hauswiesner and Dieter Schmalstieg, *World Congress 2009 — Medical Physics and Biomedical Engineering, 11th International Congress of the IUPESM, IFMBE Proceedings, pp. 1349–1352, 2009*: Describes the vision, idea, and concept, as well as the application cases for the multi-* raycaster. The author of this thesis defined the vision, the requirements list for the raycaster, and typical application cases. The software design and approach were then decided in group discussions, among all the co-authors of the paper. The material of this publication is part of Chapter 5.

- **Ray Casting of Multiple Volumetric Datasets with Polyhedral Boundaries on Manycore GPUs**, Bernhard Kainz, Markus Grabner, Alexander Bornik, Stefan Hauswiesner, Judith Muehl, and Dieter Schmalstieg, *ACM SIGGRAPH Asia 2009 ACM Trans. Graph., Volume 28, Issue 5, Proceedings of ACM SIGGRAPH Asia 2009, Article No. 152*: This publication describes the resulting software system first approached in the previously mentioned publication. The author of this thesis again invented the vision and defined the list of requirements as well as typical application cases. Furthermore, advised on design and development. Implementation, as well as

details on speeding up the raycaster algorithm were performed by Bernhard Kainz, Markus Grabner, Alexander Bornik, and Stefan Hauswiesner. Discussions on the overall approach as well as evaluation strategies were performed within the whole team with all the co-authors of the publication. This material can be found in Chapter 5.

- Formal declaration of innovation. Accepted for procedure to patent innovation by TU Graz. Austrian patent number A1570/2009. This patent describes the process to generate a 3D image volume from histological sections and fuse it to a CT image. The author of this thesis hereby holds the major share of 30% of the patent innovation, Matthias Seise and Bernhard Kainz hold 15% each, Sonja Koestenbauer, Ursula Mayrhauser, Philipp Stieger, and Horst Ruper Portugaller hold 10% each. The author of this thesis created the overall vision, the idea, the knowledge on computer oriented data acquisition and the resulting requirements for the laboratory work for preparing the tissue, down to details on fixing the tissue in the same position as in the CT image, slicing large sections at different distance intervals and alternate staining. The requirements for the image processing were derived from these prerequisites. Sonja Koestenbauer and Ursula Mayrhauser elaborated the details for the laboratory work, which they also performed. Philipp Stiegler and Horst Portugaller privided knowledge to the overall procedure in discussions and performed the animal study. Bernhard Kainz elaborated and performed the scanning technique for the fixed large sections, tested the non-rigid registration of single sections. Matthias Seise elaborated the image processing up to forming one stack of histological sections. Matthias Seise and Bernhard Kainz together elaborated the free-form deformation application for the fusion of the histological stack to the CT image. Bernhard Kainz performed the evaluation of the registration results. The material of this patent is reused in Chapter 8.

- **Effects of Needle Placement Inaccuracies in Hepatic Radiofrequency Tumor Ablation**, Rostislav Khlebnikov, Judith Muehl, *Procedings of the IEEE Engineering in Medicine and Biology Society Annual Conference., pp. 716–721, 2010*: For this publication the author of this thesis defined and outlined the vision, aim, approach, scientific advise, research question and concept for evaluation as well as the focus of the contribution. The solver presented as well as all application cases were implemented by Rostislav Khlebnikov. The method to start with the model presented by Kroeger in [80] was provided by the author of this thesis. Rostislav

Khlebnikov enhanced the model by the proportional integral controller and introduced the evaporation, where condensation was decided after a joint discussion by Rostislav Khlebnikov and the author of this thesis. The application to needle misplacement together with tumor perfusion rates was determined by the author of this thesis. The material of this publication can be found in Chapter 6.

The remainder of the thesis discusses how the research hypothesis was approached in this work: Chapter 3 gives an overview of the interdisciplinarity in the context of the research question. Chapter 4 introduces the concept of the Imppact project which forms the framework for this research work. As the main purpose of this thesis is the validation by simultaneously visualizing multivariate data, Chapter 5 explains the visualization task as well as the implementation of our created tool: the multi-* raycaster. Chapter 6 explains the background on RFA as well as our finite element solver. The elaborated simulation shows deficiencies in created coagulation by non-optimal needle placement. Chapter 7 explains the establishment of a reference model from a computer oriented data acquisition procedure. Chapter 8 shows the procedure to reconstruct a 3D volume from histological sections. All these parts together form an innovative and unique procedure to validate a prediction of a complete RFA intervention by comparison to experimental results in an animal study. Also the required and newly designed tool set is defined and introduced.

Chapter 2

Related Work

Contents

Our work deals with creating a validation system to test a biomedical model intended for treatment planning of RFA in the liver. This challenge is new and has not been approached previously. We first take a look at the medical procedure and the research performed on it in detail. Second, we examine the state of the art in treatment planning systems and their modeling components. Third, we look into suitability of existing solutions needed for completing the task of setting up a validation system and identify deficiencies.

2.1 Radiofrequency ablation — an overview

RFA is a rather new procedure in clinical practice. Patients were treated first in 1993 [99]. Modeling of heat transfer to predict the procedure outcome was already a research topic in 1994 [10]. An overview of the topic and different aspects can be found in [2]. A description of the medical procedure in clinical practice can be found in [2], [61], and [86]. Reporting criteria and terminology for this intervention are discussed in [63].

In the medical domain, there exist a lot of publications which deal with the overall approach or statistical questions surrounding RFA, especially in clinical practice. The questions surrounding events of local recurrence are still a most important research topic and often examined — e.g. in a meta-study [106]. These examinations also concern statistical evaluations from clinical treatment practice over time [72].

From an engineering perspective Organ [114] gave an overview of electrophysiological principles of RFA as early as 1976. A more recent insight was provided by Haemmerich et al. [67] in 2004. Many biomedical researchers describe the process of RF ablation in an abstract way and compute heat distribution for artificially generated situations. For example, the authors of [159] investigated the influence of the blood flow rate on tissue temperature and lesion size in an artificial vessel.

The most prominent effect in RFA procedures is the heat sink effect through perfusion — especially that due to large vessels. This effect was researched by Patterson et. al. in 1998 [120]. The study looked into effects in an in-vivo study in porcine liver. An analytical relationship between the heat convection coefficient, blood velocity and temperature was formulated by Consiglieri et al. [44]. Santos et. al. looked into the temperature distribution on the vessel walls [49].

2.2 RFA treatment planning systems

Models simulating the complete process are created to be used in treatment planning applications. The first prediction of the RFA treatment result [154] modeled the shape of the necrosis zone as an ellipse (as out forward by Butz et al. [36]) with cut outs for blood vessels [155]. The respective treatment planning tool RF-Sim [154] provided an extensive planning environment showing a virtual presentation of the liver and the surrounding anatomical structures, was able to compute the optimum position for needle placement [152] and gave haptic feedback in intervention simulation [153]. The above research results were obtained in the framework of the nationally funded research project START. This approach, to model the necrosis zone as ellipse, is too simplified to meet reality. (`http://www.ircad.fr/virtual_reality/start.php`).

Modeling the necrosis zone as an ellipsoid was reused in the RFAST project (`http://rfast.cit.nih.gov`) by the National Institute of Health, USA. This project led to a planning tool for RFA that incorporates image processing tools [98], but — as it was still based on the coarse shape estimation for the necrosis zone — still has the same limitations as the RF-Sim approach.

Physiological models computing RFA are based on the bioheat equation [123]. A physically based 3D model to simulate RFA was created as part of the nationally funded research project FUSION (http://www.somit-fusion.de/SF/). Results based on anatomical structures were developed by Kroeger et al. [80]. The model has been used for workflow oriented treatment planning [157]. Another model was created at NTU (http://homepage.ntu.edu.tw/ twhsheu/research/research$_b$s.htm), [139]. In 2008 Schutt et al. [135] presented a comprehensive model for the RFA process, though it has not been applied to treatment planning scenarios. It uses the creation of a proportional integral controller as researched in [69].

Kroeger and Schutt both modeled biochemical reaction rates like Stein [142] based on the reaction time for sugar and acids [11]. Kroeger's model has been used for planning the optimum needle position [5]. These needle placement computations have also been computed for other models (for example in [42] and [152]). However, these needle placement computations are not suitable for use in clinical practice as many factors outside the liver, such as positions of bones and lungs, also influence the best needle path. Even if the best needle position is computed it is difficult to place the needle exactly as computed.

None of these complete models has been validated experimentally. Our approach on creating an intervention planning system is presented in Chapter 4. Since the key instrument of the planning system is a physiological model with enough predictive power we first look into existing models and single aspects known about the procedure.

2.3 Modeling aspects of the complete process

The input for a model computation is taken on a macroscopic scale. Some effects that influence the outcome of the intervention already apply on this scale. We look at the state of the art on this macroscopic level to identify the building blocks any model predicting RFA has to provide.

2.3.1 Macroscopic factors

The effects of perfusion by vessels with diameter > 3 mm (heat sink) and tissue inhomogeneity on RFA treatment results have been observed many times in medical experiments (e.g., [58], [93]) as well as in patient treatment. Mathematically advanced predictions on the influence of perfusion were carried out in [135], [139], and [150]. This approach is useful when looking at abstract questions or very detailed effects. A treatment planning

system, however, demands a different approach. Tungjitkusolmun et al. [150] showed in great detail the cooling effect and the effect of moving the hotspot in the direction to the vessel.

The influence of the needle geometry has been widely researched. A comparison of different needle geometries can be found in [90]. The process of RFA is controlled by an ablation protocol. Ablation protocols have not been widely researched. Looking at efficiency and deposited energy [34] gives some insight. The electrode extension algorithm for the RITA system has been researched in medical experiments [21] but is not part of any planning application as yet.

The RITA manufacturer set the protocol for expanding the needle array according to a given time set depending on the tumor size [6] It was predicted that the created lesions have a spherical shape [8]. Nevertheless, in an egg white study Lobik et. al. showed that the shape of coagulation zone is not as predicted by the manufacturer [90]. The RITA system was simulated by Schutt et. al. [135]. It included many features necessary for the RITA needle. Our modeling approach for the RITA system is based on Kroeger's approach and is described in detail in Chapter 6.

Coagulation is most often modeled using the Arrhenius formalism [11]. The reaction rate here is based on the reaction time for sugars and acids. The Arrhenius formalism uses an equation based on an exponential function (approximation to a state of saturation) with experimentally found constants. Physically measuring their values demands the examination of tissue samples in a laboratory. Haemmerich et al. found the isosurface for 50°C to fit the predicted coagulation when using the Arrhenius model for predicting coagulation. Measurement techniques for the used constants are described in detail for example in Stein [142]. While Stein concluded, that the differences in material properties are negligible, Cosman and Cosman [46] showed the differences in material properties for heating tissue concerning electrical properties to be significant. Dielectric properties are often researched, so for example in [115] and [128]. Thermal constants are harder to measure and therefore not as often studied. Bhattacharya et al. [22] examined changes concerning heat conductivities. Changes in parameters are not neglectible here either. Tissue properties are also known to change with temperature, for example leading to denaturing [14]. Brace et al. [26] found permittivity and conductivity to decrease by about 50% when approaching temperatures of 100°C. Duck [51] presented a large collection of measured values. Haemmerich et al. examined the specific heat capacity of liver tissue [68]. They furthermore showed the effects of tumors as inhomogeneity factor depending

on the frequency used in heating up the tissue [70]. A model for computing evaporation of cell fluid has been created by Yang et al. [165] as well as by Schutt and Haemmerich [135].

2.3.2 Microscopic aspects

The effects of RFA cannot be determined solely on a macroscopic scale. In fact microscopic aspects also determine the intervention result on the macroscopic scale — for example microperfusion.

Effects of microperfusion have been studied by Jain et. al. [76]. Recent work has enabled suitable models to be produced [41]. There is a strong regional dependence on the vascular properties, which will be included in a suitable model. Neill et al. [113] modeled the liver tissue as a porous sponge to account for microperfusion and applied this model to estimating tissue temperature [122].

The residual post-treatment thermal inertia means that the process continues after the RF generator is turned off. Findings in medical studies show changes in the form of the necrosis zone after the treatment. Therefore, early detection of local recurrence is performed by analyzing 3D shapes in follow-up scans [32], [33], and [57].

Though these follow up scans are usual in treatment practice they only show the appearance of the tissue in an imaging modality. To see the real result of the intervention tissue samples have to be examined. So Morrimoto et al. [105] evaluated morphology and histological characteristics of RFA lesions over a six months follow up period and compared the results to those of radiological studies.

Models for ongoing cell death after ending a thermal ablation have been proposed by Breen et al. [29], and Chen et. al. [43]. These models start with measuring the thermal history for the regions and therefore rely on the observation of heat dissipation in tissue on the radiological scale. Unfortunately, the RF generator works in the same frequency range as the MRI necessary to perform the scans. Possibilities to overcome this issue range from changing the ablation protocol [171] to modifying the ablation device [116]. Another approach concerns the development of new contrast agents [56]. A good review on this topic can be found in [55]. These thermometry measurements are not feasible in high resolution due to technical difficulties. Furthermore, they only give information on the process during the ablation.

By relating the thermal dose taken in by a cell during the ablation, the cell death models by Breen et. al [29]. and Chen et al. [43] predict cell death according to phe-

nomenological descriptions. These phenomena have so far not been integrated into any planning application. Still, the prediction of the treatment result directly after ablation or even a few days later is an important research topic. The correspondence of radiological images with tissue response was researched by Goldberg et. al. [62] in 2000. Lu et al. look into the heat sink in post-ablation CT scans as well as in histological examinations and compare the results [93]. Raman et al. compare CT as well as Ultrasound imaging to findings in histology and conclude CT imaging is rather similar to histological findings while Ultrasound imaging tends to underestimate the size of the created lesion [129].

Many details determine the outcome of the complete procedure. Many details are known but there is still no complete validated equation that models the process at least on a less complex level. So the research hypothesis in this thesis has not yet been addressed and demands an approach from many different directions, but many useful details are known. So the challenge is solvable.

2.4 Processing of radiologically acquired image data

All patient-specific intervention planning relies on radiological data. The same applies, of course to the model computations. To be able to compute with a radiological image is input it needs to be processed by a computer. We look at the state of the art in image processing to decide if progress in this direction is necessary to reach the overall goal.

2.4.1 Segmentation

Even though manual segmentation is time consuming, it is most often used in clinical applications. Several automatic methods have been, however, proposed for liver segmentation. Most promising methods are based on deformable models [140], but even the best automated techniques have problems with atypical livers. Semi-automatic methods [164] are a good balance between manual and automatic methods when both computation time and segmentation accuracy are considered to be equally important.

Extensive evaluation of semi-automatic segmentation for internal structures in the liver showed that region-growing and iso-contour algorithms [94] could potentially be used in clinical tumor segmentation as a trade-off between fully automatic and entirely manual segmentation. Also for vessel segmentation, region-growing techniques [138], [169] have given good results. In both applications fully automatic methods [59], [140], have also been proposed. Although some of the results have been very promising, reliable automatic

segmentation remains an unresolved issue.

For the work in this thesis, two liver and vessel segmentation approaches were chosen. First images were processed with the semi-automatic method of Unger et al. [151] for segmentation of the liver itself. At this stage an approach for segmentation and separation of the livers vascular trees that is based on the work of Pock et al. [125] and described in detail in Bauer et. al. [17] was chosen. During evaluation of this method on clinical CT datasets of humans and on phantom datasets the use of different imaging protocols showed a strong influence on the number of identifiable vessels and the achievable surface accuracy [71]. Later in this thesis the image processing tool by Alhonnoro et al. [4] was applied as it demands less user interaction.

Independent of the image processing used, an applied segmentation algorithm can only find structures in the images that are imaged. Chapter 7 discusses the data acquisition from CT images suitable for our validation task.

2.4.2 Registration

One single image never gives complete information on a process with all its parts. So many images have to be acquired and have to be registered to provide all information necessary for the validation experiment in one single coordinate system.

The reconstruction of one patient specific anatomical model from multiple sets of pre- and post-interventional datasets demands both rigid and non-rigid transformations to capture complex motion/deformation of the liver. State-of-the-art methods use non-rigid transformations with large numbers of degrees of freedom (DOF) and voxel-based similarity measures [83], [133]. They are therefore computationally very expensive.

Liver parenchyma is soft tissue and deforms with every breath. Registering different radiological images showing the liver will therefore require non-rigid registration. State of the art techniques to perform non-rigid registration can be found in [35] and [172]. For registration of multiphase CT images a state-of-the-art report on intra-modal registration was published in [83]. In [75] a new and faster method to solve this registration task is evaluated. For registering radiological pre- and post-operative images we rely on state of the art tools. Again the right image acquisition for suitable images is discussed in Chapter 7.

2.5 Examining treatment results histologically

Treatment planning always has to rely on radiological images. However, the final result of the intervention is only reliably visible in histological examinations. So a fusion between both modalities — in fact one 3D image dataset showing both, radiological and histological outcomes — would be highly desireable. To gain this information, we have to prepare a whole volume of tissue which is cut and examined section by section. The prepared sections then have to be stacked to form a 3D volume. Fusing the reconstructed histological volume with the corresponding radiological one then demands non-rigid registration to counter the numberous deformations in the process. This process equals the modeling fusion of microscopic and macroscopic effects for the experimental and data acquisition side.

2.5.1 Tissue preparation

To examine the area of interest histologically, the tissue has to be harvested and prepared to obtain stained slices. Large section histology is able to show the whole area of interest in one single section. This method is used for histopathology of cancers favored in the field of gynecology and obstetrics [82], [144]. It is based on fixation and dehydration (alcohol serial, xylol and acetone incubation) of the tissue and embedding into paraffin. For each sample the method is adapted. In situ perfusion of the livers in combination with immersion fixation is described in different standard protocols [1], [78].

Lu et al. [93] as well as Patterson et al. [120] explanted an RFA treated pig liver and trimmed it to the area of interest. Representative gross sections of lesions were examined. Tissue preparation used perfusion fixation and embedding in paraffin wax. Wright et al. [162] used a similar procedure to gain sections in mm intervals which are used for pathologic evaluation. A study [110] on the impact of laser-induced coagulation necrosis described a different fixation and staining method to evaluate the effect on the cellular level. Yoshimoto et. al. [166] used this technique to visualize the necrosis area of in vivo RFA in pig liver.

A preparation of liver tissue optimized for large sections suitable for later image processing and final fusion to 3D radiological data has not been achieved so far. We meet this challenge with our approach as explained in detail in Chapter 8.

2.5.2 Involved image processing

The sections produced in the laboratory need to be scanned and then processed by computer vision. Segmentation and registration for histological sections both rely on the other algorithm's results. The segmented vessel candidates build the natural feature points for the registration algorithm. At the same time, the probability of identifying a vessel candidate is higher if a neighboring section has candidates in the respective area too. So the challenge concerns a joint registration and segmentation solution.

Formulating the joint segmentation and registration problem in a variational framework was done by Ehrhardt et al. [52]. Solving that formulation is computationally too demanding for the large data sets delivered from a stack of histological images. The other approach is to divide the task into two independent sub-tasks: segmentation of tissue structures from 2D histology sections and registration of the 2D sections for reconstruction of the 3D model. In Dercksen et al. [48] that approach has been successfully applied to histology images of a grain. Braumann et al. [27] build a volumetric probabilistic model for the tumor tissue which was segmented using a 3D level-set.

For classification of tissue types an unsupervised standard mixture of Gaussians (GMM) classifier which is widely applied in color image segmentation tasks [163]. Other, mostly supervised, classifiers have been applied to histology tissue classification (e.g. hierarchal AdaBoost & Decision tree [50], neural networks [48]).

Aligning stacks of histological images to reconstruct a histology volume has been performed in [12] and [103]. [145] describes an approach less sensitive to noise using curve fitting.

2.5.3 Fusion of histological and radiological data

To cope with the final fusion the stacked histological sections have to be non-rigidly deformed. Free-form deformation is an important tool in computer-assisted geometric design and animation. Barr [16] developed a method which altered the transformation while it was being applied to the object. A more general technique was later developed by Sederberg and Parry [136] which deformed objects by deforming the space in which the object is embedded. Another method was developed by Coquillart [45] which used an initial lattice and B-spline control points to approximate the shape of the intended deformation.

Fusion of histological and radiological data is often attempted for small, easily stiffened or non-deforming tissue samples to avoid registration errors. Ou et al. [117] registered histology to MRI data for the prostate gland. As features of interest which provides

the control points both landmarks and the region with cancerous cells were chosen. The landmarks were chosen on the prostate boundary, the cancerous region itself was chosen for aligning this region of interest with the MRI image. Another approach was chosen by Zahn et al.[170]. In their case the 2D histological images were warped to fit some plane in the MRI data. No 3D warping of a reconstructed block was attempted or achieved. Yushkevich et al. [167] used histological sections of a mouse brain for fusing with a respective MRI scan. The fusion approach deals with a stack of images oriented on another stack of images. The method therefore depends on orientation of the image planes to be similar.

Ourselin et al. [118] worked on fusion for histology and MR data for the Human Basal Ganglia. This part of the brain does not deform in radiological images and — being the brain — is easily stiffened for histological examinations. So their block of histological slices did not need to be distorted in 3D after its reconstruction and the registration step from the 3D histology block to the MRI data was achieved using an affine registration. Meyer et al. [101] worked on a glioma brain tumor in a rat. Again this is a very small volume, and easily stiffened. Deformations of the histology block were therefore minimal and not significantly processed. Another approach was to fuse histological slices with micro-CT data, which shows the prepared block just before sectioning [130]. Using Micro-CT data as intermediate step in a registration procedure to go from histological data to CT data for lung cancer was published by De Ryk [47]. This method relies on taking micro-CT data as an intermediate representation to ease the registration task.

Observing the three-dimensional result of RFA was approached in [58]. The slices used had a thickness of a few mm $(4-6)$ and a rigid registration. Therefore the result was not a histological examination. Moreover, the sliced tissue could only be roughly compared to an MRI or CT scan as there was never the same slice visible in the scan as in the tissue and there was no compensation for slicing either another parallel plane or else a non-parallel plane.

For radiofrequency ablation, Work on registration of radiological images and histological results was conducted by Breen et. al. [31] using a specifically developed coarse histology slicing method (slice thickness 3 mm). They also developed a procedure to register their stacked photos of macroscopic tissue to corresponding MR images using fiducial markers and anatomical landmarks [30]. Again, as no volume was under examination. The fusion of histologies to MRI scans was based on slices. Though spatial distortion was addressed, it was not sufficiently solved for heavily deforming organs.

2.6 Computer graphics and scientific visualization

For our validation, we aimed at comparing a model's prediction to the result of a real intervention in 3D. So we needed a computer graphics system able to visualize all data and give hints on where a model fits reality and where inconsistencies are hidden. We took a look at existing visualization systems and discussed their suitability for this task.

The visualization of multi-dimensional and multi-modal datasets as generated by computational simulations is a research topic in its own right [85], [107]. Unlike aiming at the highest possible degree of automation, interactive visualization and visual analytics [147] aim to provide optimized tools for the work of a human expert [156]. There are two approaches towards three-dimensional rendering of medical data: surface-based rendering requires the segmentation and reconstruction of surfaces of anatomical structures, whereas direct volume rendering operates directly on the volumetric data from medical imaging. Recent advances in graphics hardware have made interactive direct volume rendering (DVR) possible. DVR offers higher quality images and a larger degree of freedom, since no data is lost during a transformation [87]. Nowadays GPUs allow visualizing volumes with this technique at interactive frame rates on consumer hardware. We now look into the details of volume rendering systems and describe the approaches known so far for real-time volume rendering systems.

2.6.1 Multi-volume rendering

Rendering of multiple volumes is a recurring topic of research. While multi-volume rendering was previously limited to static images (for example [108]), CPU based rendering has relatively recently achieved real-time frame rates through the use of cache-coherent, multi-threaded strategies [66]. However, the processing power of CPUs has been overtaken by GPUs, which have more parallel processing units. Volume rendering is now commonly based on representing regular volumetric models as 3D textures in the GPU memory, and casting rays in the fragment shader. The setup of rays is done through rasterization of the volume's bounding geometry [81]. With the advent of branching and looping in the shader, a ray can now be traversed inside the shader rather than through multi-pass rendering [141].

Through the use of depth peeling [53], handling of more complex scenarios becomes possible. With respect to GPU-based volume rendering, depth peeling has been used to clip volumes [158] and to intersect individual volumes with geometry [24], [146]. Recently multi-volume rendering has been combined with depth peeling and dynamic shader

generation into a very efficient framework [132]. Depth peeling is used on the bounding geometries of multiple volumes allows the performance of what are essentially CSG operations, and every distinct volumetric area is handled with optimized shader code that is derived from an abstract representation. A similar approach combining depth peeling and dynamic shader generation was taken in [124]. The work in [28] is unique in that it is able to combine multiple volumes with arbitrary layers of translucent, concave geometry.

2.6.2 Fragment processing

Depth peeling is a widely used multi-pass technique that relies on manipulation of the z-buffer to progressively reveal layers of occluded geometry. Generally speaking, multi-pass techniques are methods used to overcome the limitations on the resources of the GPU, in particular in terms of available storage. Given unlimited memory, an approach like the A-buffer [39] can store all fragments in a list sorted by depth. Such an implementation is not really feasible in hardware, and therefore various approaches operating with bounded memory rely on multiple passes. Achieving effects involving multiple fragments often requires sorting of fragments by depth. Hardware-accelerated depth peeling [53] is such a method, but requires N rendering passes of N objects, leading to undesirable $O(N^2)$ complexity. Several pieces of work try to at least reduce this complexity by a constant factor, by making use of additional memory. This can take the shape of specific extensions of the fragment stream processing model of the GPU [3], [96], or by relying on existing extended framebuffer capabilities [18], [19], [37], [89]. Some work combines such an approach with an approximate pre-sorting on the CPU, in order to approach linear time behavior [160], [37], [40]. However, such a pre-sorting is not feasible for general scenes.

A common acceleration technique for polygon rasterization is coverage masks [54]. These encode the pixel-wise inside condition with respect to a half plane in any possible orientation (typically for 8×8 pixel squares). Arbitrary convex polygons (and triangles in particular) can be processed by computing the intersection of the half planes associated with the edges, which is equivalent to a bit-wise *and* operation of the corresponding coverage masks. In the literature, there are examples both for precomputed masks [54],[65], and for on-the-fly computation [137].

2.6.3 Rendering on manycore GPUs

Recent trends indicate that graphics programming is rapidly moving away from fixed-function approaches towards general compute languages executing on manycore archi-

tectures [73]. Rather than redesigning existing techniques to fit the highly constrained execution environment found in conventional GPU programming using shader languages, software rendering methods can become competitive again by executing them on manycore GPUs.

A noteworthy example is the Larrabee manycore architecture [137], which is based on multiple x86 cores and uses a flexible software renderer including a recursive polygon tiling algorithm [65]. This approach is highly optimized towards Larrabee's hardware capabilities, in particular its vector processing units. Developing on GPUs with CUDA is not quite as flexible as Larabee's execution environment but allows similar results to be achieved using mainstream graphics hardware. For convenience, we review the main aspects that influence our work. CUDA executes kernels written in C in a massively multi-threaded fashion on the GPU's multiple processing cores. Threads are grouped into blocks, which are executed with round-robin scheduling on a multi-processor consisting of several single processors and a limited amount (16 kB) of fast shared memory, which acts as a cache. Threads also have access to the GPU's global memory at a slower speed. Fully utilizing all processors while avoiding memory latencies requires careful design of algorithm and parameters.

A brief report on ray casting single volumes with CUDA was given in [97], concentrating on the best choice of execution parameters for basic ray casting. Single volume ray casting with moving least squares was considered in [84]. This method achieves very high quality reconstruction, but seems more appropriate for unstructured volumes. Ray casting of large deformable models composed of opaque polygons was presented in [119]. This work sorts all polygons into a view dependent 3D grid at every frame, and therefore focuses mainly on the sorting.

For our validation task we needed to deal with multiple overlapping volumes and polygones. We needed a flexible solution at interactive framerates for the visualization of CSG (constructive solid geometry) operations in real-time. A system like that is beyond the state of the art. Our approach and implementation is described in detail in Chapter 5.

2.7 Summary and discussion

Complete models for treatment planning have been developed and used for predicting the treatment outcome. Unfortunately, they have never been validated by experiment. Two main challenges arise: first, we need a concept for validation as acceptable to a natural

science researcher (a medical expert) as well as to an engineering science researcher who is building the model. This question leads to understanding the gaps between cooperation of the different researchers and developing a concept for validation. We elaborate a solution for this challenge in Chapter 3. Chapter 4 furthermore explains the created cooperation environment in which the concluding necessary research was undertaken. Chapter 5 finally closes the gap for a validation strategy. As we are searching for visual validation to satisfy the requirements of interdisciplinary work, this chapter also presents our main validation instrument: the flexible real-time multi-volume rendering system identified as gap in section 2.6.

We furthermore see deficiencies in creating a model suitable for validation and adress this issue in Chapter 6. We need to compare our model's computational results to the real results of the intervention. So we need to acquire respective data, which then has to be processed. As the image processing tools seem adequate to solve the problem provided the right data has been acquired, Chapter 7 describes the data acquisition for the real data in an animal study. The intervention result is only visible in histological examinations. Chapter 8 therefore presents our approach to examining 3D data blocks of histological data.

Chapter 3

Interdisciplinarity

Contents

Nowadays many research questions cannot be answered by one discipline alone, but demand an interdisciplinary approach. Research progress has to be made in more than one discipline and especially across the borders of the respective disciplines. The research question of simulating the RFA process, especially with a validated model, belongs to this category of research questions.

3.1 Basics and definitions

When is research interdisciplinary? — A quick answer would be: when more than one discipline is participating in the research performed. To understand and examine this answer it is important to see what a discipline is in the context of research and how different disciplines are related to each other.

A definition for "research discipline" or "academic discipline" has been subject to philosophy from the times of Aristotle (384-322 BC) up until the current time [92]. To

avoid diving deeply into philosophy we will start from our general understanding of the subject and establish the definition:

> *Definition:* a research discipline or academic discipline is a branch of learning studied at a university. [143]

Disciplines can be roughly grouped into *branches of knowledge*. Also within one discipline different areas can be identified and grouped. For example physics consists of thermodynamics, mechanics, optics and many other fields. In computer science, computer graphics is included and also the database systems. We call these areas within a discipline *subdisciplines*.

The research question addressed in interdisciplinary research cannot be solved by applying independently achieved research results — so not by combining results without integration — but by integrating the research on the way to create solutions. The theory of science therefore demands for interdisciplinarity to not only cross topics but also join scientific methods together to solve the interdisciplinary research question [77], [104]. We derive the following definition:

> *Definition:* interdisciplinary research is the connection of more than one research disciplines including their specific research methodology in an interwoven approach.

Nowadays Interdisciplinary Studies is a study subject in its own right. The topic is rarely addressed in engineering or natural sciences as it generates understanding and meta knowledge, but does not enhance the academic knowledge in one of these disciplines directly. The subject is rather aligned with social sciences and communication studies. Communication is often identified as the key difficulty in interdisciplinary research.

In engineering sciences, very few articles have been published on difficulties in handling interdisciplinary work. Those articles that show up from searching typical engineering publications present communication as the key issue to be addressed in this type of work. Carlis [38] found ten typical pitfalls which have to be addressed in interdisciplinary research. The article gave a nice overview over crossing an engineering science with a natural science. He gave four good pieces of advice to handle this type of problem: embrace the struggle to communicate, hang out together, plan for unplanned changes, modify researchers' education.

Gooch [64] addressed communication strategies for interdisciplinary teams in writing a grant proposal together. The article looked into management and strategies for collaboration and sees its role as a case study. The team had members from several disciplines,

engineering as well as natural sciences and mathematics. The article did not look into the different natures of participating disciplines and therefore not into the reason for misunderstandings but rather discussed communication strategies.

Mehandjiev et. al. [100] presented results from a workshop on interdisciplinary software engineering. The workshop participants here described elaborated methods, techniques and concepts from different disciplines, which all address contemporary software engineering. The article therefore focused on presenting different approaches rather than attacking the problem of interdisciplinarity or communication.

Far more contributions exist on cooperative writing, which might also be an aspect for interdisciplinary communication if one looks into the nature of communication. We will look into the research question of radiofrequency ablation simulation as a case study for interdisciplinary research.

In the following sections we first identify the disciplines and subdisciplines participating in this specific research question. Then, for every participant an expert is interviewed to characterize the methodology applied. By evaluating these interviews we find similarities and differences between the collaborating (sub-)disciplines. Communication is successful if it is based on a common context. Where the common context is missing it has to be established. With communication being a key difficulty, similarities build a strong bridge between the collaborators. We conclude this section by adressing the differences found in the expert interviews and presenting strategies to overcome the difficulties found.

3.2 Radiofrequency ablation — participating disciplines and subdisciplines

Creating an interdisciplinary research approach for our application case demands that we first take a look at the participating specialists and in which branches of knowledge they originate. Our research question dealt with creating a planning application for a medical intervention. The intervention was performed by a radiologist. So a medical doctor specialized in radiology was the first expert whom we needed to involve in solving the question. The intervention was planned based on radiological images. As we needed to apply additional information about the physiology of the patient in addition to the radiological images we needed to process the images and create a form that enables computation on them. So the next expert involved was a computer scientist who specializes in image processing and computer vision in the medical domain. The output of this processing step was

an anatomical model of the liver suitable for applying computations to it. The equations that model the physiology of the patient relevant for the intervention are researched in the area of biomedical engineering. So a biomedical expert specializing in tissue ablation and heating is the next expert had to be involved in this research. To be able to apply the equations to the real geometry of a patient image, a mathematician specializing in numerics needed to work on solving the equation in a non-analytical way for the arbitrary geometry. The result is data which needs to be presented to the performing radiologist in a way that satisfies his expectations and is easily comprehensible. So finally this needed a computer scientist specializing in computer graphics and more precisely visualization.

Though the data processing chain sketched above is complete for building an application which supports the planning process there is an additional requirement. The planning application is supposed to deliver the correct prediction and needs to prove that it does. Otherwise it would not be of any use in practice. However, the result of the intervention concerns cell death of a certain region of tissue. This is only visible in histological examinations. So we needed at least one more expert examining the tissue to take a look at the result and one more expert processing this kind of data to integrate it into the computer model. Tissue inspection is done by pathologists, while methods for preparing the tissue are subject to research in microbiology. As the result of the tissue preparation has to be integrated into the computing model, rather than being observed under the microscope, involving an expert in tissue preparation is mandatory. Processing the images created from tissues once again is computer science and image processing. It is a different aspect rather than processing radiological data, but does not involve a new discipline. So, finally, our application case extended through three different branches of knowledge: natural sciences, formal sciences, and engineering sciences.

3.3 Methodologies in the participating disciplines

The research topic as well as the methodolgy differ widely for the disciplines participating in research on radiofrequency ablation. Especially, as the participating disciplines belong to three different branches of knowledge and can roughly be grouped as formal sciences (numerics), natural sciences (molecular biosciences and radiology) and engineering sciences (biomedical engineering, computer graphics, and computer vision). The following interview summaries explain the respective research approaches for the disciplines and subdisciplines participating in our example case.

3.3.1 Research in numerical mathematics — finite elements

In the case of our application scenario, contributions in mathematics concern numerics. The aim of this research subdiscipline is to find methods to process numbers in computations that cannot be solved directly (analytically) and therefore have to result in approximations. As in all mathematics in the center of basic research stands deduction and proof of new theorems to extend so far existing methods and theorems. The methodology applied is the formal proof of correctness for new findings. Research contributions either go in the direction of finding a very good special solution to some complex applied problem or else in finding a new technique to a general (not complex) solution. First questions concern the creation of a mathematical model for the application case, the existence of a solution, and validation of the model's correctness. Here also, inverse engineering can be applied. Other questions concern the stability of the solution as well as its behavior in the case of perturbation. A contribution is for example a new method to solve some equation numerically, new findings in predicting errors, or in simplification. To evaluate a result means to judge the correctness of a proof and inflicted errors. Significance for a result is high if the elaborated method is applicable to a large class of problems or excels in the researched quality criteria above the state of the art, for example, if a solution converges earlier than comparable methods. Of course a mathematical proof of correctness belongs to a contribution. However, the proof often concerns very special cases and proving the general approach, for example that some method always works for a specific class of problems, is established years after the first application cases. (Dr. Zaglmayer — private conversation [168])

3.3.2 Research in computer science — computer graphics

Computer graphics aims at creating images and visualizations. Often this includes systems with graphical user interfaces and therefore also user interface aspects. Computer graphics is an engineering subdiscipline and therefore looks into the creation of new solutions — innovation. Often a research result can easily be seen in an implementation demonstration. The approach to generate results is often bottom-up, meaning first a simple solution is created, then single aspects are enhanced and a bigger solution is created out of a preliminary small one. Contributions consist of new techniques, algorithms or systems. A weak evaluation of a result can be achieved by a demonstration (show that some feature actually works). Stronger evaluations use quantitative measurement of some criteria (like runtime) or for example in user studies if perceptional effects are targeted. The significance

of contributions is high if the innovation is large, the applicability is wide or result in very obvious visual differences. Therefore, for all practical aspects the bigger an innovative step the better. Good results mean a theoretical approach and explanations, together with an implementation. One alone (only theory or only implementation) is not enough. The subdiscipline includes interdisciplinary aspects through the integrative systems approach. (Prof. Dr. Schmalstieg — private conversation [134])

3.3.3 Research in computer science — medical computer vision

Computer vision is concerned with three main questions: understanding the process of seeing, building machines that see, and principles of seeing. Research in medical computer vision thereby is grouped in the second question with processing and understanding medical images. So it is actually the inverse problem of computer graphics and from this point of view both are closely related. In the center of computer vision stands recovery of information that is given ill-posed and can only be achieved when using reasonable assumptions. So it comes clear with a more analytical approach. Medical image processing creates specific algorithms to solve very specific tasks optimally — for example one algorithm is designed only for segmenting the liver surface, another one for the heart, etc. Other areas of computer vision deal with algorithms that solve a larger class of problems. This research is then also influenced from artificial intelligence research and machine learning. For all of computer vision a contribution would consist of a new algorithm or a new technique, which is evaluated for capabilities, but also for correctness (for example true or false recognition of positive or negative candidates) or else for higher speed. The methodology is therefore a mixture of engineering and formal sciences such as mathematics. A contribution is significant if it enables a new technique, or makes a large step forward in quantitative indicators for successful information recovery. A correct evaluation of the respective achievement is of course vital. (Prof. Dr. Bischof — private conversation [23])

3.3.4 Research in biomedical engineering

Research in biomedical engineering in our application case aims at modeling biomedical processes in the human body. It always starts with a clinical question to answer, which determines the approach taken and the tools to be developed. Biomedical engineering is — as the name says — an engineering science and therefore very pragmatic. So at the center of this research stands the invention of new models and therefore understanding of processes and data. The approach is iterative in nature. So when a model is built its

prediction is compared to respective data and if deficiencies arise the model is improved for the particular purpose under examination. The methodology applied here can work in both directions, bottom-up (to form a mathematical model and see if it fits the biomedical reality) or top-down (to look at biomedical data and derive a model from that data), but a new model has to be superior to an old one in at least some specific case. Evaluation of a model can be achieved as proof of concept but is better judged in measurable quantities. The creation of a model demands that it is computationally solved so the result can be demonstrated. Significant results are achieved by validating one part of a model and then extending this model with another part so it fits new data. Wide innovative steps or else important questions that are widely applicable lead to highly significant results. So larger steps of innovation are preferred but thinking without applying is only half the way to go and not worth much. With the hint of understanding processes and creating models with predictive power biomedical engineering holds aspects of analytical thinking as natural sciences or else computer vision do. In fact there is a large crossover of biomedical engineering and medical computer vision. People from both disciplines work on identical research questions together. (Dr. Payne — private conversation [121])

3.3.5 Research in molecular biosciences as basic research for medicine

Biology is a natural science. So its aim is to understand and explain parts of reality — in the case of biology: life. Biology is structured into a lot of sub-categories. One of them is the relatively new category of Molecular Biology. It focuses on questions on a molecular scale (e.g. RNA, DNA level). In all categories of biology, experiments under controlled conditions stand at the center. Observations are made, evaluated and experimental results are brought into context with other findings. The research methodology is hypothesis driven, that means the question and the approach to examine the question are important factors. According to the hypothesis the technology and methods are chosen. It is normal to start with established methods, a valid technique, independently developed and already evaluated/published, which were adapted to the experiments to follow the hypothesis. However, often there is the need to set up totally new experimental techniques to provide the required information. Biology is a very inventive and substantial sciences. Every answer brings up new questions. Qualitatively good science need to provide an answer to an addressed question in a clear, traceable and reproducible way. The most important part is the interpretation done by the experimenter. He is responsible for bringing the results into the right context and giving the answer to the question addressed. The quality of the

work is not in direct correlation to the importance of the work for the science community. Every aspect of science is important for the whole picture of life but not every topic is important for the human being. In the context of our application example methods and techniques of biology are used as basic research for medical questions (Dr. Koestenbauer — private conversation [79])

3.3.6 Research in medicine — radiology

Medical research aims at understanding the human body to be able to cure people. It is an applied research approach which puts clinical studies and clinical treatment practice at the center of interest. A hypothesis driven approach is highly demanded. First, the design of a study is cumbersome if it does not follow a clear hypothesis and also the ethical justification suffers if studies are just fishing for some unknown data correlation. Hypothesis driven means the question and its validation have to be known before the study is conducted and hereby equals the top-down approach in engineering sciences. Evaluation of the results of a study is performed using statistical evaluations to meet the lack of control over the complex system that a patient always constitutes. The importance of a result is high if a study approaches a very new research question and statistical results are mathematically significant. Studies on patients are very limited due to ethical reasons and have to be very limited in deviation to the normal treatment procedure. Clear ethical rules apply and are ensured by ethics committees. (Prof. Dr. Portugaller — private conversation [127])

3.4 Comparison of the participating research disciplines

The above sketches for the research disciplines show the shape of research practice for the participating (sub-)disciplines. Table 3.1 gives a summary of the descriptions to gain a clear picture of differences between the participating subdisciplines.

	Finite Elements	Computer Graphics	Medical Computer Vision	Biomedical Engineering	Molecular Biosciences	Radiology
Topic/Context	Process numbers in computations that cannot be solved analytically	Creating images and visualizations, including user interfaces	Processing and understanding medical images, recovery of ill-posed information	Modeling biomedical processes	Understanding life, focuses on molecular scale (RNA, DNA)	Understanding the human body to cure people
Applied Method	Formal proof of correctness for new findings	Engineering methodology, bottom-up approach	Analytical approach, create algorithms, mixture of engineering and formal sciences	Engineering methodology, understanding of processes and data, iterative approach, bottom-up or top-down, holds aspects of analytical thinking and natural science approaches	Experiment under controlled conditions, hypothesis driven, starts with established method, adapted to experimental hypotheses, also develops completely new techniques	Applied research approach with clinical studies and clinical treatment practice, hypothesis driven, top-down

	Finite Elements	Computer Graphics	Medical Computer Vision	Biomedical Engineering	Molecular Biosciences	Radiology
Contribution	Deduction and proof for new theorems, either special solution to applied complex problem, or new technique to general simple solution,	Technique, algorithm, system	Algorithm, technique,	New models, which are superior to an old one in at least one specific case, model is solved computationally	Answer to research question, possibly new technique	Answers to study questions
Evaluation	Proof	Weak evaluation by demonstration, strong one by quantitative measurement (runtime or user study)	Evaluated for capabilities as well as correctness, speed	Proof of concept, better judged in measurable quantities	Interpretation of results done by the experimenter	Statistical evaluations

	Finite Elements	Computer Graphics	Medical Computer Vision	Biomedical Engineering	Molecular Biosciences	Radiology
Significance	High if applicable to a large class of problems or excels in quality	Large innovation, wide application, obvious visual differences	Enabling a new technique, much better in information recovery	Wide innovative steps or solutions to widely applicable questions	Every aspect of science is important for the whole picture of life, but not Every topic is important for the human being.	Study on very new research questions
Good Results	Includes proof, special cases often before general approach	Theoretical explanation together with implementation	Especially a correct evaluation is vital	Thinking with applying	Provide clear, traceable and reproducible answer to a question	Mathematically significant results
Step Size	Often very special cases before proving general approach	The larger the better	The larger the better	Large steps preferred	Not necessarily large	Very limited due to ethical reasons

Table 3.1: Comparison of participating research disciplines in the elaborated criteria

3.5 Grouping participating disciplines

When answers for specific questions are very similarly, researchers in the respective disciplines act similar and have an implicit understanding for other researchers' work. We see these similarities and differences more clearly in Table 3.2, which sorts the research disciplines according to their main answer for a specific criterion. In some cases, a discipline holds aspects of both groups and therefore is listed in both groups and printed in italics.

In Section 3.1 we learned that interdisciplinarity demands combining not only the topics but also the methodologies and evaluation strategies. Especially evaluation strategies of participating research disciplines still have to be valid for the specific part to solve the complete question. So, not only do differences have to be tolerated, but for conflicts arising from differences in approaches a solution needs to be found.

3.6 Combining the research to achieve interdiscplinarity

We evaluate Table 3.2 to identify key design strategies for our research approach to the interdisciplinary question as well as towards the exploitation of research results. Looking at the topic and context of the research questions addressed in the participating disciplines biomedical engineering, on one side, and radiology as well as molecular biosciences, on the other side, research very similar topics. So though their methodologies differ they are looking into the same parts of the research question and trying to make similar progress. The contributions for those disciplines still differ widely, as biomedical engineering looks into the creation of a technique or equation, while the medical disciplines look into answering specific questions for the sake of knowledge. So it makes perfect sense to have all those disciplines participating in the project with their independent focus on the same research topics. It also makes sense to approach the modeling challenge from two sides — once from the bottom up approach of looking into single effects and modeling those and once using the top down approach of explaining the complete situation in total with a statistical approach. In the context of our application case, the bottom-up approach was performed by the biomedical engineering expert, while the top down approach was achieved from applied computer graphics.

The validation of the simulation result is the question for evaluating the research result. In natural sciences, the result of the data taken is interpreted, in engineering sciences it is important to measure the error. Both strategies need to fit into one result for the overall goal. Therefore, we apply computer graphics to show measured results together with

Topic/Context	
Computation and Numbers	Life Sciences
Finite elements Computer graphics Medical computer vision *Biomedical engineering*	*Biomedical engineering* Molecular biosciences Radiology

Applied Method	
Bottom Up	Top Down
Computer graphics *Medical computer vision* *Biomedical engineering* *Molecular biosciences*	Finite Elements *Medical computer vision* *Biomedical engineering* *Molecular biosciences* Radiology

Contribution	
Create Technique	Answer Question
Finite elements Computer graphics Medical computer vision Biomedical engineering *Molecular biosciences*	*Molecular biosciences* Radiology

Evaluation	
Quantitative Measurement	Interpret Result
Computer graphics Medical computer vision Biomedical engineering	Molecular biosciences Radiology

Significance	
Widely Applicable / Benchmark	Specific Study Question Relevance
Finite elements Computer graphics Medical computer vision Biomedical engineering	Molecular biosciences Radiology

Good Results	
Theory and Application	Meaningful Statistics
Finite elements Computer graphics Medical computer vision Biomedical engineering Molecular biosciences	Radiology

Innovation Step Size	
Large Steps	Small Steps
Finite elements Computer graphics Medical computer vision Biomedical engineering	Molecular biosciences Radiology

Table 3.2: Grouping of research disciplines according to similarities. Whenever a discipline stands on both sides it is printed in italic

predicted results. We compute quantitative numbers but these alone are not satisfactory if you want to interpret the result and look into deficiencies. So the graphical presentation closes the gap to the overall understanding of the applied research question and this is also reflected in the setup of our application case as described in Chapter 4.

The research methodology applied is very different for some disciplines. Especially computer graphics, which is used to bridge the gap between engineering and medical sciences, work in an opposite direction. Therefore, only complete results can be presented to the other discipline here. Intermediate results will always show the wrong end of a discussion to the other discipline, as intermediate for computer graphics with its bottom-up approach means "the bottom" (some software tool, which is not yet integrated) is already there, but nobody knows where it will end, while for the medical sciences it means "the top" (the right question) is already there, though there is no consequence and possibly no implementation to this achievement yet. For the research presented here, it means that the part dealing with the validation (Chapter 5) shows both the top down approach and the created computer graphics tool.

The disciplines also vary in their judgement on when research makes a significant contribution to the respective area, which leads to misunderstanding. That means, results that are very important and highly significant to the overall research collaboration are not

important or significant to the single participating discipline. Therefore, every discipline has to create bigger results, than are necessary to the collaboration alone, if they are to show their success in successful dissemination in their respective community. Even worse: good results for the statistical approach demands a lot of processing of data where for some disciplines the proof of principle is enough. So some disciplines have to invest more time to satisfy the partner's requirements for good research and not only their own. The only chance of keeping this explosion of effort within the realms of possibility is to aim at automation as high as possible for the processes involved in generating answers for statistics. As for our application case a full automation of all processing steps diminished the quality of the result so significantly that it could not be achieved. We aimed still at processing with as few manual steps as possible. This was one reason for acquiring the best possible data for processing in the validation chain (compare Chapter 7).

Last but not least, the step size for innovative aspects is very different between the participating disciplines. So what are publishable results in one discipline are considered below the minimum as an interesting novelty for the other discipline. A good possibility for dealing with this gap is to publish separately for most of the work in the participating disciplines. In the worst case, this means publishing similar findings twice — once with the emphasis of one discipline, once with the other discipline's emphasis. Dissemination of the results is still ongoing and situations like this will probably arise in the future.

All these aspects can be found in the design of the research collaboration as well as in the single elaborated results in the following chapters of this thesis. Most important here is the overall approach to the research hypothesis addressed in this thesis. As the whole approach was interdisciplinary, all the above elaborated aspects can be found in the following parts of this thesis.

3.7 Summary and conclusion

Nowadays, solving real world questions leads to interdisciplinary research tasks. These tasks can only be solved if the partners from different disciplines work closely together. This is a challenge in communication between the cooperating partners. Communication is easy if the context is similar for the partners. As explained above this is not always the case. Most important here is to understand not only obvious differences but rather implicit differences. Being aware of the respective aims, methodologies, etc. allows breaking the overall question down into parts for every participant without violating their respective approaches.

Interdisciplinary research demands not only having joint research interests and topics, but also interwoven methodologies to address joint research aspects. So while the research methodology for the overall collaboration was oriented on the end-user of the research result, the methodologies of the (sub-)disciplines had to be integrated in all the parts. This approach leads to the necessary interwoven approach. So it is especially important to understand differences in methodologies to arrive at clear and fruitful communication. We identified key design strategies for our approach to research on simulating radiofrequency ablation by computing a validated model for the process. These strategies were the underlying principles in the design and work carried out for the research project IMPPACT described in Chapter 4. They allowed us to bridge the communication gap and led to successful interwoven research on the topic.

Chapter 4

Image-Based Multiscale Physiological Planning for Ablation Cancer Treatment

Contents

Building a planning application for the RFA intervention based on a physiological model is a multi-disciplinary research question. It demands close collaboration from many different research areas. Therefore, an interdisciplinary research project with exactly this research topic was created. The following sections describe the research project, the overall plan, and short sketches on what research needs to be performed for each project participant to gain the full solution.

4.1 Motivation

The project by its nature was set up to deliver scientific understanding of a physiological process and integration of the findings into an engineering result: the Intervention Plan-

ning System (IPS). The bottleneck on the way toward the patient specific planning tool is our limited ability to computationally model and simulate the process. Our limited understanding of the processes during tissue heating and, ultimately, tissue death as the result of that heating, hinder the modeling task. Specifically, a model has to prove that it is capable of computing the process correctly. The IMPPACT project aims at opening this bottleneck by generating a new insight into the physiological processes and biochemical reactions in the context of tissue heating. The main challenge to success lies in verification and validation on every modeling level from single aspects to the complete overall process. Otherwise, any model prediction is pure fiction and unusable in clinical practice.

The project tackles the challenge of predicting the RFA process by computational modeling and simulation. All modifications as well as simulation results are validated in phantom and animal experiments and compared to ongoing clinical patient treatment. A workflow oriented approach guarantees its suitability for clinical practice. Overall, the project aims at bringing RFA from its last resort status up to the treatment of choice for hepatic cellular carcinomas and liver metastases. By integrating modeling, imaging and visualization in a full simulator, IMPPACT creates an IPS* as a clinically relevant application.

4.2 Objectives

The project's major objective is the creation of an IPS based on a patient specific physiological model of the liver under local hyperthermia intervention. Furthermore, an augmented reality training simulator is created to teach surgeons optimal RFA application before they start using this treatment.

4.2.1 Multiscale modeling as part of a new bio-heat equation

The established bio-heat equation was determined for the resting human forearm and does not match the RFA process. Although the heat dissipation in the liver is a macroscopic effect, it is essentially determined by features that can only be found on the microscopic level of cells. In particular, the observed changes of the necrosis zone shape for a long duration after the intervention have not yet been included in any prediction model. They originate in cellular behavior during heating and cell death. Understanding of these effects is essential for predicting treatment results. To meet this challenge, the project examines

*Intervention Planning System

equivalences between macroscopic features and microscopic findings, their importance and characteristics measured and modeled accordingly. So modeling of the ongoing process is performed on two scales — microscopically (cell changes, physiological changes, cell death) and macroscopically (blood flow and temperature). Both levels are independently developed and the results integrated into a common system.

While the microscopic level is mostly dominated by setting up experiments and asking for macroscopic equivalences in findings, the macroscopic level is dominated by physically based, but phenomenologically oriented comparisons between simulation results and macroscopic findings. Both together tackle the problem from different sides.

Furthermore, currently used constants in the established equations for modeling the RFA process are in fact not universal constants but patient specific parameters. There exists no validated simulation of a real situation where computation is compared to experimental data. Hence, one objective of the project is to develop an equation that will describe a validated model, which fits reality and includes patient specific parameters and microscopic as well as macroscopic effects.

4.2.2 Computation of simulation results for interactive exploration

Any simulation model for a real organ has to rely on finite element analysis and is therefore computationally very expensive. In our case, the necessary multiscale simulation approach for modeling the RFA process correctly leads to numerically solving partial differential equations in 3D. Interaction with the final application is highly desired, as the intervention planning process is interactive in nature. The solution to this challenge lies in accelerating the FEM solving as well as precomputing a set of solutions. Results are handled in a flexible solution space to allow interactive planning and visualization of treatment results.

4.2.3 Accurate reconstruction of identifiable anatomical and pathological structures

Image processing as the basis for physiological simulations has significant new requirements compared to image processing for volume rendering. For IMPPACT, the results from animal experiments are used as the ground truth in building a verifiable computational model. Here most important is the *accurate* reconstruction of *identifiable* structures, which can easily be associated with physiological properties. As segmentation of the liver and its inner structures cannot be achieved fully automatically in good enough quality, a semi-automatic image segmentation product is used to achieve manual refinement of automatic

segmentation to a level with acceptable accuracy. A special emphasis lies on the fusion of image processing results with results from histological examination.

4.2.4 High level validation

The most interesting research question in IMPPACT concerns the construction of a validated model for computing the RFA process on a physiological basis. Validation of the model's prediction needs to be achieved especially on the same level of complexity as the final planning application — the top-level which comprises a complete medical procedure.

RFA is a medical intervention which is used in clinical practice. At the same time it is subject to medical research, since effects that determine lesion shape and size are not completely understood and predicting the treatment result is therefore difficult. Medical research tests hypotheses in studies on phantoms, animals, or in patient studies. The measurement of correctness for knowledge to be established in the community is the statistical evaluation of observations for test cases in a study.

Engineering uses techniques and methodologies to compute results. In the case of establishing a predictive model for RFA, a physiological model of the human body is established in the form of equations and computed to predict the treatment outcome. Validating an application that simulates a medical intervention therefore has to be achieved in a manner that is accepted methodology for the participating engineering sciences, otherwise the application will not deliver any reproducible results. At the same time, the application aims at being used by the medical community and therefore has to be validated according to medical standards or else the validation will not be accepted by this community.

Creating a tool for validation on the highest level by visualizing treatment results together with simulation results is a computer graphics challenge. Parameters and equations are not only evaluated but also modifications proposed by visual comparison of treatment results with the simulation. This, in particular, allows a macroscopic modeling approach to tissue parameter estimation and the influence of anatomical structures. The created model provides input to the clinical practice, whereas feedback from the clinical practice in turn supports the modeling. Visualization is a suitable method for establishing communication between these different research areas. By involving both research areas in the creation of the model, confidence in the models prediction is established.

The final model created in IMPPACT is fully verified and validated at several development stages (in phantoms, animal experiments and with patient data). This validation strategy not only guarantees correctness of basic research results (by phantom or animal

experiments), but also their correct application for the complete prediction model (by cross-checking with patient images from ongoing treatment).

4.3 Concept for modeling, animal experiments, and studies on patients

The IPS created in IMPPACT is a clinically relevant application that is based on fully validated modeling. Modeling therefore happens on two levels: macroscopically (needle geometry, influence of vessel trees, etc.) and microscopically (cell reactions to heating and cell death). Both modeling aspects rely on experimental findings: animal studies on the impact of external circumstances and specific tissue related factors; patient studies as cross comparison to relate the modeling with the ground truth from the patient treatment while developing a patient specific model. Figure 4.1 shows a rough overview of the data flow in an example of one experimental cycle.

There are four essentially different areas of research involved in the project:

1. Medical research on pre-clinical RFA-experiments in animal models and on cell lines provides:

   - a comprehensive image record of the ablation process for image processing and intra-operative measurements of impedance and power for the biomedical partner in the physiological model;
   - a histological investigation of tissue for image recording and tissue characteristics to be used as input by the biomedical partner for the physiological modeling.

   In addition, images collected from clinical RFA-treatment on patients provides ground truth knowledge on the process of actual ablation and its effects on the patient tissue. This data provides feedback to the physiological model necessary for its refinement. Studies on patients do not concern new treatments but only taking images during normal treatment.

2. Image processing focuses on algorithms for semi-automatic analysis of multi-modal image data acquired before and after the ablation, as well as in follow up checks. These data are used to construct the physiological model and to validate its predictions.

3. Bioengineering develops the patient specific physiological model for the RFA-treatment and its follow up processes. The modeling takes input from the medical as well as image processing research. Computational aspects of the modeling are optimized through FEM implementation.

4. Predictions of the biomedical model fused with multi-model image data are visualized in the IPS as well as for high-level validation.

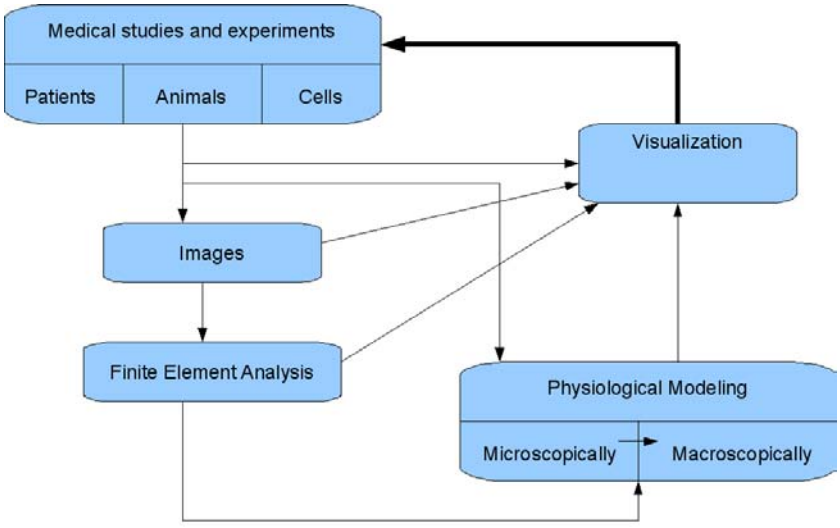

Figure 4.1: Illustration of the data flow in one experimental cycle

4.4 Novel features of the complete project

Unlike other intervention planning systems which model an anatomical organ (e.g. patient specific geometrical structures), IMPPACT focuses on modeling a physiological organ including the metabolism and patient specific tissue properties. This alone is a huge step forward as compared to the state-of-the-art intervention planning systems that do not address this issue.

To achieve this goal, the project demands and introduces a number of important novelties from different research areas. Not all have been addressed in every detail up to this point and not all of them are part of this thesis.

- First and foremost a new version of the bio-heat equation is elaborated encompassing micro-perfusion, coagulation, and cell death microscopically as well as macroscopically. The new modeling equation also models patient specific physiological factors.

New terms that are necessary are created by the biomedical engineering partner and currently partly available. Pure macroscopical findings on boiling cell fluid, the needle geometry, as well as the ablation protocol and a controller to steer the ablation are researched at the author's host institution with the author's participation. The relevant results, are presented in Chapter 6. Current results achieved by the biomedical engineering partners concern micro-perfusion, coagulation, and cell death. This cell death model is extended by the biomedical engineering partner to compute long term effects like cell death due to chemical reactions for weeks after the intervention. These terms will also be incorporated into the macroscopic prediction model.

- The elaborated physiological model demands a multistage experimental validation. Here, the medical partner performs experiments on cell cultures and establishes a tumor model in Styrian domestic pigs. Wherever the numerical solver has to incorporate new solving strategies these have to be mathematically verified to work correctly by the participating numerical expert. Finally, the complete prediction simulation is visually compared to the result of the intervention in a medical study. The necessary tool for this was created at the author's hosting institution with participation of the author. Results are presented in Chapter 5.

- The visual comparison of measured and simulated data is achieved by continous visualization of both types of results at interactive frame rates. This multi-variate presentation is an application of the tool presented in Chapter 5. Techniques for steering the user's perception towards interesting details and events are currently under research at the author's host institution with participation of the author. Possibilities here open a wide area this document therefore leaves results for future work.

- The required experiments fit the computed situation and therefore results can be compared in a validation study. They are designed by engineers and medical doctors in cooperation. An complex example for this experimental definition has been created by the author in collaboration with the medical partners and is provided in Chapter 7.

- Because the application is planned based on radiological images but its result can only be seen in histological findings, both imaging modalities have to be processed for further use in the validation procedure. While the data is again acquired in a medical procedure and therefore by a medical partner, two computer vision partners

are involved in the image processing. One of these partners specialized in processing radiological images, one takes care of images presenting histological findings. The overall procedure was developed by the author in conjunction with the medical partner. Chapter 8 provides results to this challenge.

- The final design of the IPS system is oriented on needs for clinical day-to-day work. It is therefore based on results of a feasability study, consisting of a work flow analysis and the design of a new workflow. The new workflow seamlessly integrates the IPS into the clinical workflow. This research was performed by the author together with the medical end user. It is not presented in the context of this thesis as it concentrates on the final shape of the prediction application, not on the validation process.

Together all these efforts makes it possible to predicting the final shape of the necrosis zone in clinical relevance and lead to the IPS. The complete project falls into three major phases. The first phase created tools that allow high-level validation of respective simulations. The second phase deals with adapting model equations to incorporate new medical findings and new elaborated equation terms into the simulation. The third phase consists of the application to patient data and creation of the IPS as well as the augmented reality simulator. The phases presented in the context of this thesis concern the validation step, especially the high level validation for the complete procedure. Implementation of the IPS and tests for the clinical case are left for future work.

4.5 Computer graphics research aspects in IMPPACT

The strong emphasis on computer graphics for the whole IMPPACT project naturally leads to a bias towards fundamental research questions in computer graphics. These aspects can be found throughout the whole project and in every one of the three major phases.

4.5.1 Visualization of probabilities, uncertainties, and errors

Visualization of processed registered and fused images together with simulation results is the key to model validation. It allows human evaluation of simulation quality and therefore top level validation. This document shows the creation of the validation study setup, the necessary tools and the processing chain that support this validation step. The most fundamental computer graphics question involved in this context concern the created multi-*

raycaster as presented in Chapter 5. In addition to this tool a clear and intuitive graphical presentation for analyzing all simulation results and matching experimental findings is implemented. The solution concerns multidimensional multivariate interactive scientific visualization, which we leave as direct consequence for future work.

Images from up to 9 consecutive CT scans and a set of histological slides (for animals) or else images from three consecutive CT scans and 1 MR image (for patients) need to be visualized in close spatial relation but without occluding each other. Achieving this demand at continuous interactive frame rates leds to the development of new visualization techniques for probabilities in multi-variate data through optimization of algorithms and data structures for volumes. The new visualization techniques will allow simultaneous examination of multiple overlapping volumes as well as visual judging of measurement errors and simulation results together. This technique is currently being developed at the author's host institution with the author's participation, but left as future work as far as this document is concerned.

4.5.2 Virtual reality planning application

Based on the interactive visualization tool for validation, the intervention planning application is created. This application allows interactive needle position testing and supports different ablation protocols. Now different simulation results can be visualized together and compared. Newly developed visualization techniques allow comparison of different pre-computed simulation results (different shapes of necrosis zones and isotherm-surfaces, etc.) with the aim of giving a skilled medical doctor the ability to plan his/her optimum needle position interactively and consequences from possible difficulties in performing the procedure are foretold. The planning application has been created at the author's host institution in cooperation with the author but is not included in this thesis as it does not primarily focus on the validation challenge.

4.5.3 IPS user interface design

The screen layout and user interaction for the final application had to be designed. We first designed mock-ups and evaluated them together with the end-user — the medical partners. A suitable user interface was implemented that fits the needs of medical personnel in clinical practice. The user interface was then attached to the underlying virtual reality planning tool. A special emphasis was put on identifying the best suited interaction techniques for easy control of the application and the interactive planning functionality

for the needle position and orientation.

The IPS will be examined in future work at the medical partner's institution as soon as the complete biomedical modeling functionality is achieved. Most important here is matching the end-user's needs in a hospital or clinical environment. Therefore, user studies and quantitative evaluations have to be performed and the findings reported back to the development team to find solutions for any inconveniences arising. This part will be elaborated in the context of the IMPPACT project but will be left as future work.

4.5.4 Augmented reality training simulator

Together with the medical experts, a training simulator with suitable user interface will be developed. Every stage of the simulator needs to model different aspects of the real intervention and therefore user interfaces differ in requirements. After identifying the different training units an implementation based on the planning application will be created. Creation of the augmented reality simulation is in this document left as future work.

The basis of the training simulator is a phantom, a physical replacement for the patient, as well as medical data acquired in clinical practice. As the dataset has not been acquired from the physical phantom the used data has to be fitted to the extensions and features of the phantom. The result will be developed to fit the requirements determined by medical personnel.

The training simulator will encompass several stages of the procedure in different aspects. The content for every stage will be developed with the end-users and then implemented. If necessary, different setups will be elaborated. The developed simulator can then be evaluated for its suitability in the given task by performing user studies (qualitatively and quantitatively). The augmented reality simulator as envisioned here will be part of the IMPPACT's project third phase. For the content of this document it is therefore described as future work.

4.5.5 System integration

All the individual parts needed by the IPS will finally be integrated into one system that serves the medical personnel for planning the intervention. Starting from a work flow analysis and the user interface design, the application has to be constructed for everyday use in clinical practice. A detailed analysis of the suitability of the solution will then be carried out. Necessary revisions and refinements will be implemented and presented as alternatives. Any difficulties or possible deficiencies will have to be dealt with and any

errors found in tests eliminated.

First tests of the integrated application will be performed by engineering personnel to ensure a level of stability and correctness before beginning tests with medical personnel. The first tests with the end users should be simulation tests involving a physical phantom as replacement for the patient. At this stage, the development of the training simulator and the IPS can be implemented simultaneously and tested together. User studies have to address both the correctness and suitability of the IPS in clinical practice and the suitability of the training simulator as an educational tool.

Once the IPS has passed the phantom tests and is ready to be used, a test series with animals should ensure correct working under hospital conditions. The final all-deciding test will be in clinical practice in the treatment planning situation. As the treatment is already performed in clinical practice with much less planning and more risk than with the IPS, introduction of the IPS will be an addition and is therefore ethically acceptable.

While this chapter presents an overview over the complete IMPPACT project, this thesis deals with the validation of the biomedical model to be developed in the project. Achieving this validation for a model usable for intervention prediction is a computer graphics research topic. Therefore, the following chapters present the research results on the way to establishing top-level validation for a model predicting the result of the medical intervention RFA.

Chapter 5

Validation through visualization

Contents

The IMPPACT project as a whole presents many different challenges in many different research areas. Together they form the necessary work to produce an application for RFA treatment planning. The core of any planning application lies in the predictive power and therefore the correctness of the underlying model. For RFA, the model cannot be derived theoretically as the process is not understood well enough in the underlying sciences (biophysics, biochemistry, etc.). The model therefore has to be found by adaption to empirically gathered findings.

Bridging this gap in accepted methodologies can be achieved by utilizing computer graphics. The simulation prediction is computed by engineers. Comparing the simulation's prediction to treatment results in medical studies can be done by a medical expert, provided a suitable visualization and comprehensible processing of the medical data can be achieved. So creating a validation application is a computer graphics challenge.

5.1 Data processing

The overall process is a complex procedure and so is data processing to gain information as ground truth from the gathered medical data. Before a top level validation can be attempted, every single participant in the processing chain has to validate or verify

their respective data processing tools. In this way the complete processing chain can be evaluated for correctness.

5.1.1 Processing chain for RFA simulation

We take a look at the data processing chain for a validation study to identify the blocks of which it consists. Furthermore, with a close look, we can see the connection in between the building blocks. The connection between the blocks has to be close without leaving a gap. Otherwise the chain will not be complete. The processing chain for the RFA simulation is presented in Figure 5.1.

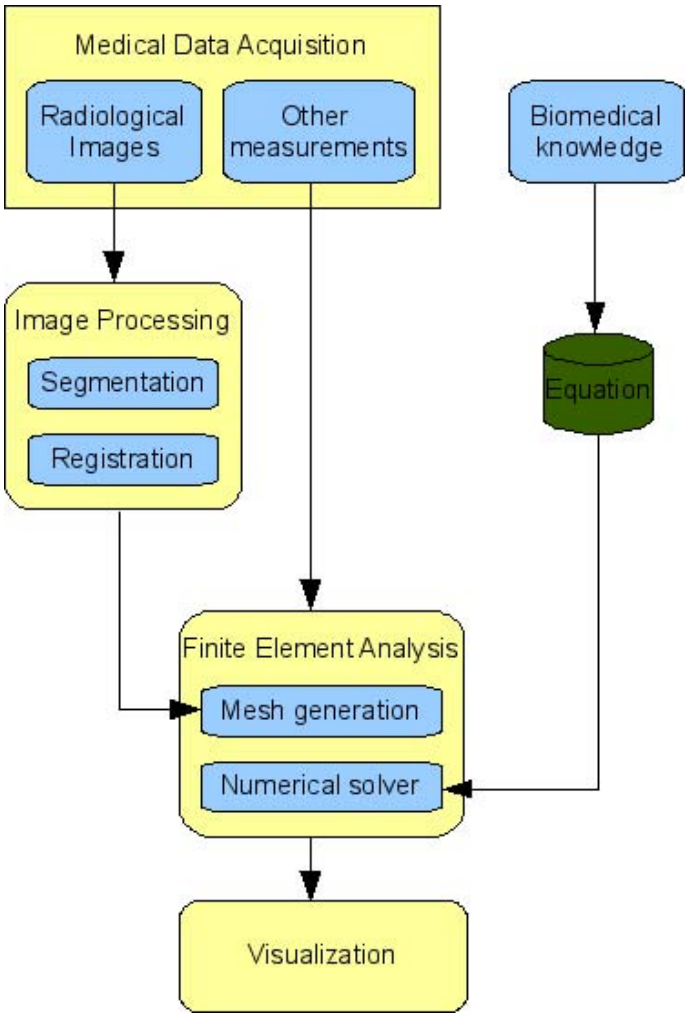

Figure 5.1: Data processing for RFA simulation

Computational prediction of the physiological process RFA takes medical data as input.

The data is acquired by medical specialists who contribute their expertise. It is then processed by computers so that it can be used as simulation input. Whenever the data collected is imaging data, the processing concerns computer vision. Other data acquired in this procedure is not as complex and therefore does not concern a specific computer science discipline.

To achieve a simulation the governing equations describing the process need to be defined in detail. The insight into this is gained in the areas of biophysics or biomedical engineering. The equations are partial differential and do not have a closed analytical form. So numerics are applied to solve the equations. Finite element analysis is the most obvious choice here. The acquired and possibly pre-processed data is used as input in the computational simulation of the process. The information gained from the images is used as geometrical input and further processed by a meshing tool. The solver applies numerics to compute the variables of interest in the simulation. The result of the simulation can then be visualized to understand the outcome of the finite element simulation. This concludes the whole processing chain used for RFA simulation computation.

5.1.2 Processing chain for measured medical data

From a medical perspective, foremost radiology and — as the outcome of the intervention is not seen in radiological images — histological examinations of the tissue are necessary. Furthermore, otherwise collected data such as temperature or blood flow might be of interest, as these could explain discrepancies in simulation and real data. These other values should be taken for the study whenever judged as being reasonable by a medical expert and visualized as well.

Even real data collected in medical studies needs to be processed by engineers to be available for visual comparison. Part of that data processing is equivalent to the input into the simulation. However, data showing intervention results requires more data processing blocks to prepare the data for visualization. Figure 5.2 shows the processing steps necessary for visual presentation of the data acquired in medical studies.

Radiological images can be visualized by direct volume rendering. They are taken in regular grids with scalar intensity values, which hold the information. They can also be processed by computer as explained for the data simulation processing chain. Histological images are acquired on sections through a tissue volume. To create a volume out of these sections image processing has to be applied. The created volume could then again be visualized by direct volume rendering. But whenever medical data is processed to form

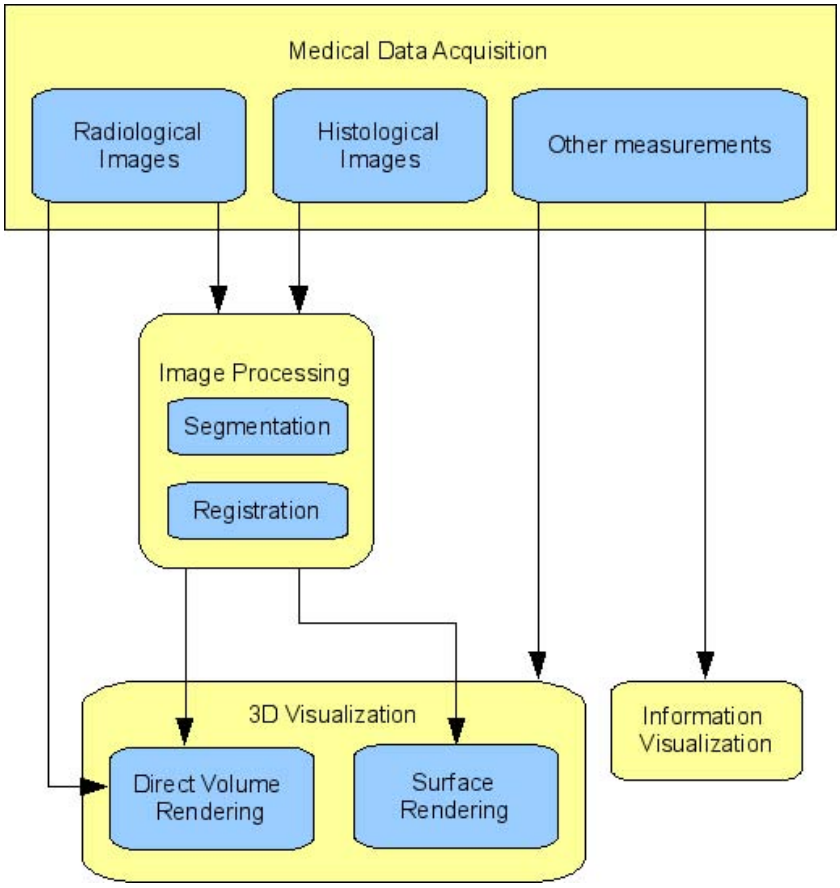

Figure 5.2: Data processing for visualizing data acquired in medical studies

a surface, surface rendering is possible and might be more suitable for conveying the information. All imaging data needs to be fused and presented in a co-located way. It is acquired for the same subject at different points in time and therefore builds one complete dataset per study object.

Other data acquired in the procedure are taken sometimes automatically, sometimes manually. Examples are measurements of blood pressure or the readings from the RITA generator during the procedure. This type of data is abstract and typically presented in measurement values with or without given measurement errors. The data can be presented side by side with the rest in any abstract fashion. Still a connection with the rest of the data, especially the measurement points, if any exist, has to be established. So a loose coupling is the required minimum. But of course the data could also influence the presentation in the 3D visualization — for example the coloring at some specific point.

Most of the acquired data is volumetric and therefore demands a 3D visualization.

Together with presentation of the abstract measurement data this gives an overview of the complete real data as acquired in the medical procedure. This concludes the processing chain for the recorded measured data. Comparison of the simulation and the treatment result can only be achieved by visual judgment by an expert. So computer graphics has to present the simulation as well as the recorded real data in a form that allows discovery of equivalence and discrepancies.

5.1.3 Correctness of building blocks

To validate the correct processing of the whole processing chain every single step needs to be validated according to the methodology applicable to its respective research area. The first step concerns the acquisition of medical data. In our case the acquired data is radiological images and possibly laboratory data. For each of the methods applied (CT, MRI, medical laboratory) the respective methodology has already been elaborated and its validity as a procedural step has been accepted. Otherwise it would not be available in medical research. We can therefore presume that the acquired data provides the information that is typically assumed in the medical community for this type of data.

Medical data has to be processed to be usable for simulation computations. While laboratory values just need to be provided (in their original form, e.g. tables with numbers) images are processed using computer vision algorithms and methodologies. An image segmentation algorithm is evaluated by comparing the algorithm's result to the result an expert achieves when classifying voxels by hand. Technically the comparison can be done on every image but the procedure is very time consuming. So relying on an already evaluated algorithm and applying this method to images taken for this specific validation is a practical solution. For processing information from more than one image the data has to be fused. This step is performed by applying image to image registration, which is evaluated by comparing the warped image to the target image. Subtraction on voxel base shows the differences.

Finite element analysis is performed in two steps: meshing the geometry and solving the numerical computations. The typical mesher and solver toolkits are mathematically sophisticated software tools and libraries. The accepted method for mathematical research validation is proof by deduction. Meshing is done using an engineering approach. The mathematics lies in the solver toolkit. Its validity therefore has been proven at least once by following every computation step mathematically and proving the result is correct before being put to actual use. For the research performed here, an existing mesher and

solver toolkit can be applied and their validity taken as granted. The solver then has to be built using the solver toolkit and its validity concerns the question of whether the solver really implements the equation that was given as input by the biomedical researchers. This step is performed as implementation like any other programming and involves checking and debugging like any other computer program.

The correctness of biomedical equations is validated by comparing the computed result to real world examples. This validation step is rarely researched for complex medical cases as these are hard to judge in total. Single aspects are validated by looking into artificial setups. However, these do not reflect the real medical situation and therefore hardly deliver results applicable directly in real life. A rare example is the bioheat-equation, where fundamental research has been achieved by comparing computations to the real situations. But also in this case the process under examination is rather simple.

Computer graphics presents the processed data to the human expert in a fashion best decided by the expert. Errors here concern wrong visual appearance like miscoloring or deformation. They do not concern a miscategorizing of data. Judging the visual output is the only measurement for correctness here and has to be discussed between the developing researcher and the experts using the graphics. Typical test cases need to be found and demonstrated so that trust in the software can be established. The whole processing chain ends with taking a final look at the result of the simulation computation compared to medical data. So when every single step in the processing chain is known to work correctly, the visual presentation of the result will show the computed simulation for the specific input case as well as the treatment result.

5.2 Top-level validation through visualization

Numerically computing the simulation is time consuming and cannot be done at interactive frame rates. But to be able to judge the computed result by comparison with real data the visualization needs to work at interactive frame rates. After all, a user needs to analyze the data, to rotate volumes or otherwise adjust presentation. So the simulation does not have to be computed in real time, but it has to be explored in real time. From a computer graphics perspective, the challenge in the validation of the procedure concerns showing many different data sources together using different volume visualization techniques. So computer graphics must deal with a huge amount of information in real time.

5.2.1 Multi-* raycasting

From a systems point of view, the data to be visualized is

- *multi-dimensional* data of at least four dimensions: the acquired data in the medical procedure is volume data and therfore has 3 dimensions. Furthermore, the RFA procedure generates changes over time which are especially relevant and visible in the simulation of the process. So here a fourth dimension is needed.

- originally acquired in *multiple volumes*: for the validation step of the procedure CT scans are acquired at multiple points in time. These represent multiple volumes from which information needs to be observed at the same time. One approach is the graphical presentation of more than one volume together.

- *multi-model* data: This data is acquired in different modalities. For the IMPPACT project, the image acquisition from patients for example holds CT and MRI scans which present two different modalities.

- *multi-variate* data: Every voxel in the volume holds different values and different data presentations. Especially, data is taken with measurement errors and therefore holds more than one value in one position. Simulation data generates a huge amount of information for every position and point in time. Already the physical constants in the equation are unknown and measured with errors. So every voxel is associated with temperature, probability for coagulation, probability for cell death, etc., but the input constants have measurement errors, as the exact model equation is not known. So, every value comes with a possible error or confidence interval.

- acquired on *multi-scales*: in the course of the study, data is acquired on different scales. The obvious example is histological data as well as CT data. Both are acquired for the same study subject and relate to each other in 3D space (and also in time), but differ strongly in magnitudes of represented physical size.

- *multi-resolution*: Different images can be acquired with different voxel sizes. For IMPPACT the voxel size differs between CT scans and MRI scans for patients. But of course the voxel size also differs for histological data and CT data. Even simulation results are not generated on a regular grid and have to be mapped to a regular grid with a suitable voxel size.

At the very basis of all the above described features stands a system that allows visualizing medical volumes together with the computed simulation results at interactive framerates. Direct Volume Rendering (DVR) here comes in as the most promising approach, as it introduces as few preprocessing errors as possible. DVR in real time is a challenge for directly programming the GPU (Graphical Processing Unit). In our case we seek a DVR approach fulfilling the above described capabilities, which can also handle intersecting polygonal data.

5.2.2 Multi-volume raycasting

Our preferred way to cope with overlapping volumes is to extend the commonly known raycasting integral

$$\int_b^a g(s) exp\left(-\int_a^s \tau(x)dx\right) ds \tag{5.1}$$

by piecewise homogenous ray segments through the volumes. Then the integral can be calculated within these volume segments with improvements like early ray termination or empty space skipping. To include arbitrary geometry correctly and to obtain homogenous regions, intersection calculations have to be performed. This is computationally not feasible for real-time applications. Therefore, depth peeling is the obvious choice. The depth peeling step for multi-volumes is outlined in Figure 5.3.

The remaining step for our approach is to determine which homogenous volumetric region belongs to which three dimensional volume texture. This is done by a separate assignment of orthogonal coordinates for the volumetric objects and geometry. An intersection of two objects is represented as logical OR of the object's coordinates. A simple example for that coordinate scheme is also outlined in Figure 5.3. With these assumptions also geometry can be handled. If a ray hits the next volumetric region, and it is a polygonal object, it only has to accumulate the object properties such as color to the current ray's value.

Multi-volume rendering is harder than rendering single volumes, because it requires handling of intersections and per-sample intermixing. Resampling the volumes to a single coordinate frame is not desirable because of the resulting loss in quality (or increased memory requirements) and limited flexibility of layouting. Another requirement of advanced applications is the combination of volumes with polygonal meshes. Polygonal models are useful for embedding foreign objects or reference grids into volumes, but also to apply clipping shapes, highlight areas of interest, or display segmented geometry. We also note that

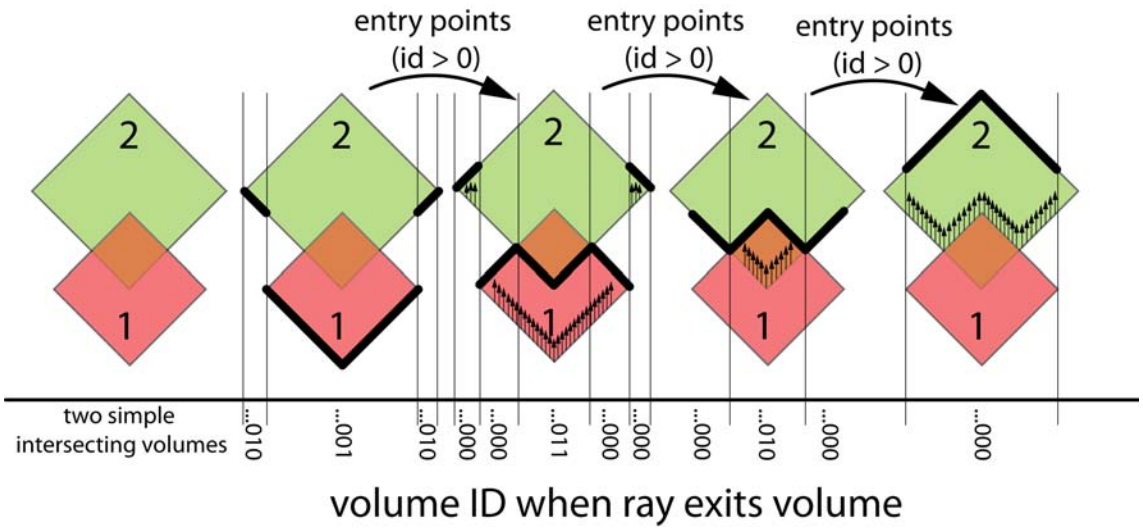

Figure 5.3: Illustration of the depth peeling step and the subsequent ray casting. Every time a ray leaves a volume, the corresponding ID of that volume is combined with a logical *or* to the currently valid ID. The current ID is then used during the traversal of each ray to determine in which volume the values have to be searched.

the intersection of the bounding boxes of multiple volumes is given as a polyhedron. Such an intersection of bounding boxes is useful as a conservative approximation of the region for which intermixing of the shading contributions of intersecting volumes is required. For expressiveness and convenience, support for polygonal structures should not be limited to convex shapes or opaque materials.

Since the raycaster kernel (transfer function and accumulation) is relatively simple, the bus traffic will become the bottleneck when aiming at more complex scenes composed of multiple volumes and polygonal objects.

5.3 Using many-core architecture

We investigated an approach suitable for current many-core GPUs, which overcomes the inefficiencies imposed by a fixed function pipeline. We employed the new Compute Unified Device Architecture (CUDA) [112], a C-like language for general purpose computations on the GPU.

A CUDA application consists of a large number of concurrent threads (typically more than 1000), which are grouped into tightly coupled thread blocks. CUDA offers several benefits which are relevant in our context:

- Within each thread block, data can be cached and exchanged with other threads with extremely high bandwidth (over 1 terabyte/second) and low latency (few nanoseconds). If an application with an existing memory bus bottleneck can be rewritten to utilize these resources, performance can be improved significantly.

- The programmer has detailed control over the execution configuration (number of threads, size of thread blocks, synchronization mechanisms) and can optimize these parameters for a particular application.

- The CUDA memory model is more sophisticated than its counterpart available in shader languages. The programmer can choose between different memory access units (e.g., texture and linear memory) and select the unit which is best suited for a particular task. Moreover, arbitrary write operations (scattering) are supported. This allows us to overcome the rather bizarre algorithms developed in the past to compensate for the lack of the scatter operation in shader languages.

Similarly to the OpenGL renderer described by Seiler et al. [137], we implemented a volume rendering pipeline based on polygon tiling entirely in software. This approach has complete control over the rendering process and executes an efficient sort-middle approach. Geometry is rasterized only once, and all depth samples are passed on to ray casting through on-chip shared memory, which is also significantly faster than global memory. Ray casting is coherently executed in tiles of 8×8 pixels with straight rays. Both geometry and fragment processing (ray casting) are executed in a massively parallel way using CUDA's multi-threaded execution model. The efficiency gained by this approach allows us to support a very general multivolume data model, thereby unifying a number of advanced volume rendering approaches.

5.3.1 Constructive solid geometry by raycasting

Our system is able to produce ray casting images of complex intersecting volumetric datasets with polyhedral boundaries. A recursively defined constructive solid geometry (CSG) structure composed of arbitrary volumetric polyhedra, i.e., two-manifold (possibly concave) triangular meshes with volumetric texturing serves as a memory model for our multi-* raycaster approach. Every polyhedron is associated with a volumetric 3D texture, a transfer function and a geometric transformation. This structure is similar to a volume scene graph approach [109] and supports any combination of the following use cases:

- Multiple intersecting volumes with individual coordinate systems and resolutions. CSG operations are used to distinguish overlapping and non-overlapping areas.
- Volumes can have arbitrary two-manifold bounding or clipping geometry. Concave polyhedra can conveniently be used as tight fitting bounding geometry. Selected areas in a volume can be highlighted interactively.
- Volumes can intersect and be intersected with transparent, concave geometry.
- Polygonal models can have volumetric effects, in particular they can be made of transparent homogeneous material (not just transparent surface rendering).
- CSG operations on a volume segmented into multiple regions with polyhedral boundaries can be used to assign individual transfer functions to each region. Each region can be transformed individually, allowing exploded views. Multiple instances of a region are possible for side by side comparison.

All computation is executed on the GPU, the only information that is received from the CPU for every frame is the camera position. The scene that represents the input to the ray casting procedure is structured in the following way (see Figure 5.4):

- Raw volume data from multiple volumes is represented in a volume atlas.
- Polyhedral objects consist of a triangular mesh. A polyhedral object can be concave, but must be two-manifold, so that the interior and exterior can be distinguished.
- A scene consists of a simple scene graph. Interior nodes are associated with CSG operations, whereas leafs refer to a polyhedral object as the boundary, a volume texture or single material property for the interior, and an affine transformation for global placement of the object. The transformations can also be animated. Instances can be created by referencing the same polyhedral object and/or volume texture more than once.

The ray casting algorithm follows the usual steps of a rendering pipeline: transformation of polygons, rasterization, and fragment processing. The latter is done in a pixel-parallel way per 8×8 tile and is responsible for traversing adjacent rays through the volumes stored as 3D textures. It therefore naturally exploits texture cache coherence.

Unlike depth peeling approaches, our rendering system traverses the scene only once. We implement all steps in CUDA software and therefore have access to all intermediate

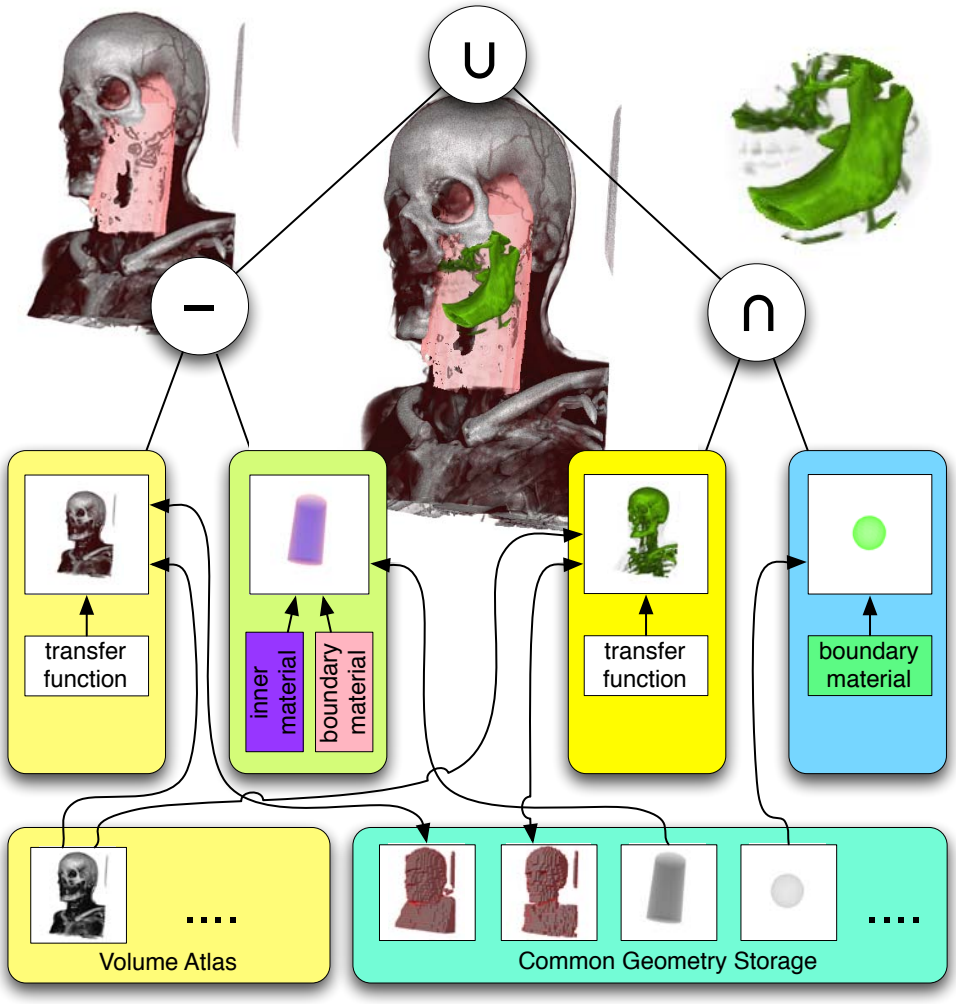

Figure 5.4: The scene graph consists of CSG operations and polyhedral objects with volumetric textures and/or material properties. Textures are stored in a texture atlas, polygonal geometry and volume boundaries in common storage, which allows for instancing. Note that the two bounding volumes of the head in the geometry storage are computed from different transfer functions.

results of the pipeline, which are kept in shared memory wherever possible for maximum performance. We still need two separate kernels (one for triangle processing and one for fragment processing) since the ray caster requires a sorted list of all relevant fragments at each pixel, which is only guaranteed to be complete after processing all of the triangles.

5.3.2 Implementation details

The triangle kernel then is responsible for geometric transformations, assignment of triangles to viewport tiles, and computation of coverage masks. The pixel kernel receives the fragments covering a pixel in arbitrary order. They must be sorted in the z-direction before they can be used to split a ray into homogeneous segments. The final ray casting and shading step requires the blending of several intersecting volumetric objects and therefore the efficient accumulation of the individual volumes' contributions along the rays. Support for concave bounding geometry simplifies empty space skipping. Volume samples are taken from a volume texture atlas. For an overview see Figure 5.5.

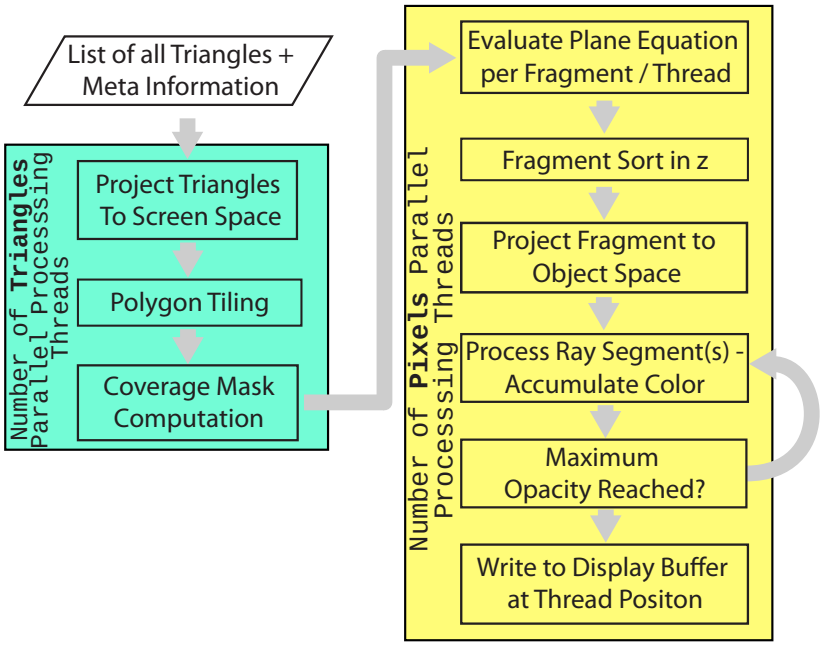

Figure 5.5: The flow-chart shows an overview of our rendering system. The main steps — triangle processing and pixel processing — are executed in separate compute kernels.

5.3.2.1 Triangle rasterization

In conventional rendering of scenes dominated by opaque objects, high performance is related to being able to identify occluded portions of the scene early in the pipeline. In contrast, our volume rendering must unconditionally rasterize all polygons and pass information on the screen coverage of a polygon as quickly as possible to the pixel processing. After transforming a triangle into screen space, for each tile of 8×8 pixels intersecting the

triangle's bounding box, a 64-bit coverage mask [54] is computed. This simple strategy maps well to CUDA hardware due to its low resource requirements and outperforms more sophisticated approaches (such as [137]) for typical scenes.

It is essential for our approach that every fragment covered by the triangulated volume boundary is visited exactly once since we initialize the ray segments for our ray caster at the rasterized surface fragments. Coverage masks are well suited for this purpose due to the simple bit-wise AND operation of the contributions of the corresponding half planes. However, precomputed coverage masks cannot be used in this case since a particular mask is selected from the lookup table based on a discretized orientation of the half plane, which might result in a few misclassified pixels. We therefore compute the covered pixels for each triangle on-the-fly. Since the GPU cores in our target platform (NVIDIA GT200) are scalar processors, the method proposed by [137] is not favorable in our case. Instead, we make use of bit shift operations to compute one row (or column) of the $N \times N$ pixel coverage mask in constant time.

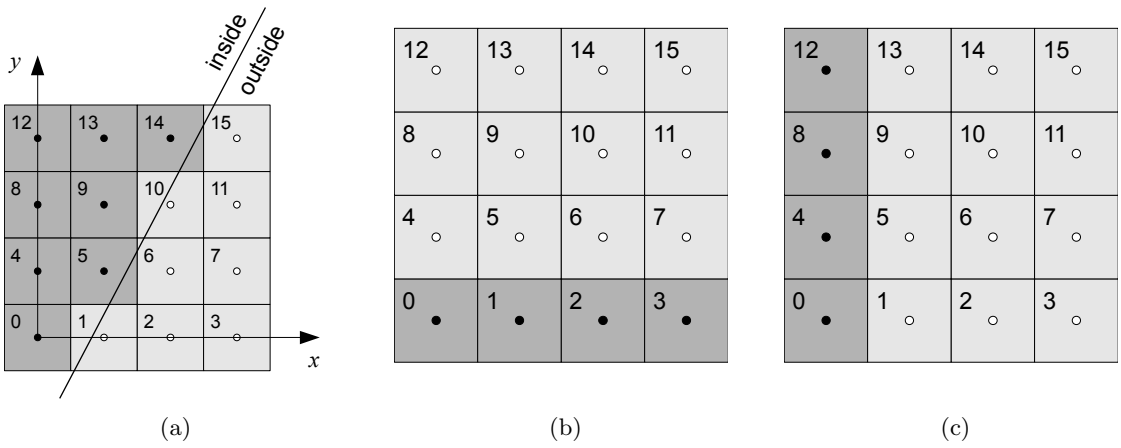

Figure 5.6: On-the-fly half plane inclusion test for a 4×4 pixels square. The coverage mask (a) is composed of shifted copies of the unit row $r_0 =$ 0x000F (b) or the unit column $c_0 =$ 0x1111 (c). The numbers refer to bit positions in the coverage mask.

Consider the example in Figure 5.6a. The outside half plane is defined by $ax+by+c > 0$. A bit in the mask is set to one (dark squares in Figure 5.6a) if the corresponding pixel center (filled circles) is located inside the half plane, and otherwise set to zero. For plane coefficients $a > 0$ and $|a| > |b|$ (such as in this example), we compute the number $n_1(y)$ of

"one" bits in a given row $y \in \mathbb{Z}$, which equals the number of corresponding pixel centers to the left of the line separating the inside and outside half planes:

$$x = -\frac{by + c}{a}, \quad n_1(y) = \text{clamp}(0, \lceil x \rceil, N), \tag{5.2}$$

where $\text{clamp}(i, j, k) = \max(i, \min(j, k))$. The bit mask $r(y)$ of a single row y can be obtained in constant time from the unit row mask r_0 (Figure 5.6b) by means of two bit shift operations:

$$r(y) = (r_0 >> [N - n_1(y)]) << [N \cdot y]), \tag{5.3}$$

where ">>" and "<<" denote the bit shift operation to the right and left, respectively. The entire coverage mask m is then

$$m = \sum_{y=0}^{N-1} r(y). \tag{5.4}$$

For $|a| < |b|$ we proceed in a similar way column-by-column, using the unit column mask c_0 in Figure 5.6c instead. The case $a \leq 0$ is handled by symmetry and bit-wise inversion.

Note that all constants in the equations can be precomputed, such that equation (5.4) can handle both the row-by-row and column-by-column case without conditional expressions to distinguish them. It is therefore possible to process triangles with arbitrary edge orientation in parallel in a SIMD-efficient way. On current NVIDIA hardware, this method is four times faster than a straightforward per-pixel computation of the mask as proposed by [137].

Every triangle record contains the coverage mask and the ID of the contributing triangle. No per-fragment information is stored in global memory, which makes the communication significantly more efficient than conventional buffer strategies [18, 96]. The triangle records are organized in chunks of 64 records each, which are drawn from a preallocated pool of memory. When a tile receives its first triangle (or the previous chunk is fully occupied), a globally unique 32-bit chunk index is appended to the list of chunk indices associated with this tile. We choose a maximum of 64 chunks per tile, which allows for a total number of 4096 triangles per tile. Parallel creation of this data structure is synchronized among the worker threads of the triangle kernel using atomic functions.

5.3.2.2 Depth sorting

A block of threads responsible for a tile consists of 64 threads, one for each pixel in the tile. A thread's first task is to build a representation of the ray, consisting of the intersections with the triangles, sorted by depth. The thread iterates through the list of triangle records and checks its bit in the coverage mask. If the bit is set, it computes the depth of intersection from the triangle's plane equation. The z-values and triangle IDs are stored as array in fast shared memory. We therefore allocate only a single 32-bit value per entry, 16-bit for the signed z-value and 16-bit for the triangle ID. The entries in this array are interleaved to avoid banking conflicts.

Moreover, the available shared memory of almost 16 KB is subdivided into 64 slots, allowing every thread to store a maximum of 63 entries. This limits the maximum depth complexity to 63. The array is maintained in sorted order by inserting new values at the appropriate position, with those entries closest to the camera first (more complex sorting algorithms are likely to perform worse on such a small dataset). It is therefore guaranteed that the array contains the 63 closest fragments, no matter in which order they appear in the input. It turns out that the time spent for sorting is small compared to the subsequent ray traversal time, even for a specially designed worst-case scenario where the entire list of fragments has to be reversed (i.e., has quadratic time complexity in the number of fragments). Moreover, due to the spatial coherence in moderately complex scenes, the insertion operation is likely consistent across many threads. Fragments with rank 64 or higher in the sorted order are discarded. The rationale of this approach is that fragments occluded by 63 closer layers will have minimal influence on the final image, and can therefore be omitted.

To illustrate this claim, we have tested the approximations on objects with very high depth complexity. A ground truth implementation using larger but slower global memory rather than shared memory was used for comparison. The object presented in Figure 5.7, which was chosen for the highest depth complexity from our sample scenes, has a maximum depth complexity of 81 in the present view. Fewer than 0.05% of pixels exceed the threshold of a 5% difference between the fully correct and the approximated image (i.e. 12.75 gray levels of the overall color range 0 – 255). The contrast enhanced difference image in Figure 5.7 confirms this observation.

Allocating 16 bits for a triangle ID limits the number of simultaneously visible triangles to 64k. We have found this to be an acceptable compromise, since the visual complexity in a scene is usually dominated by the volumetric objects. There are two ways to trade off

(a) (b) (c) (d)

Figure 5.7: (a) Thumbscrew (max. depth complexity of 81). (b) Image from our system (depth complexity limited to 55). (c) Reference image with full depth complexity (slower algorithm). (d) Enlarged differences. Fewer than 0.05% of the pixels show errors > 5% of the color range.

other features for a larger number of visible triangles. We can forsake the ability to access a triangle's normal for surface shading (see Section 5.3.2.3). In this case the triangle ID can be replaced by an object ID, and we can still perform all volumetric shading effects and CSG operations. Alternatively, we can limit the maximum depth complexity to 32 layers, and use the additional 32-bit per depth entry for a quantized normal.

5.3.2.3 Ray casting of homogeneous segments

After sorting, a pixel thread iterates through the above-mentioned depth sorted array in order, from nearest to farthest. The depth interval between two consecutive entries in the array defines a homogeneous segment of the ray with respect to intersected objects. While traversing the array, we maintain information on the set of currently intersected scene objects, which are leafs of the CSG tree defining the scene. Figure 5.8 illustrates an example of the CSG operations enabled in this way.

An empty set of scene objects means the segment can be skipped. If one or more scene objects are intersected, the starting point of the ray has to be transformed into the model coordinates of each scene object, thus forming a set of object space rays. Each object space ray has to use the same step size in world coordinates to correctly blend the samples from each scene object. Since scene objects can have different size and resolution, we use the minimum step size of all objects along the ray segment to guarantee that no features are missed. Since this can lead to oversampling of objects with lower resolution, we provide an option to adjust this parameter. Objects which would require a high sampling rate might not provide more information at that rate, so we let the user balance between speed and accuracy. However, oversampling does not significantly influence performance due to texture cache coherence. For blending sampling points of different objects, we query

the transfer functions separately and multiply the resulting colors with their transparency and a sampling factor which accounts for oversampling. The results are summed up and accumulated to the ray. For purely polyhedral objects made from a homogeneous material, no volume texture sampling is necessary. If a ray segment consists only of polyhedral objects, the loop can be avoided while still yielding high quality translucency. This can yield performance improvements of up to 10%. Once a ray segment has been sampled, the intermediate result is blended into the final result color for this pixel. If a certain opacity threshold is exceeded, the ray can be terminated.

Since polyhedral geometry plays an important role, both surface shading of the polygons and volumetric shading from 3D textures are combined. Optionally, conventional surface material parameters can be assigned to every scene object to add Phong shading and surface transparency effects at object boundaries.

(a) (b) (c)

Figure 5.8: CSG operation examples: boolean difference (a), boolean union (b) and boolean intersection (c). Note that visualization of the boundary surface for highlighting cutting region(s) can be toggled by including or not including the boundary in the operation as shown in (a) and (c). In both cases the particular choice results in cutting surface being highlighted.

5.3.2.4 Empty space skipping

Empty space skipping is an essential acceleration technique for volume rendering. In conventional hardware accelerated ray casting, exterior empty space skipping is typically done by calculating bounding geometries [13, 88]. The bounding geometry is rendered with

vertex coordinates encoded as RGB values, so that the graphics hardware computes the ray entry and exit points for accumulation. Interior empty space skipping either requires a multi-pass ray casting approach similar to depth peeling or sampling of an additional lower resolution texture, which encodes empty and full bricks (sub-volumes) of a volume.

The efficient handling of bounding geometry in our rendering system allows exterior and interior space to be skipped in a uniform way. A lower resolution mask volume is calculated decomposing the original volume into uniform bricks, which are masked out if the transfer function evaluates to zero at each underlying dataset voxel. The brick size is user configurable per volume, for medical datasets a size of 8^3 results in maximum performance. The actual bounding geometry polygons enclosing full bricks are obtained using a traversal similar to a marching cubes algorithm [91] of the mask volume, which avoids generation of duplicate polygons. Detection of empty bricks and the subsequent geometry calculation for a particular volume requires evaluation of the transfer function for all voxels in a volume and must be repeated every time the transfer function changes. For interactive transfer function editing, short calculation times are essential. This can easily be achieved by performing the calculation in parallel on the GPU, thereby avoiding additional slow data transfers from system memory. Computation times for a 512^3 dataset are around 5 milliseconds on an NVIDIA 280 GTX.

New bounding geometry polygons are inserted into the global triangle list in global GPU memory and associated with the relevant scene object. During ray traversal using the sorted fragment list, bounding geometry polygons allow for simultaneous exterior and interior space skipping based on a set of active objects, which is updated whenever a bounding geometry fragment is processed, adding or removing a particular object. Note that the set also contains in/outside information from all polygonal objects and is the basis for the evaluation of the CSG-tree. The algorithm may directly skip to the next fragment, whenever the set is empty and/or the CSG expression evaluates correspondingly.

The use of tight fitting bounding geometry improves the frame rate by up to 15%, in particular for transfer functions which make large portions of a volume transparent. In general, the optimization affects both the triangle and the pixel processing kernel, since smaller triangles can be processed more efficiently than large ones in the triangle kernel, and the pixel kernel needs to process fewer ray segments, both in screen space and along the rays.

5.3.2.5 Volume texture atlas

To overcome the limited possibilities concerning reallocation of arrays in global memory, we use a 3D texture atlas for the volumetric datasets. A texture atlas is a single large 3D texture, which is assigned to one texture unit. The maximum size of the texture atlas depends only on the available graphics memory.

Finding an optimal memory layout is an instance of the cuboid packing problem [74]. Since volume data sets often have a square cross section with a power-of-two edge length, we can (without significant waste of memory) reduce the packing problem to a single dimension, where the solution is trivial. The texture atlas memory is organized into slots of a certain size, depending on the application's needs. A volume can occupy one or several contiguous slots. The border voxels of every slot are duplicated to allow the use of unclamped texture coordinates in the innermost loop (this is not related to OpenGL texture borders, which facilitate seamless stitching of separate textures).

5.3.3 Results

We tested our implementation using CUDA 2.0 on a desktop PC (Intel 3.16 GHz Dual Core2-Duo with 3 GB RAM) running 32-bit Windows Vista and 64-bit Linux. We used two alternative GPUs, a GeForce GTX 280 with 1 GB RAM and a Tesla C1060 Computing Processor with 4 GB RAM. The latter is able to work with volumes up to 1024.

5.3.3.1 Performance

For performance evaluation, we compared our framework with two recently published state-of-the-art multi-volume renderers (Roessler et al. 2008; [131], Brecheisen et al. 2008 [28]), which were kindly provided by the authors. In the following, we refer to these tools as Roessler and Brecheisen, and Ours for our own work. The comparison was done on the GTX 280.

C1 represents a high quality medical scan. C2 and C3 are medical scenes with multiple volumes, which use multiple modalities or scans from different body parts. Figure 5.9 shows C2 as the image on the left. C4 and C5 show an anatomical scan involving a time resolved scan, for example of blood flow, leading to a larger number of volumes. C6 is a combination of an anatomical scan with a high resolution iso-surface. C7 is a volume of the abdomen combined with different polygon models shown as the right-hand image in Figure 5.9.

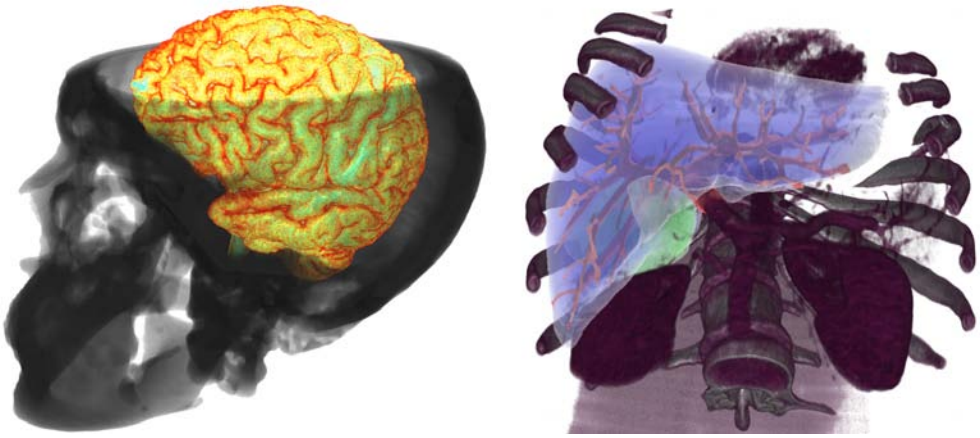

Figure 5.9: Most relevant scenes for real medical applications are used as test cases C2 (left) and C7 (right). C2 shows a skull acquired as CT scan with a brain acquired as MRI. C7 is a volume of the abdomen, combined with a 10k polygonal model representing the liver surface, a 30k polygon model representing the liver portal vessel tree and a 5k polygon model representing a tumor.

No	Volumes	Polygons	Roessler	Brecheisen	Ours
C1	1×512^3	none	14 – 46	9 – 17	10 – 21
C2	2×256^3	none	24 – 38	6 – 12	17 – 25
C3	4×256^3	none	5 – 9	1 – 3	16 – 25
C4	1×256^3 7×128^3	none	1.5 – 3	n.p.	15 – 23
C5	1×256^3, 20×64^3	none	n.p.	n.p.	10 – 17
C6	1×512^3	1×30k	n.p.	1 – 2	7 – 15
C7	1×512^3	1×10k 1×30k 1×5k	n.p.	0 – 1	7 – 15
C8	50×64^3	1×30k	n.p.	n.p.	8 – 16

Table 5.1: Overview of test scenes used for performance comparison with state-of-the-art tools.

Table 5.1 compares the frame rates achieved with Roessler and Brecheisen and our approach. Roessler generates shader code for every scene and is therefore quite efficient for a few volumes. However, it cannot handle geometry and therefore cannot be used for cases C6 through C8. It could also not run C5 on our system since the generated shader code was too large. Brecheisen is able to handle up to four volumes combined with an arbitrary number of intersecting geometric objects, and therefore cannot handle C4, C5 or

C8. In our experiments, we varied viewport size (between 512 and 768), transfer functions and camera positions. Reported minimum and maximum frame rates are averaged over the tested viewport sizes, since the tools used for comparison do not allow arbitrary choices of viewport size. Lighting is done with pre-calculated gradients, since Roessler only provides this method. Progressive rendering is disabled in all evaluated tools. The tests are performed with 8-bit value per sample datasets due to the restrictions of Roessler and Brecheisen. A transfer function with high transparency is chosen to avoid early ray termination. Camera zoom is set to a value such that most screen pixels are covered. Table 5.1 indicates that our approach compares favorable with shader based systems in particular for scenes with many volumes or complex geometry.

5.3.3.2 Workload distribution

In order to understand our rendering system better, an analysis of the workload for various conditions was undertaken. The triangle kernel uses only 2–10% of the computation time, depending on the triangle/voxel ratio of the scene. The NVIDIA Visual Profiler revealed that the triangle kernel is able to efficiently occupy all processors of the GPU, thus optimally hiding global memory latency. Moreover, projecting triangles and computing coverage masks are very uniform tasks with few diverging branches, which allows peak rates to be obtained. Overall, the pixel kernel uses up to 90% of the computation time. Since kernels are executed in threads on the GPU asynchronously with respect to the CPU, the GPU code was instrumented using the *clock()* API function to query the number of GPU cycles. Unfortunately, this function does not report the time spent per thread, but rather the clock of the processor, while the processor performs time slicing of multiple threads. Low consumption of register space and shared memory allows more threads to be active (i.e., time-sliced) concurrently and therefore better hiding of memory latency. This improves performance, but at the same time makes clock measurements unreliable.

We therefore experimented with both low and heavy loads on shared memory. A low load can be achieved by limiting the maximum complexity of the scene. For example, lowering the maximum depth complexity or the number of intersecting objects frees register space and shared memory per execution block, and therefore enables the GPU scheduler to run other blocks while waiting for memory transfers. Through this strategy, we could obtain overall performance improvements of up to 40%. We also selected setups which create a heavy load on shared memory, giving no opportunity for time slicing. This allowed us to perform the following analysis. For scenes with significant geometry, but relatively little

volume data, the results indicated that up to 50% of the pixel kernel's work consists of sorting fragments in z-direction. The rest consists of Phong shading of geometry surfaces ($< 3\%$), accumulating pure geometry interiors ($< 3\%$) and ray traversal of volumetric data (23%). Tests with various scenes confirmed that ray traversal is generally the most costly part. This is reassuring because it seems likely that the $O(n^3)$ complexity for handling the volumetric data should dominate the system's performance. However, it also means there is limited room left for improvements.

5.3.3.3 Memory consumption

The memory requirements of the described method are mainly related to the texture atlas and the triangle records used to communicate between triangle kernel and pixel kernel. The texture atlas size depends on cumulated sizes of the volumes contained in the scene. We commonly use a texture atlas of 528^3, which can accommodate all the scenes used in the evaluation, in about 562 MB of global memory. Pre-calculation of gradients for lighting increases the required memory by a factor of four, because for every sample three additional values need to be stored.

The triangle record memory consumption for a viewport size of 768^2 pixels is 96^2 (tiles) $\times$ 64 (chunks per tile) $\times$ 4 (bytes per index) = 2.25 MB for the fixed-size set of chunk indices, plus the variable-sized chunk pool (768 bytes per chunk). Our experiments were run with a total chunk pool size of 6 MB, which can be raised for more complex scenes up to the limit imposed by the available amount of memory on the graphics card.

Due to recent improvements in multicore GPU programming models, we were able to develop a new approach for multi-volume and geometry rendering. CUDA is not specifically designed for graphics, but allows the development of a software rendering pipeline, which is executed in a massively parallel way. A key property of this approach is the efficient use of scatter operations, which allows a scene's polygons to be rasterized only once.

Our created raycaster builds a strong backbone that allows presenting all data acquired in the medical procedure of RFA together with simulated data. We apply it to visualize the results of the following examinations. Further development of the presented raycaster as well as suitable visualization techniques are left as future work outside of the scope of this thesis.

Chapter 6

Modeling radiofrequency ablation

Contents

A correct description of the RFA process is not only mathematically demanding, but also relies on model equations for the medical and biochemical process. Descriptions from an engineering perspective explain many details but are rarely integrated into one all encompassing model. Most importantly, treatment models do not fit treatment results. Some phenomena are not incorporated and also for some phenomena their importance in the role of treatment planning is not resolved as yet.

We describe the details of the RFA process from an engineering perspective. Modeling this very complex process holds many challenges. With the aim of validating a computational prediction model we put a special emphasis on existing models as well as necessary model accuracy. An all encompassing equation is far removed from the current state of the art and will not be easily achieved. The following sections give an overview over the complexity of the process and an approach to deal with the major effects in a computer model.

6.1 Radiofrequency ablation from a biological and chemical perspective

The process of RFA begins with placing a needle inside a tumor. Most important is here to hit the target exactly as planned. When switched on, the RF generator creates an electromagnetic field. The needle electrode thereby plays the role of an antenna sending electromagnetic waves into the tissue. As in any electromagnetic field, the energy density decreases with the distance from the needle. Ions are electrically charged atoms or molecules and part of tissues and fluids. They move with the induced alternating electromagnetic field, causing friction along the path they take. This friction generates heat in the target region. Understanding this mechanism leads to two important findings with direct consequences for the procedure and its result. First, the heat is generated in the tissue. It flows from the tissue to the needle and not vice versa. Measuring the needle temperature directly only gives hints at tissue temperature. Heating the needle in a different media leads to incomparable results that do not allow us to draw conclusions on heating within the tissue. Second, hot spots in the tissue exist and depend on the tissue parameters. Obviously, those regions in the tissue that react the strongest to the ion friction are heated the most, not those closest to the needle. The herein described effects are modeled in physical equations and influence the procedure and result in the organ on a 'whole liver' macroscopic scale.

6.1.1 Heat propagation in the tissue

The heat created is conducted to the surrounding tissue. The most dominant effect here is cooling by perfusion. Blood in nearby vessels with a diameter above 3 mm is heated up, but then a quantity of heat is carried away with the blood flow. It is replaced by new, cooler blood. This effect has often been observed in medical studies and determines size and shape of the coagulation visibly. The main governing equation is the Bioheat equation [123]. This mathematical description allows us to compute the heat transfer in biological tissues.

In addition, cooling in the form of micro-perfusion also influences the size of the necrosis zone. Even at a distance from large blood vessels, RFA applied with the same outer parameters creates smaller coagulations in perfused tissue than in unperfused tissue [114].

6.1.2 Biological and chemical reactions

When the tissue is heated up the cell fluid starts to boil. One effect is that micro-bubbles are created. They are visible in ultrasound images during the procedure and are mainly responsible for the low benefit of intra-operational ultrasound. Furthermore, the tissue coagulates and if heated up too high or too fast it carbonizes.

Cell chemistry changes during the heating process. From a biochemical point of view, tissue coagulation occurs as the cell proteins denature. So by applying energy in the form of heat, the protein molecules' structures in space change. The chemical reactions of enzymes are hindered or impeded completely. Biological structures in the cell are destroyed. The most visible effect (under the microscope) is the destruction of the cell's nucleus. Furthermore the mitochondria (responsible for the cell's energy metabolism) are destroyed. Finally, the cell enters a metabolic cycle that leads to its death in the near future. Changes in cell metabolism are responsible for ongoing cell death even after switching off the RF generator and removing the needle. The final necrosis changes size and shape for a couple of days after the intervention [105].

Measurements of heat distribution can be acquired using intera-operative MRI scans and compared to histological findings to gain validation hints. As the models are based on phenomenological observations further research to understand cell changes and theoretical model mechanisms on the cell level is still needed.

6.1.3 Material parameters

The effects of boiling cell fluid and coagulating tissue not only remove energy (i.e. heat) from the process serving as a tiny heat sink, but they also have a direct influence on the tissues material parameters: the local efficiency of radiation conduction, heat conduction, and ion friction change with the tissue heat. The respective physical equations therefore do not rely on constants for the material properties but on parameters that couple the result back to the source. Measuring these values is a question for physiological measurements or biomedical engineering.

6.2 Induced physical effects in the process

In addition to all the medical and biochemical processes that need to be modeled, the RFA procedure is induced by applying external factors. So a needle electrode is used to deliver external energy to the tissue in the form of electromagnetic waves. Where the radiation

energy is deposited in the tissue depends on the geometry of the electrode as well as on the emitted radiation frequency.

6.2.1 Needle geometry

Ablation electrodes as used today in clinical practice are rarely simple mono-polar or bipolar electrodes but rather extendable umbrella shaped electrode arrays, as for example the RITA StarBurst (see Figure 6.1). In homogeneous media those shapes produce large coagulations of up to 7 cm. These electrode arrays are therefore better suited to treat tumors of relevant size (up to 5 cm).

Figure 6.1: RITA Starburst XL: Expandable umbrella shaped needle electrode as marketed by AngioDynamics

According to the manufacturer the RITA needle forms a sheprically shaped coagulation. In a study by Lobik et al. [90] coagulated egg white takes on a mushroom or cone shape. The shapes predicted by the manufacturer are not achieved.

6.2.2 Ablation protocol

The control algorithm is built into the radiofrequency generator. Therefore, it is set by the manufacturer and can rarely be changed, simulations which examine these algorithms can only deal with coarse adjustments. For example, looking at runtime for the ablation in the final extension state could be useful for treating patients with more certainty.

For a model predicting RFA, these external effects have to be modeled in the equations together with the medical and biochemical processes. For a validation study, we modeled the exact conditions as used in the validation experiment. In our validation study we used the RITA RF system by AngioDynamics. We created a prediction for the RITA system, encompassing all major effects and therefore usable for treatment planning.

6.3 Mathematically modeling the complete RFA process

From the many different existing models for the RFA process Kroeger's model has been compared to patient images — though the patient data used was acquired 2 months after the intervention. The publication by Kroeger et al. [80] at least attempts a validation of the computation model. The solver described computes the finite element in 3D for a multi-physics system. Starting from this model we developed an extended version to deal with the RITA system necessities.

6.3.1 Kroeger's model

Major parts of Kroeger's model for the RFA process are

- tissue-state dependent physical properties
- calculation of electromagnetic potential that allows us to model of both monopolar and bipolar probes
- calculation of temperature distribution using the bioheat equation calculations of tissue water evaporation and condensation.

All of these parts are very interdependent. In order to solve such a tightly coupled system of PDEs, Kroeger et. al. proposed using a fixed-point iteration algorithm.

Equations that allow modeling of the heat transfer induced by radiation, the cooling effect caused by blood vessels, as well as heat conduction in the tissue, are in nature coupled partial differential equations in three dimensions and cannot be solved analytically. Figure 6.2 shows the interdependencies between the equations in Kroeger's model.

Every block in the diagram represents equations that model the specific aspect of the complete system.

6.3.2 The modified model

We cannot apply Kroeger's model directly to the RITA system as it has several limitations. Firstly, the proposed model of evaporation does not allow the temperature of the tissue to exceed 100°C. As for the commonly used ablation protocols that are used with the RITA generator, the average target temperature of readings on the needle tips is 105°C, overcoming this limitation is of great importance. Secondly, as RITA performs

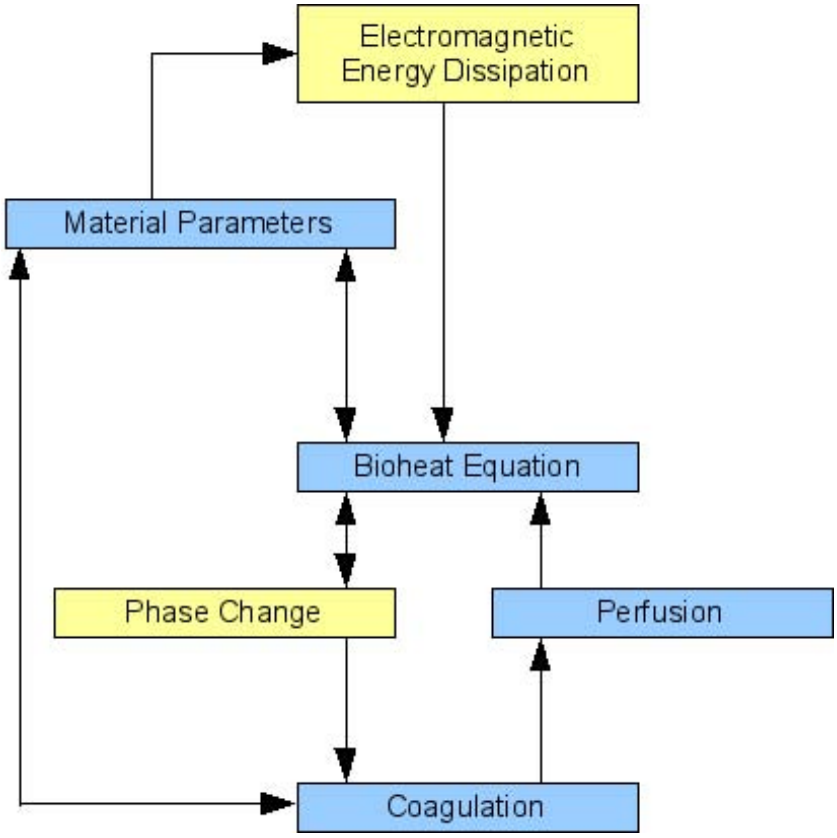

Figure 6.2: Equations used to model the RFA process according to Kroeger are strongly interdependent. Every building block in this diagram models a process described by partial differential equations. The arrows show the influence of changes in one term which lead to recomputation of the state in another term. Blocks shown in yellow have been substituted in the process of adapting the model to the RITA ablation device.

temperature-controlled ablations, the mechanisms for the calculation of the power deposited in the tissue should be changed. In the following sections we describe the model equations.

6.3.2.1 The Bioheat Equation

The electrical currents heat the tissue up due to Joule heating. This process can be modeled with the following equation:

$$\frac{\partial\left(\rho c' T\right)}{\partial t} = \nabla\left(\lambda \nabla T\right) + Q \tag{6.1}$$

where ρ is the density $\left[\mathrm{kg/m^3}\right]$, λ is the thermal conductivity $\left[\mathrm{W/\left(m \cdot K\right)}\right]$ and c' is

the effective specific heat capacity [J/kg · K].

with

$$Q\left(t,x\right)=Q_{\mathrm{rf}}\left(t,x\right)+Q_{\mathrm{perf}}\left(t,x\right)+Q_{\mathrm{m}}\left(t,x\right) \tag{6.2}$$

where Q_{rf} is the heat induced by the radiofrequency ablation (dissipation of electromagnetic energy), Q_{perf} models the cooling due to perfusion, and Q_{m} is heat generated by metabolism. The latter term is considered insignificantly small compared to the first two and therefore it is excluded from modeling.

The effective specific heat capacity $c\prime$ is used to seamlessly integrate the energy that is necessary for tissue water evaporation to the bioheat Equation 6.2. Following Yang et al. [165] we set this term to

$$c\prime=c-\frac{\alpha}{\rho}\cdot\frac{\partial\rho_{W}}{\partial T} \tag{6.3}$$

where α is the specific latent heat of water vaporization [kJ/kg] and ρ_{W} is the density of water in tissue [kg/m^3]. The functional form of the dependence of tissue water density on the temperature is derived in [165] to match the experimental measurements. Furthermore, the evaporated water is considered not to escape the system but to condense in the other parts of the tissue. We model this process by

$$\frac{\partial\left(\rho cT\right)}{\partial t}=\alpha\cdot m_{\mathrm{V}}\frac{f_{\mathrm{c}}}{F_{\mathrm{c}}} \tag{6.4}$$

where m_{V} is the total mass of water [kg] that evaporates within the tissue and $\frac{f_{\mathrm{c}}}{F_{\mathrm{c}}}$ is the fraction of water that condenses at a particular point in space. To compute this fraction we first define the function $f_{\mathrm{c}}(T)$ that controls the distribution of water vapor within the tissue. The normalizing coefficient F_{c} is then computed as the integral of f_{c} over the whole space. Following Yang et al. [165] we assume that the vapor is deposited in the range between 60°C and 80°C. The shape of the continuous function $f_{\mathrm{c}}(T)$ that is used in this study is shown in Figure 6.3.

6.3.2.2 Joule heat

The distribution of the electromagnetic potential within the tissue influences the term Q_{rf}, the heat sink due to perfusion. We assume that this distribution is quasistatic and is governed by Laplace's equation.

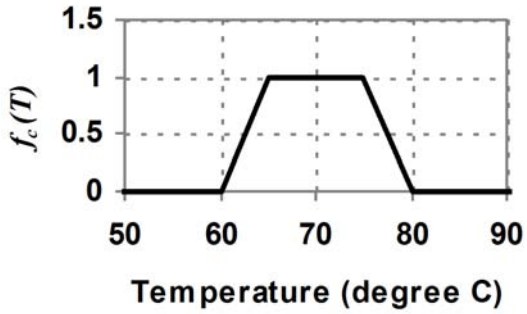

Figure 6.3: The assumed shape of the continuous function that controls the distribution of water vapor within the tissue (based on an assumption made in [165]). The fraction of vapor that is deposited within a certain temperature range is proportional to the integral of this function.

$$-\nabla \cdot (\sigma \nabla \phi) = 0 \tag{6.5}$$

where σ denotes the electrical conductivity $[\mathrm{A}/(\mathrm{V} \cdot \mathrm{m})]$ and ϕ is the electric potential. The power applied at every point in space can then be calculated as

$$p(t,x) = \sigma(t,x) \left|\nabla \phi(t,x)\right|^2 \tag{6.6}$$

This power value is then scaled so that the total power deposited in the tissue matches the desired setup power of the generator:

$$Q_{\mathrm{rf}}(t,x) = p(t,x) \frac{p_{\mathrm{setup}}(t)}{p_{\mathrm{total}}(t)} \tag{6.7}$$

where p_{total} is the integral of $p(t,x)$ over the whole space. The setup power of the generator is calculated using the proportional- integral controller [69].

6.3.2.3 Coagulation and perfusion

The tissue coagulation is modeled by the Arrhenius formalism:

$$C = 1 - e^{-\Omega}, \qquad \partial_t \Omega = A_A e^{-E_A \frac{1}{RT}}, \qquad \Omega(t_0) \tag{6.8}$$

where R is the universal gas constant $[\mathrm{J}/\mathrm{K} \cdot \mathrm{mol}]$, $A_A = 9,4 \cdot 10^{104} \mathrm{s}^{-1}$ and $E_{\mathrm{A}} = 6,7 \cdot 10^5 \frac{\mathrm{J}}{\mathrm{mol}}$.

The amount of energy taken away by blood is calculated by using the extension of

Parameter	ψ_1	ψ_2	ψ_3	ψ_4
σ	0.21 $\mathrm{A}/(\mathrm{V}\cdot\mathrm{m})$	0.013 K^{-1}	-1	1.143
ρ	1080 $\mathrm{kg/m}^3$	-0.00056 K^{-1}	-0.657	0
c	3455 $\mathrm{J}/(\mathrm{kg}\cdot\mathrm{K})$	0	-0.596	0
λ	0.437 $\mathrm{W}/(\mathrm{K}\cdot\mathrm{m})$	0.0025 K^{-1}	0	0

Table 6.1: Material constants for tissue-state dependent parameters

Pennes' approach:

$$Q_{\mathrm{perf}}(t,x) = \nu(x,\mathrm{DS})\,\rho_{\mathrm{b}} c_{\mathrm{b}}\,(T_{\mathrm{body}} - T(t,x)) \tag{6.9}$$

where ρ_{b} is the blood density $\left[\mathrm{kg/m}^3\right]$ and c_{b} is the specific heat capacity of blood $[\mathrm{J/kg}\cdot\mathrm{K}]$. $\nu(x,\mathrm{DS})$ is the perfusion coefficient $\left[\mathrm{s}^{-1}\right]$. We set its value to 0.05 s^{-1} inside the hepatic and portal veins and $0.1\mathrm{s}^{-1}$ inside the artery [80].

Inside the rest part of the tissue we use the approximation proposed in [135] that models the dependence of perfusion on the degree of vascular stasis. DS is the degree of vascular stasis which is computed by using the Arrhenius formalism similar to 6.8, but with slightly different parameters: in this case $A_{\mathrm{A}} = 1.98\cdot 10^{106}\mathrm{s}^{-1}$ and $E_{\mathrm{A}} = 6.67\cdot 10^5\mathrm{J/mol}$ [135].

6.3.2.4 Material parameters

Kroeger's model uses the approximation of the dependence of the physical properties of liver tissue (i.e. electrical and thermal conductivities, as well as tissue density and specific heat capacity) on tissue temperature, relative amount of water within the tissue, and its state of coagulation as in [80]

$$\psi(t,x) = \psi_1\cdot(1+\psi_2\,(T(t,x) - T_{\mathrm{body}}))\cdot(1+\psi_3\,(1-W_{\mathrm{R}}(t,x)))\,(1+\psi_4\cdot C(t,x)) \tag{6.10}$$

where ψ stands for either one of σ, ρ, c, or λ with the respective constant values that are listed in 6.1. W_R is relative content of fluid water which in our model is calculated as

$$W_{\mathrm{R}} = \frac{\rho_{\mathrm{W}}(T)}{\rho_{\mathrm{W}}(T)+\rho_{\mathrm{L}}}\cdot\frac{\rho_1}{\rho_{\mathrm{W}}(T_{\mathrm{body}})}, \qquad \rho_{\mathrm{L}} = \rho_1 - \rho_{\mathrm{W}}(T_{\mathrm{body}}) \tag{6.11}$$

where ρ_{L} is the density of dry liver tissue $[\mathrm{kg/m}^3]$.

6.3.3 Numeric Simulation

Similar to Kroeger [80] we solved this heavily connected system of equations as a fixpoint iteration on changing state variable values. Whenever one new state is computed in one of the parts the dependent parts were recomputed with the new state variables as input. In this way the multi-physics system is solvable by working on one physics description at a time.

6.3.3.1 Software and model geometry

We used the deal.II library [15] as a basis for our solver. deal.II is a C++ program library that is a powerful instrument in developing FEM solvers and is easily extensible because it is open-source software in the sense advocated by the Open Source Initiative.

We chose the computational domain to be a cube with a side of 8 cm. The RITA StarBurst XL needle model was placed perpendicularly to one of the faces so that the tip (before expansion of the prongs) was 2.5 cm deep in the cube. With the TrueGrid [148] mesh generator we created a three-dimensional mesh for this geometry with approximately $350,000$ hexahedral elements and with node spacing in the range of 0.2 (in proximity of the needle) to 2 (at the periphery) millimeters. Figure 6.4 shows the mesh for the RITA needle geometry.

As the open source library deal.II demands hexahedral meshes creating the mesh for this non-straight needle geometry presents itself as a difficult challenge. The mesh presented was therefore used in all computations for all needle extensions. Solely, the inserted needle was left to shorter extensions for simulating the non-extended prongs. For this configuration every simulation run stets approximately six hours on a desktop computer with Intel Core i7-960 processor and 4 GB RAM.

6.3.3.2 Initial values and boundary conditions

For the computation of the electric potential distribution 6.6 we set the value of electric potential to 1 on the surface of electrically conducting parts of probe and on the outer surface of computational domain to

$$n \cdot \nabla\phi = n \cdot (s - x) \left| s - x \right|^2 \phi \tag{6.12}$$

where s is the barycenter of the whole electrically conducting surface [80].

For the bioheat equation 6.2 we set the initial temperature in the volume to 37°C

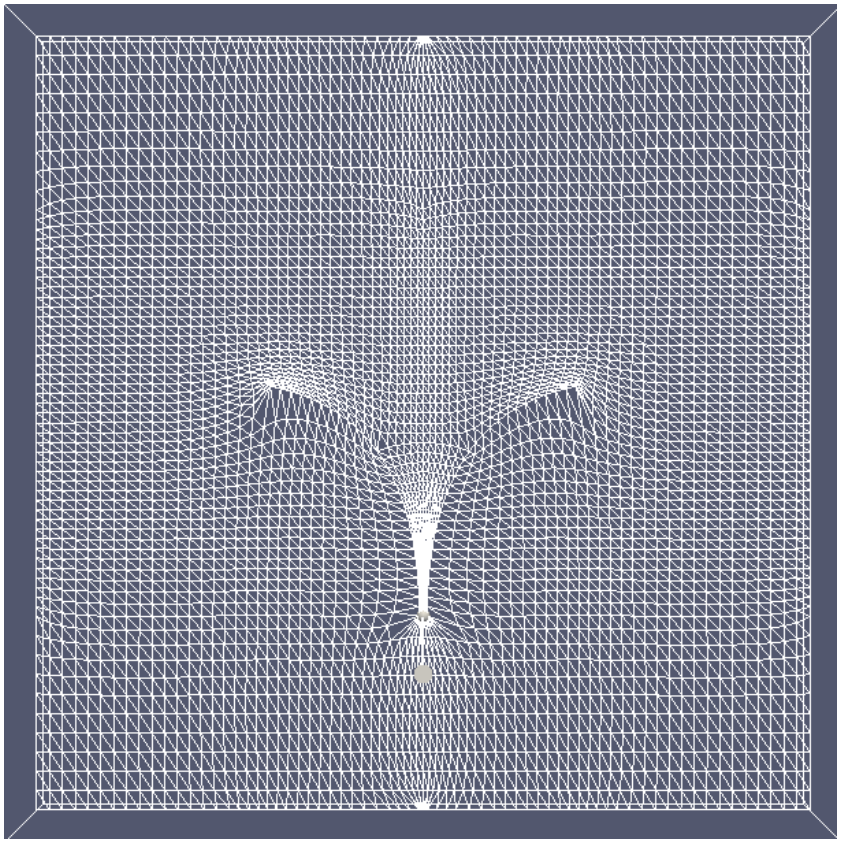

Figure 6.4: One slide of the mesh for the RITA needle geometry. The mesh is in fact a hexahedral mesh. It is presented with connections along the diagonal of the hexahedral elements, as the visualization tool implicitly assumes triangular or tetrahedral meshes.

and homogenous Neumann boundary conditions on the outer surface of computational domain.

Equation 6.4 was solved separately for each time step. The distribution of temperatures at current time served as an initial condition. The homogenous Neumann boundary condition was prescribed on the outer surface of computational domain.

6.4 Simulating RFA to examine tolerance to needle placement deficiencies

Using our prediction model we simulated the influence of needle placement deficiencies on the intervention success. The optimum needle position for tumors of size 1 cm or 2 cm was aimed towards the center of the tumor, with the needle tip at a distance of 1 cm from

Tissue type	Tissue perfusion rate (mL/min/100 mL)	Tumor Type	Tumor perfusion rate (mL/min/100 mL)
CL	67	HCC	94
NL	108	MH	305
NL	108	ML	26

Table 6.2: Perfusion rates for normal (NL) and cirrhotic (CL) liver tissue are taken from [20], for hypoperfused (ML) and hyperperfused (MH) metastasis from [102] and for hepatocellular carcinoma (HCC) from [149].

the tumor center as described in the RITA ablation protocol [6]

6.4.1 Different tumor perfusion rates

In this study we assumed, that there were no large blood vessels in the area where the ablation is performed. We calculated simulations for different needle positions for all three settings of perfusion rates: cirrhotic liver with hepatocellular carcinoma (CL, HCC), normal liver with hyperperfused metastasis (NL, MH), and normal liver with hypoperfused metastasis(NL, ML). Perfusion rates for these settings are presented in Table 6.2. The perfusion rates for liver tissue are taken from [20], for metastasis from [102], and for hepatocellular carcinoma (HCC) from [149].

6.4.2 Influence of a 2 cm tumor

We applied the standard RITA protocol for expandable needles like the Starburst XL for a 4 cm lesion. The ablation protocol for the 4 cm lesion is defined as follows [6] deploy prongs to the 2 cm mark, wait until the average temperature reaches 105°C, deploy to the 3 cm mark, wait until temperature reaches 105°C, deploy to the 4 cm mark, wait until temperature reaches 105°C and then hold at this temperature for 7 minutes. For this protocol the simulation time ranges from 12 to 13.5 minutes, where every simulation run took approximately 6 hours.

Figure 6.5 shows the resulting temperature field achieved with perfect needle positioning for all three settings. We assumed the ablation zone to be the zone where the coagulation value exceeds 99% (curved line), this means the probability of a cell coagulating is at 99%. Due to meshing artifacts the curved line does not appear smooth.

Table 6.3 shows the measurements of the ablated zone dimensions and the shortest distance from the tumor to the non-ablated region.

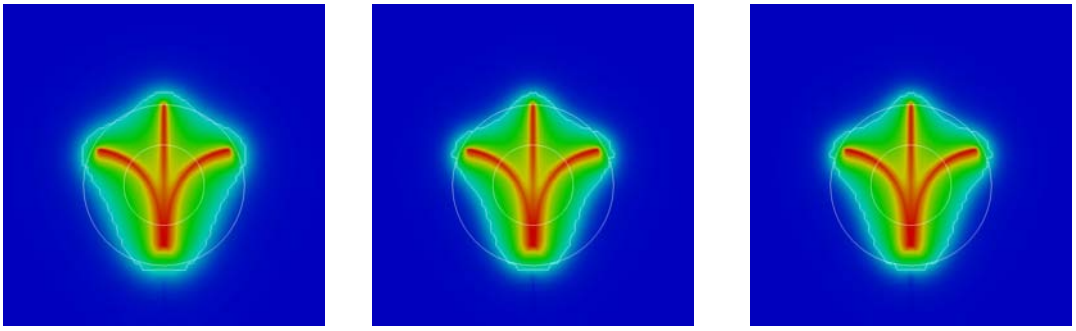

(a) CL, HCC (b) NL, MH (c) NL, ML

Figure 6.5: Resulting temperature fields for needle placement in the optimum position for a tumor with a2-cm diameter.

Tissue/tumor type	Maximal transverse diameter (mm)	Axial diameter (mm)	Shortest distance from tumor to non-ablated region (mm)
CL, HCC	44.5	40.5	5.3
NL, MH	44.4	40.6	3.4
NL, ML	44.3	40.3	3.9

Table 6.3: Ablation zone size for perfect needle placement.

We see that with perfect needle positioning relatively to the tumor the perfusion rate of the tumor does not play a significant role. The maximal sizes of the ablated zone are almost independent of the tumor perfusion rate. This can be explained by the fact that during the first two steps of the ablation protocol the tumor is heated up to the temperatures that are enough to reach a high degree of vascular stasis and therefore the perfusion rate is reduced significantly for the rest of the ablation time. This effect can be seen in Figure 6.6, which shows the temperature field before extending the prongs to the next level. We see that hyperperfused tumors do not lead to significant shrinking of the ablation zone extension and hypoperfused tumors do not lead to much bigger ablation zones.

We see that the hyperperfused metastasis hinders the heating up process in the first needle extension. However, right before extending the prongs for the second time the difficulties are overcome. The heated up area shows almost no difference to the cases with low perfused metastasis or HCC.

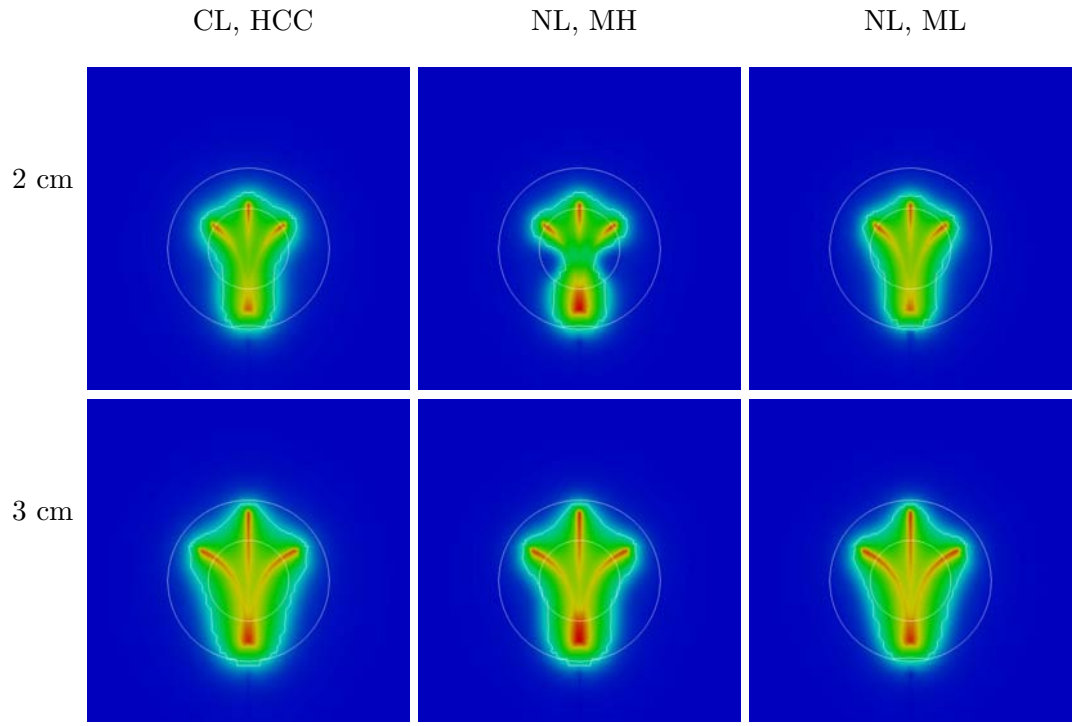

Figure 6.6: Temperature fields and the zones of 99% degree of vascular stasis (curved line interior) for perfect needle placement befor extension of the prongs.

6.4.3 Misplacement of the needle by 5 mm

A typical non-optimum placement occurs when the needle electrode is placed at a distance of 5 mm from the optimum position. This might happen with the needle being too far away, too close, or not leading to the center of the tumor but rather off to one side.

Again, we simulate the temperature field at the end of the ablation — now with the needle misplaced in respect to the tumor. Again, the curved line shows the area of 99% coagulation and lacks smoothness due to meshing artifacts. Figure 6.7 shows the results for all three settings.

While placing the needle at a distance to the tumor which is 5 mm too far away does not show severe effects, being 5 mm too close leads to possible undertreatment. The heated up area at the lower end of the needle is too small to cover the whole tumor and its safety margin, This does not change over time with extending the prongs. So parts of the tumor hit the threshold where 99% coagulation is achieved and possibly tumor cells might survive. The effect occurs for both types of metastasis residing in normally perfused liver tissue. So it is generated by the normal liver perfusion and does not occur for the

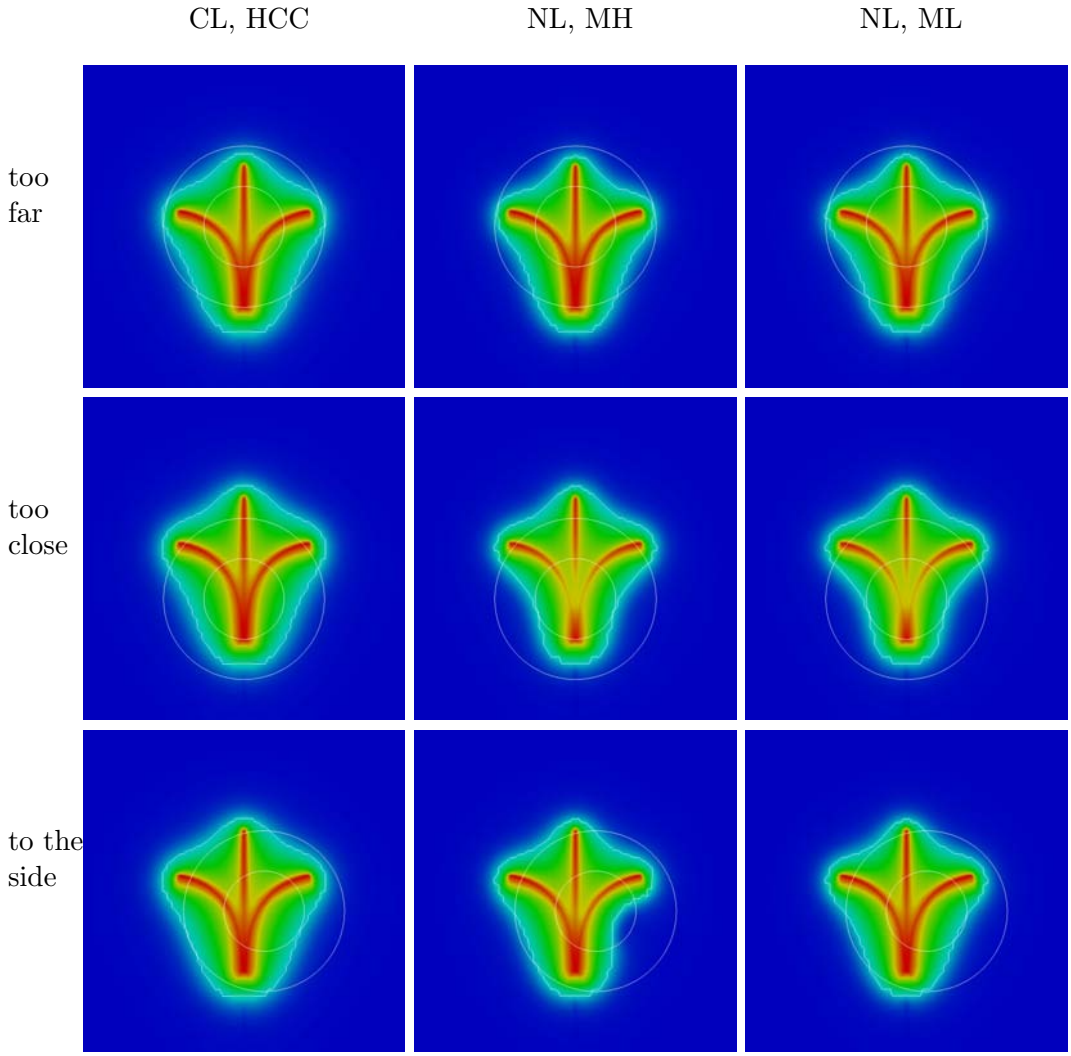

Figure 6.7: Simulation results for needles misplaced by 5 mm.

less perfused cirrhotic tissue. Hitting the surface of the coagulated area with the tumor surface does not leave any safety margin. So this might lead to difficulties for successful treatment.

Even worse results occur for a hyperperfused tumor with the needle tip offset by 5 mm to the side. The simulation shows clearly a suviving tumor part for a hyperperfused tumor in a normally perfused liver. A deviation from optimum needle position of only 0.5 cm already leads to an unsuccessful treatment, if the current mathematical model is correct. This deviation from optimum placement is not unusual in clinical practice. For a hypoperfused metastasis as well as for HCC the tumor surface hits the surface of

Tumor type Needle positioning	CL, HCC	NL, MH	NL, ML
too far	5.4 mm	4.3 mm	3.9 mm
too close	3.4 mm	0.0 mm	0.6 mm
to the side	0.1 mm	−5.0 mm	0.0 mm

Table 6.4: Distance from tumor surface to the area outside the predicted limit for 99% coagulation.

the coagulated region. This situation equals the situation for too close needle placement. Again no safety margin exists.

Measuring the distance from the tumor surface to the region with 99% coagulation we get a numerical evaluation for the situations, which of course still rely on the quality of the mathematical model — just like the overall simulation result.

The result for the case where the needle tip is misplaced to the side shows the most severe difficulty. While bringing the needle too close to the tumor or staying too far away from the tumor can be easily corrected by the placing radiologist (draw back or push forward), missing the center and going to the side is not easily corrected. Here needle placement needs to start from scratch to hit the center more directly.

Figure 6.8 shows the surface comparison for a too close needle placement as well as a needle placement to the side with an offset of 5 mm. The white sphere represents the tumor and the blue surface shows the limit of tissue that is 99% coagulated.

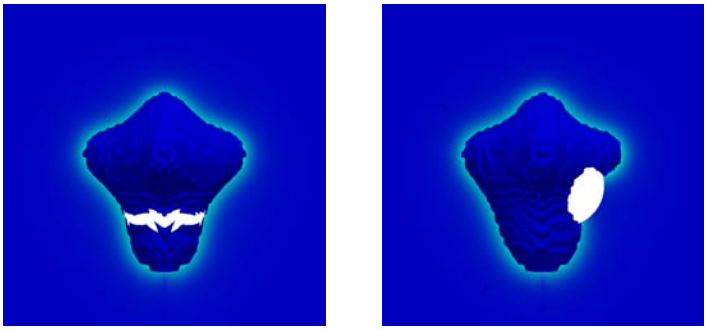

(a) too close (b) to the side

Figure 6.8: Visualization of surfaces for coagulated volume (blue), and treated tumor (white). A tumor which is sticking out lacks treatment. The surface of the coagulated region lacks smoothness due to meshing artifacts.(a) shows the situation for aproaching the tumor too closely, (b) for reaching the optimum position with a deviation to the side.

For the case of severe undertreatment (needle placement off to the side, normal liver

needle placement offset	2 mm	3 mm	4 mm
distance (mm)	1.4	−1.3	−3.4

Table 6.5: Distance from tumor surface (mm) to the area outside the predicted limit for 99% coagulation for different offsets in needle misplacement to the side.

tissue with hyperperfused metastasis) we took a look at the temperature field before the extension of the prongs. Figure 6.9 shows this situation for the timesteps right before the extension of the prongs.

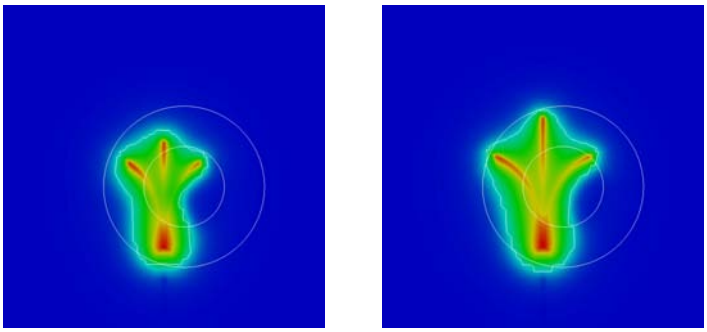

(a) 2 cm extension (b) 3 cm extension

Figure 6.9: Temperature field before extension of the prongs to 2 cm and 3 cm respectively for normal liver tissue with a hyperperfused metastasis.

We can see that the tumor is not completely heated up. Therefore, part of the tumor stayed at a low temperature during the complete treatment. Vascular stasis cannot be achieved for this part and it contributes to the cooling during the complete procedure. The hyperperfused metastasis itself remains to a large part untreated, not to mention the safety margin, even without a heat sink effect from large blood vessels.

6.4.4 Looking closer at deviations to the side

We examine tolerable deviations from the optimum position to the side closer for a 2 cm diameter hyperperfused metastasis. Figure 6.10 shows the effects for 2 mm, 3 mm, and 4 mm offsets, Table 6.5 lists the numeric values for these observations.

While a deviation from the optimum needle position by only 2 mm does not show undertreatment, a deviation by 3 mm causes the tumor overlap the coagulation area and a 4-mm deviation shows this even more clearly. All these observations of course assume that the simulation model used is correct.

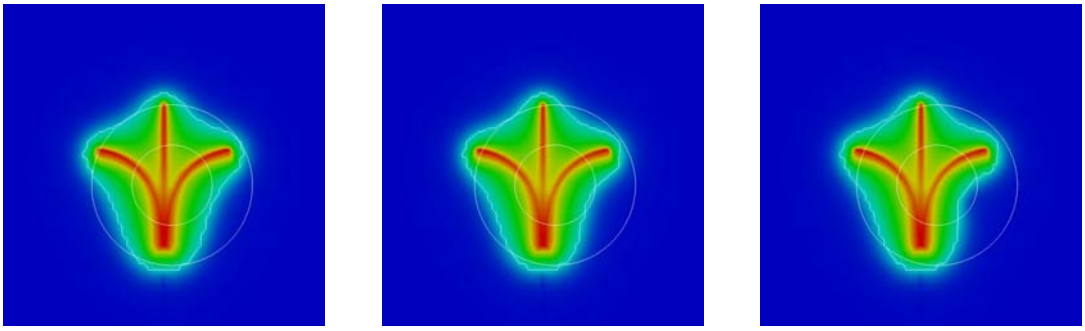

(a) 2 mm (b) 3 mm (c) 4 mm

Figure 6.10: Tolerable deviations to the side from the optimum needle position. Temperature fields have been computed for normal liver tissue (NL) and hyperperfused metastasis (MH).

Needle placement offset	3 mm	4 mm	5 mm
Distance (mm)	4.7	3.5	2.2

Table 6.6: Distance from the tumor surface to the area outside the predicted limit for 99% coagulation (mm) for tumors of 1 cm diameter in needle misplacement of 3 to 5 mm.

6.4.5 Comparison of results with 1-cm tumors

As the simulations with 2-cm tumors gave results of possible undertreatment, we took a look at the situation of tumors with 1-cm diameter. Again we looked at the so-far worst case of normal liver tissue and a hyperperfused metastasis tumor. The smaller tumors do not present such a large source of hyperperfusion as the bigger ones. However, the hyperperfusion still needs to be heated completely to enter vascular stasis early and therefore achieve sufficient coagulation.

We applied the RITA standard protocol for 1-cm tumors, which creates 3-cm leasions according to the following procedure:. Start with an extension of the prongs to 2 cm. Heat the tissue up until the target temperature (105°C)is reached. Extend the prongs to 3 cm. Again wait until the target temperature is reached. Carry on heating for 5 min.

Figure 6.11 shows results for a 1-cm diameter tumor with deviations to the side of 3 to 5 mm. Table 6.6 shows the measured numerical values for these test cases.

The simulations for 1-cm tumors showed no cases of severe undertreatment. Only the safety margin might not be addressed completely. The tumors were heated up completely and therefore reached vascular stasis and coagulation.

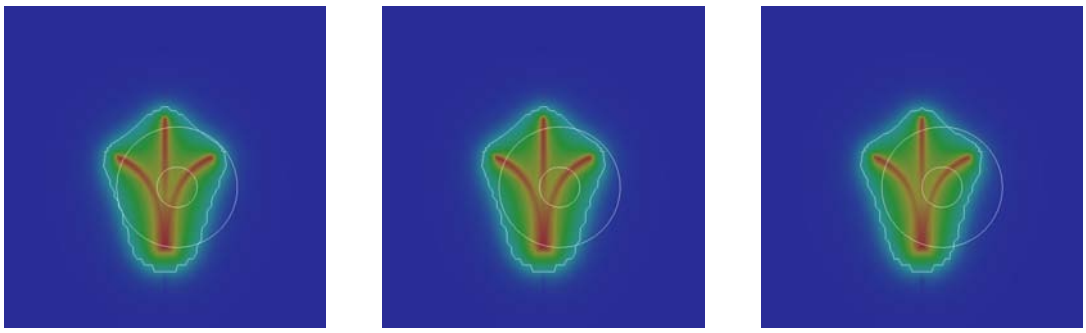

(a) 3 mm (b) 4 mm (c) 5 mm

Figure 6.11: Simulations with normal liver tissue and a hyperperfused metastasis — tumor with a 1-cm diameter.

6.4.6 Running the protocol longer for critical cases

One method of solving the problem of undertreatment with imperfect needle positioning might include modifications of the ablation protocol (for example in the case of bad positioning, one might use a protocol for creating a larger lesion (5 cm instead of 4 cm) or else a modification of the runtime. While all possibilities need to be examined in detail, we performed simulations for slightly modified ablation protocols to understand the effect of time intervals in the procedure.

The modifications in the ablation protocol concern a longer runtime at the end of the procedure by 1 or 2 minutes for the two simulations shown in the upper row. For the lower row the simulations also included extra time (1 or 2 minutes) with an extension of the prongs to 3 cm before reaching the final extension to 4 cm.

The original protocol for a 4 cm lesion is defined as:

```
extend prongs to 2 cm, wait to reach target temperature (105°C)
extend prongs to 3 cm, wait to reach target temperature (105°C)
extend prongs to 4 cm, wait to reach target temperature (105°C)
wait for 7 min
```

We modify in a first step by an additional runtime in the end:

```
extend prongs to 2 cm, wait to reach target temperature (105°C)
extend prongs to 3 cm, wait to reach target temperature (105°C)
extend prongs to 4 cm, wait to reach target temperature (105°C)
wait for 7 min
wait for additional time
```

In a second step we also introduce additional time before extending the prongs for the

last time:

```
extend prongs to 2 cm, wait to reach target temperature (105°C)
wait for additional time
extend prongs to 3 cm, wait to reach target temperature (105°C)
wait for additional time
extend prongs to 4 cm, wait to reach target temperature (105°C)
wait for 7 min
wait for additional time
```

Results of the modified procedures are given in Figure 6.12. Results were computed for normal liver tissue with a hyperperfused metastasis of 2 cm diameter and a needle placement offset of 5 mm to the side from the optimum needle position. Table 6.7 shows results of the numerical evaluation for distances from the tumor surface to the non-coagulated area.

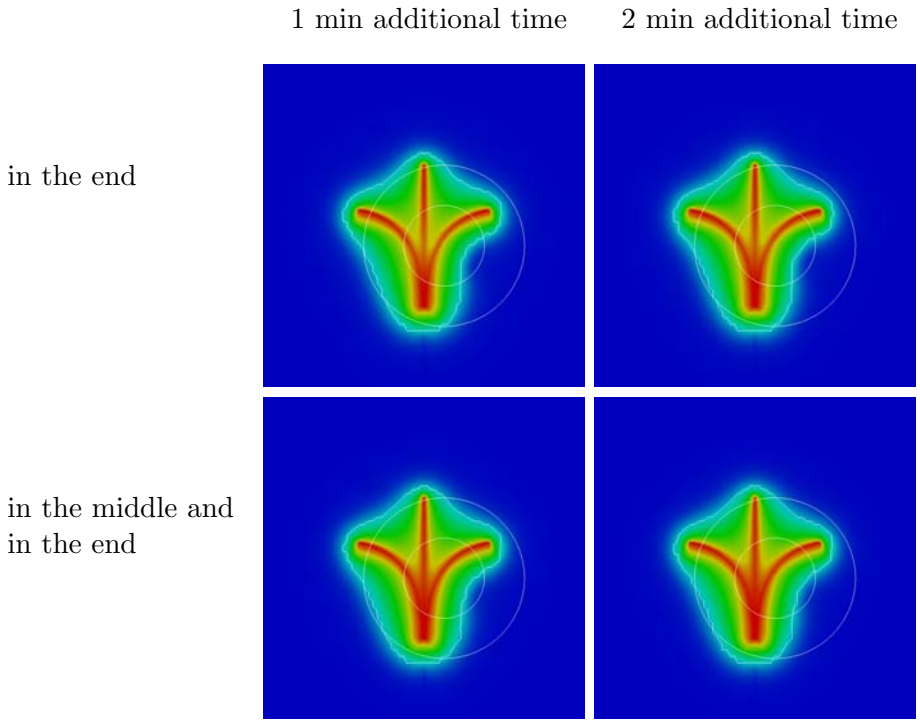

Figure 6.12: Simulation with modified ablation protocol as described above.

The modifications presented clearly show a larger heated area for the tumor and a larger coverage with the area of 99% coagulation. Part of the tumor is still sticking out. So the hoped-for solution to the problem cannot be achieved with these simple modifications of

modified protocol	1 min additional time	2 min additional time
at the end	4.2 mm	4.1 mm
in the middle and at the end	3.4 mm	3.1 mm

Table 6.7: Distance from the tumor surface to the area outside the predicted limit for 99% coagulation (mm).

the procedure. A misplacement by 5 mm to the side from the optimum position clearly demands either a new placement or treatment of a larger area.

All the above presented examinations and observations rely on the model to compute the process correctly. None of the above described state-of-the-art models — nor our model — have been validated with at least some accuracy in a medical study. A current model, extended to meet the needs of RITA, predicts survival of the tumor in cases of misplacement. All the elaborated results only hold if the prediction model can be validated to really reflect results from real interventions. The model encompasses a complete medical procedure, therefore the validation is the comparison with the result of a complete medical procedure. Until this validation is achieved the results of the simulation have to be seen as hints, not as ground truth for modifications of the treatment practice.

Chapter 7

An intervention specific physiological virtual liver

Contents

Computer science support for medical intervention planning is based on integrating additional information into the planning process. The integrated information thereby relies on a model predicting an intervention result. While in the past modeling the anatomy has been most often addressed, current research challenges have evolved into modeling physiological processes. It is absolutely mandatory to validate a model by experiment before it can be used in medical research or even clinical practice. However, designing the validation experiment is difficult. This chapter explains the design of a medical study initiated as a validation experiment for a complete RFA model. First study results present the virtual model's reconstruction suited for use in validation of computational prediction for the RFA process.

To be able to compare the outcome of a medical intervention with a computational result a virtual model of the organ under intervention has to be created. Such a model

deals with a complex situation and not a single aspect. Engineering and computer science skills have to be involved in the data acquisition process and a deviation from standard procedures is necessary to achieve a suitable result.

Building a mathematical model for a real process can be done in two ways: First by theoretical derivation from existing equations, or second, by building an empirically correct description without a theoretical base. Science here mostly evolves in small steps in both directions together. For RF ablation, a description cannot be derived completely from existing physical and chemical equations. The process is not understood well enough in those sciences. The model therefore has to be validated experimentally and to some extent found empirically by providing a computation that reproduces results from findings in experiments. The strength of the model thereby depends on the information that is available to build it: the basic ground truth.

7.1 Data acquired during patient treatment

Describing the procedure in detail is necessary to gain an overview over the data collected from patients during the procedure. The data is not sufficient by far to build a computational model, but even with filling gaps by using phantoms or animal studies, the data collected from patients is the only contribution which later on helps us to transfer findings from other studies into models for patients. The following sections therefore describe which data is available from real procedures, how it is collected, and what needs to be gathered in other ways to build a model with experimental verification.

Taking a close look at the procedure is best done by describing the work flow. In the following section, the emphasis lies on information sources (acquired images and other sources) used by the performing radiologist or surgeon in their task for two reasons: firstly it shows why simulating RF ablation is desired, secondly — as it describes the information gathered in clinical practice — it shows which information collected from patients can be used for building a computational model and for validating a simulation.

7.1.1 Pre-operative phase

A patient with a tumor in the liver has first to be diagnosed by a radiologist. This can be done with different imaging modalities, for example using Ultrasound (US), Computed Tomography (CT), or Magnet Resonance (MR) imaging. If the diagnosis points to a tumor in the liver, which needs to be destroyed by RF ablation, the next step is to plan

the intervention pre-operatively. This is done using either CT or MR images, as these give the best visual representation of the tumor location. Ideally the images used for planning the procedure are acquired no more than three to four weeks prior to the intervention. In this case there is a fair chance that the images show all the tumors with approximately the size which will be found during the intervention. If possible, images that were taken for diagnosis are reused for planning purposes. If these images are not suitable, new images are acquired. CT or MR images for tumor diagnosis are taken with contrast agents. They show all the inner structures in the liver: the vessel trees, the big bile ducts, the gall bladder, and — of course — the parenchyma. These images give the radiologist all the information needed for needle placement.

The data used by the doctor for his decision process is the patient specific MR or CT images, if acquired, US images, and his knowledge and experience of performing the procedure — based on the device manuals. This information, though absolutely sufficient for a skilled radiologist or surgeon, is hard to process automatically. US images can be recorded when acquired, but — as ultrasound presents a 2D slice through the tissue — what can be seen is absolutely dependent on the position and orientation of the ultrasound sensor. This location information is not recorded in clinical practice. The US data can therefore not be used for machine processing as the cutting plane in the image is unknown. Furthermore US images are quite noisy and automatic processing is therefore difficult.

For MR or CT images computers need sophisticated computer vision algorithms and often a higher contrast than doctors do to be able to correctly segment a liver and its inner structure. Segmentation of bile ducts out of those images is a research topic. If vessel trees are not segmented completely (which most often is the case) they might not be reconstructed correctly and a fragment which has to be connected manually might be connected to the wrong vessel tree in the reconstruction process. Tumors can be segmented if they show good contrast in any of the acquired images. The result for image processing on such an image is a virtual model of a patient's liver that is, in the best case incomplete — in the worst case wrong. This is to a certain extent acceptable for a model that is already known to compute correctly. As ground truth for building a model it is insufficient.

7.1.2 Intra-operative phase

The result of the pre-operative phase is a detailed plan of the desired needle position, needle type, and placement path. During the intervention the needle has to be placed

along this chosen needle path. The placement can be done under US or CT guidance.

US images are generated in real time, but are blocked by solids and gas. So US will not work behind the ribs or through the lung. Therefore not every needle path can be chosen. If the needle is placed using US guidance the images are taken with a contrast agent (micro bubbles) to highlight vessels and the tumor. A few seconds after inserting the contrast agent first the vessels light up then the tumor in the parenchyma are visible. The time window for watching these structures is approximately ten seconds. Then the micro bubbles are gone and another injection is necessary if the structures need to be visible again.

Alternatively, a few CT images can be acquired in near real time and these are not limited by bones or air. So for placing the needle guided by CT, a path in between the ribs and through the lung can be chosen. After the needle is placed in the desired position, destruction of the tumor can begin. The generator is switched on and, if deployable, the array of electrodes is deployed according to the device manuals. The following example describes this part of the procedure in detail and shows how to create a coagulation zone with a size of 5 cm using a RITA StarBurst:

The exact desired position for the needle tip is described in the RITA manual [7] and depends on the size the coagulation should have in the end. According to the instruction manual, to achieve 5 cm diameter for the coagulation the needle tip has to be placed at a 1.5-cm distance from the tumor. The created lesion will then extend over the whole tumor and the safety margin as explained in the data sheet for this needle [8].

For the RITA system the RF generator control is based on measurements for temperature and needs various parameters which are provided by the treating physician (power to be used and time for running the generator, etc.) [7]. Figure 7.1 shows a diagram of the created coagulation as predicted by the manufacturer together with the ablation protocol suggested for the desired coagulation diameter.

According to the device manuals, in the beginning the electrode array is deployed 2 cm wide. Then the generator is switched on and step by step the array is deployed further (3 cm, 4 cm, and 5 cm) following the decided ablation protocol. After ablating with the final needle extension, the manufacturer suggests turning the needle by 45° and applying the same maximum extension again for the requested amount of time. This helps to overcome possible deficiencies in the geometrical extension of the needle.

For the whole procedure the RITA Medical Systems' RF generator is able to measure the temperature in every other electrode in the array. It shows temperature information,

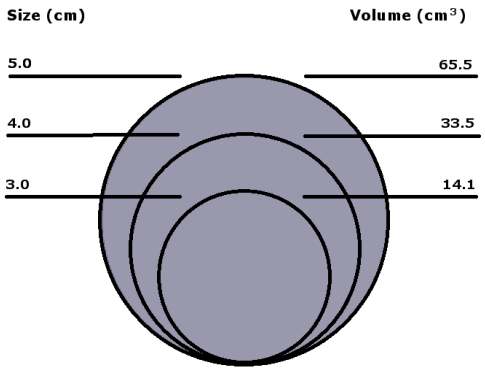

Deploy to:	For a duration of:
2 cm	Until Target Temp. is reached
3 cm	Until Target Temp. is reached
4 cm	7 minutes at Target Temp.
5 cm	7 minutes at Target Temp.

Figure 7.1: On the left side we see the expected coagulations created with deploying the array step by step as described in the StarBurst Device Placement Diagram [7]. Details on how to perform the ablation are written in the RFA for Liver Tumor Protocol [6] The manual thereby suggests an ablation protocol as in an excerpt described in the table on the right.

time, and power used in raw numbers as well as in graphics. Furthermore, it computes the efficiency which is a measurement for conductivity of the tissue. An example graphical output for a procedure on a patient is shown in Figure 7.2.

If the tissue is heated up too much it carbonizes, thereby changing its electrical conductivity to isolation. In this state it is not possible to create large coagulation zones. Whenever the efficiency drops the power is reduced to avoid carbonizing. Therefore, the upper graph in Figure 7.2 shows a rise in temperature with applied power. When the power is shut down temperatures fall with it.

Furthermore, the graphs show the temperature as measured in the five measuring electrodes. These are five spots at the rim of the desired coagulation that represent the temperature in the whole area. Ideally, all five electrodes should show the same temperature measurement. This case gives us reason to believe the assumption that the heat distribution is even as planned. If one line drops and does not reach the same temperature as the others, the tissue is probably being cooled by a nearby vessel. This is an indication of not evenly distributed heat. If one line rises more than the others, this specific tip might be sitting in an area that is not cooled as much as the others, i.e. an area that is not as perfused. Whenever the array is deployed further, the temperature in all electrodes drops as they are extended into not yet heated up tissue. RF waves are then dissipated from the new position and the new treatment region is heated up. According to the ablation protocol in the final extension, the generator keeps running for a set time.

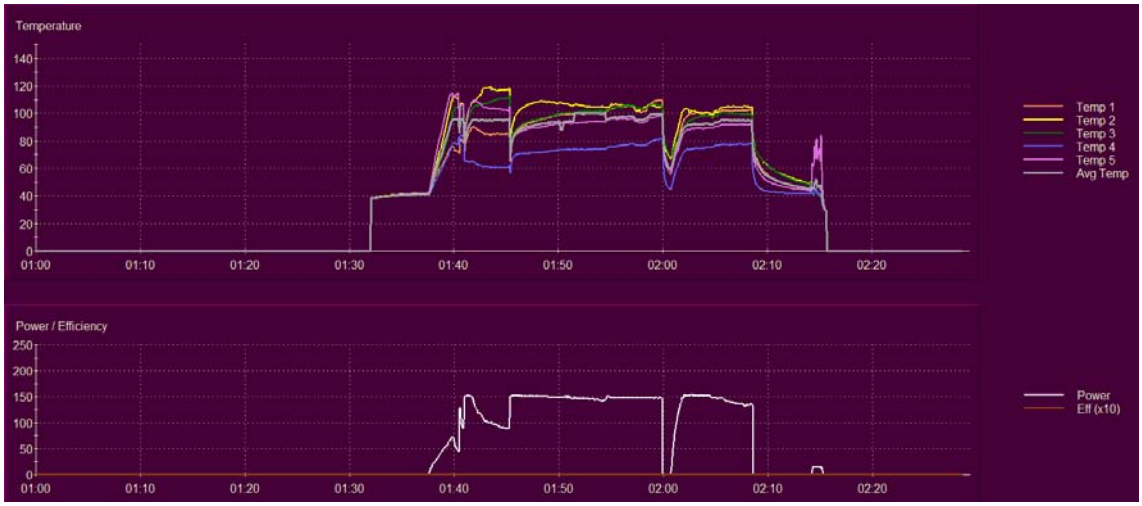

Figure 7.2: An example for the graphical output of a RITA RF generator: The upper graph shows five temperature readings and a computed average temperature. The lower graph protocols the applied power as well as the efficiency in the procedure. In the upper graph we can clearly see the temperature rising at the beginning to approximately 115°C. Then, when the needle electrode is extended the temperature drops in all measurements and much more power is applied to heat again. A second drop in temperature marks again an extension of the needle prongs. Here power is applied at a constant level at the maximum extension. The next drop occurs when the power is switched off. We see stopping the power is followed by a smooth temperature drop. Then agian power is applied. Finally when the needle electrode is removed from the tissue very small power is applied to seal the needle path on the way out. (Data plot taken in the IMPPACT project by University Hospital Leipzig.)

Finally, the RF generator is switched off.

The final result of the intervention is not easily judged. Heat conduction in the liver is patient specific and the result might therefore differ from the planned and expected coagulation. For example, though the coagulation size might have been planned for a diameter of 5 cm for some patients the result has only a size of 3 cm.

7.1.3 Post-operative phase

When the needle is taken out, the generator is running on low power. Heating up the needle path like this, kills tumor cells possibly carried along and closes small vessels along the path so there is no bleeding. Radiologist do an overview CT scan right after the procedure is completed, mainly to show that there is no bleeding in the liver. The necrosis zone is not yet defined. If the radiologist fears insufficient coagulation he can perform another

ablation. Sometimes he might even plan from the beginning to create several overlapping coagulations to treat a tumor that is too big to be treated by one single ablation.

During this part of the procedure a lot of data is gathered, but a lot of information is also not available for building a computational model. The exact location of the needle can only be acquired if the needle placement is performed under CT guidance. Still, the extended prongs change location with every extension during the procedure. So a computational model has to assume the exact prong location. This is once again acceptable if applying a model that is already known as being correct for making a prediction. It is insufficient for building a ground truth.

If temperature measurements are taken by the equipment during the procedure, this information is most desirable as this gives us a very good chance to validate computations or compare whether the prediction fits the path of the intervention during the procedure. Furthermore, a detailed protocol of the power applied and computed efficiency is very helpful in computational reproduction. Obviously, information on the extension and shape of the coagulation zone right after taking out the needle is not available. Unfortunately, this is potentially the most important information for validating a computational model that can only simulate heat distribution to this point. However, assessment of the patient treatment is done in follow up scans.

7.1.4 Assessment of the treatment result

An image acquired right after the procedure does not show the ablation in its final shape. It would also not show parts of the tumor that might have survived. The necrosis develops over a couple of days or weeks after the ablation and changes shape during that time. The liver tissue swells as a first reaction and also the process of cell destruction is carried on after the intervention. An evaluation of the procedures success is therefore done by taking images two weeks (or even one month) after the procedure using CT or MR. Contrast agents show the current shape and extension of the necrosis zone. This is the first chance to detect if a tumor is growing again.

Follow-up scans are taken at intervals of three months to find early indications of recurrences (local or somewhere else in the liver). Comparing the treatment result in these images shows that, over time, the necrosis zone gets smaller as the destroyed tissue builds a scar. New liver tissue grows back, but a left-over of the necrosis remains visible in the tissue forever.

As the goal of a good computational model should be to predict treatment success,

reproducing results from the first images that are taken for treatment assessment has to be the goal. These images are obviously taken a few days or up to one month after the procedure. However, in these images a lot of additional effects, such as regrowth of liver tissue, are also visible. The computation therefore cannot be proved correct by correlation with these images.

7.2 An engineering model for a medical intervention

Data collected from patients during the procedure is often either not suitable for machine processing or incomplete. The intervention described above is very complex and needs to be simplified for a suitable validation experiment. Computations with the aim of predicting the result of this treatment are difficult and a validation study cannot rely on data acquired in clinical practice.

A model suitable for validation describes a physiological process as induced by a medical procedure. Many details influence the procedure's result but, before all minor effects can be integrated, the major ones need to be determined and validated. In a systematic approach, medical as well as computer science requirements can be regarded as forming one joint validation approach.

7.2.1 Heat sink, perfusion, and tissue effects

Model and experimental validation have to reflect the same situation. Otherwise any validation is pointless. Therefore, the first decisions concern the exact capabilities of the model and its reproducibility in a medical study. Furthermore, a first model should be limited to the main and most important effects. It can be extended later. For the RFA process the dominating effect is the heatsink effect due to perfusion in nearby vessels. As the whole process is induced by a radio-frequency generator, the electromagnetic dispersion has to be modeled as well. Both requirements together lead to the demand of using liver tissue which has to be perfused either artificially (ex-vivo) or naturally (in-vivo).

To keep the experiment as simple as possible, minor effects should be neglected for a first study and added later. Liver abnormities such as cirrhosis, which heat differently from normal liver tissue, either have to be modeled as well, or else should not be present in any validation study. Patients with liver metastases rarely suffer from cirrhosis, but still do from a tumor which is reported to heat differently than normal tissue. So either a healthy liver should be treated, which of course will never happen in clinical treatment

practice, or else the model has to compute a more complex situation.

However, a basic model has to be kept as simple as possible to learn from the result and adjust the computation to reproduce the base situation. Therefore, using images from patient treatment for validation purposes is impossible. Furthermore, the treatment has to concern real tissue. So the liver tissue for the validation study has to originate from an animal, where pig physiology is that most similar to human physiology and pigs also have a suitable size for experiments. In any animal or human liver bile ducts build another inhomogeneity. But since bile is a resting fluid, it doesn't contribute to the heat sink effect. Hence, its influence on the size and shape of the necrosis zone is limited.

7.2.2 External factors

External factors are also part of the model to be computed. As explained above, the different available needle types create different necrosis shapes. The simplest version consists of one single electrode. It creates small coagulations with an elliptical shape if there are no vessels present in the surrounding tissue. More complex needle arrays create overlapping effects which make validation of computations more complicated. The RITA RF generator deploys nine needle prongs in an expandable, broom shaped array. The resulting coagulation is supposed to be spherical or at least mushroom shaped. To limit the number of overlaying effects for computation it is important to not expand the needle electrode from one extension to the next, though this is usually foreseen in the RITA protocol.

Together with the needle manufacturer the ablation protocol is determined. The RF generator's power control is implicit in the procedure and cannot easily be influenced. Still the power used can be recorded during the procedure and can therefore be used for the computations. The RF generator by RITA [7] steers power in the ablation protocol oriented on temperature measurements in five of its electrodes. For this manufacturer, power consumption, effectiveness, as well as the five temperature readings are protocolled automatically and can be read by computer. They are therefore available for computations. This will not help with predicting a treatment result, but for validation purpose, the computation fits the experimental situation in this point.

7.2.3 Model limitations

The model does not account for cell death that occurs after switching off the RF generator. Though this effect is important computing it would add much more complexity to the

model. Therefore, it should be added on later, but this means, that the experimental data for the extension of the coagulation has to be taken right after ending the procedure though this is not done in clinical practice.

7.2.4 Resulting measurement requirements

The models described in Chapter 6 rely on solving the bioheat equation and contains parameters which have to be measured in the validation experiment. A full virtual liver model including all relevant inner structures in high resolution builds the geometry on which a solver is to compute the result of the partial differential bioheat equation in a finite element approach. As elaborated above, the relevant structures concern all three vessel trees and the parenchyma. As the RITA generator takes measurements and provides a detailed protocol of external ablation parameters we choose this type. The position of the needle inside the liver and especially measurement lines in the protocol have to be mapped to the single needle electrode prong. Further physiological parameters (blood flow in big vessels, material property constants used in the equation as well as generator specifics) could be measured in complicated additional experiments or simply taken from literature.

7.3 Computer-oriented data acquisition

To reconstruct a virtual liver with all its inner structures, an image modality and imaging protocol has to be defined. Which images to acquire and which modality to use is an especially interesting question: imaging opens a wide range of possibilities. However, medical research and clinical practice when using radiological imaging are oriented on producing images to be interpreted by human experts. Image processing has different requirements and opens new possibilities.

For the validation experiment, it is most important to gain the best experimental results possible. Therefore image acquisition has to be done oriented on image processing capabilities and necessities. As the acquired images are not processed for visualization but for computation, accuracy gains a much higher importance. The algorithms and techniques applied also have to be oriented on low errors (false positive or false negative) and therefore high quality. A semiautomatic procedure providing good results is preferred over an automatic one with a higher error rate.

7.3.1 Imaging anatomy

From a macroscopic point of view the liver consists of parenchyma, three vessel trees (hepatic artery, hepatic vein, and portal vein), as well as bile ducts (compare Figure 1.1). CT or MRI are best suited for a reconstruction in 3D. They differ in their abilities to image soft tissue, in resolution, slice thickness, and in acquisition time. Both modalities use contrast agents to highlight vessel trees. Bile ducts are hard to image, especially with a short acquisition time. But their influence on the procedure's result is minor and therefore not included in the model. So they do not need to be imaged.

A high resolution and especially a thin slice thickness is important when reconstructing vessel trees, as a correct reconstruction can only be done for structures that are visible on the images. Every error in input will propagate and diminish the quality of the simulation result. Furthermore, all registration relies on natural feature points like vessel joints. Medical studies show, that veins with diameter < 3 mm are damaged in the ablation. Arteries are rarely thicker than 2 mm. So according to the sampling theorem (Nyquist-Shannon) images should be reconstructed with resolution of no more than 1 mm — if possible less.

Errors in detection of blood vessels as well as errors on their diameter are best avoided. Detected structures have to be identified correctly as part of a specific vessel tree, because blood flow differs for the three vessel trees. The dominating effects in modeling rely on proximity to vessels. Hence, information on the distance between vessels is very important.

As the designed study is an animal procedure, the radiation dose is not important so that CT or MRI can be freely chosen according to their suitability for computer oriented data acquisition. All advantages and disadvantages have to be considered carefully to gain a suitable model. Table 7.1 compares the image modalities CT and MRI for liver imaging from an image processing point of view.

7.3.2 Subsequent images

Contrast agents are injected into a peripheral vein and carried with the blood flow induced by the heart. So their use is only possible in an in-vivo study or else with artificial perfusion. Furthermore, which vessel tree is highlighted by a contrast agent depends on the timing after injection. First the bolus reaches the heart and from there the liver artery. Next the contrast agent enters through the portal vein and right after that leaves the liver through the hepatic vein. Both venous vessel trees are visible over a short time interval, so an image will always show both venous phases. One of them is just less optimally

Feature	CT	MRI
Vessel trees	Imageable using contrast agent, but a maximum of two vessel trees in one image	All three can be included in one image if not using contrast agent, but three phases are usual
Bile ducts	Not imageable	Imageable
Resolution	Easily < 1 mm	Better at distinguishing soft tissue
Spatial resolution (slice thickness)	< 1 mm	Spatial resolution lower than CT, either thicker slices or very high acquisition time
Acquisition time	Short, ≈ 0.7 s per rotation	Long, difficult to take images with small slice thickness during one breath hold, breathing compensation extends acquisition time
Needle electrode	Blurring	No fragments with special non paramagnetic needle
Necrosis zone	Visible area of missing perfusion, but not exactly the extension of the coagulation	Engineers claim coagulation might be imageable using contrast agent, not accepted by the medical community as yet

Table 7.1: Image modality features in liver images.

highlighted if the timing is correct.

Most reconstructed liver models show one or two vessel trees as these can be imaged in one CT scan as acquired often in clinical practice. Nevertheless, for validation purposes it is necessary to fit the experiment to the model at least when dealing with dominant effects. All three vessel trees contribute to the heat sink effect. Therefore, a virtual liver model used for computation has to include all three vessel trees. Moreover, it is important to image the vessel trees completely and identifiably, as every vessel tree holds a different flow rate and therefore contributes to the heat sink effect differently. As computer vision is able to fuse information from more than one image and more than one modality, it is more important to take images that show the desired information for one structure completely and identifiably, than to show many structures together, but none of them very good.

Every image taken has to be segmented to gain a reconstructed liver model. Segmentation is eased by high contrast, therefore in the study a high dose of contrast agent should be applied. Every additional image after the first one has to be registered to a first one, so the information can be fused in one single volume.

The main reason for deformations of the liver is breathing. Deformations due to

heart beat are minor and can be neglected. So, as long as image volumes are taken with the breath being held no deformations are present in subsequent acquired images and information can be fused directly without non-rigid registrations. This results in a high reliability for location and size of the imaged structures. Acquisition time for one single image volume has to be short to be able to take three image volumes without the subject breathing. In this case registration is implicitly given if there is no movement or deformation in between acquisition of subsequent images.

7.3.3 Other geometric information

As the whole process is induced by a radio-frequency generator, the electromagnetic dispersion is computed as reason for tissue changes. It originates in the needle prongs which are the relevant geometrical information for the medical instruments used in the procedure. Its location is determined from the same images as the anatomical structures in the liver.

The result of the intervention cannot be reliably imaged in any modality. In a CT scan, a non-perfused area can be imaged. If this area fits the necrosis zone in the end is unknown. There are hints that MR images show the coagulation right after the intervention [31]. However, this hypothesis has not yet been validated well or accepted in the medical community. Medical research relies on histological examination of the area showing intervention results, as this gives insight into cell status. But comparing histological images to radiological ones is a difficult registration task. For a first approach, our computation model will not include cell death but only predict the heat sink. Therefore, a comparison to the non-perfused area after the intervention is sufficient.

7.3.4 Annotation with non-geometrical acquired data

CT images can only show the location of the needle inside the animal. The needle prongs are visible but not identifiable from that image as they cannot be distinguished by form or material. Still from outside the animal the location of the first needle prong (which corresponds to the first measurement line in the RITA protocol) can be seen as it points to the same direction as the connection for saline input on the needle electrode. We note for every ablation the rotational angle at which the needle tip is sitting during the ablation after needle array deployment. At that time the needle cannot be rotated any more.

The physiological attributes such as tissue properties are much harder to measure as this is not done by standard medical equipment. In the literature investigators often rely

on self-built test setups which are not standard equipment. In order to keep the influence of tissue properties constant we decided on two ablations per pig — one peripheral, one central (so one without heat sink, one with heat sink). Our experiment had three phases: first before any ablation is done, second after the first ablation, third after the second ablation. All other physiological or physical properties can then be taken from the literature. Any error in these properties would affect both computations equally and therefore introduce errors which would not concern any important part of the equation.

7.3.5 Resulting data acquisition protocol

For our validation experiment we used a porcine model. A porcine liver is big enough to provide space for looking at extensions of RFA-induced coagulation. At the same time porcine physiology is similar to human physiology. Ablations were performed using the RITA system with temperature control. In this way, a machine processable protocol was written and temperature measurements were taken in the five measuring electrodes which served as measured treatment effects and ground truth for later comparison to simulation results. For our study the electrode array was extended to a fixed 3 cm position which was not changed during the intervention. In this way, the number of overlapping effects visible in the treatment results was kept to a minimum. Figure 7.3 shows the needle with a 3-cm extension.

Figure 7.3: The RITA Starburst device: in this picture the array is deployed to an extension of 3 cm as used for the animal study. So this is the structure visible as the needle in the animal CT scans.

The needle was imaged in its deployed position to gain the exact geometry needed for computations. As the needle is built from metal it generates reconstruction artifacts in the acquired images. So information on structures close to the needle cannot be obtained from images which are taken with the needle. Hence, images that show the treatment result should not be taken at the same time as images showing the needle position.

To fulfill the requirement of identifiably imaged structures as geometry input an acquisition of three separate images in three phases would be best suited, each one highlighting

one single vessel tree segmentation. A high-end CT scanner can produce images with a high resolution and a small slice distance with a short acquisition time, which fixes our best chosen imaging modality to CT. We took three volumetric CT images in the same respiration phase per experimental cycle. Images were reconstructed as a $512 \times 512 \times 320$ matrix with a slice distance of 0.5 mm. Sure-start region-of-interest detection within the aorta started 5 s after the image intensity had reached 180 Hu in the aorta. Since a 320 line CT was available we can take a whole volume within one rotation. In our protocol the portal vein scan was performed between 20 s and 25 s after the arterial scan and after another 25 s, the hepatic venous scan was performed. These values depend on the metabolism of the pigs and are specified when the weight of the pig is known.

One ablation took a couple of minutes time, so the pig was breathing during the ablation and images taken for the same phase in different experimental cycles showed the same structure but with breathing in between the image acquisition. Therefore, the images showed breathing deformations. To keep the deformations small and easily to handle the images were taken in the same breathing phase. A non-rigid registration is still needed to cope with the deformations. The resulting imaging protocol is shown in Figure 7.4.

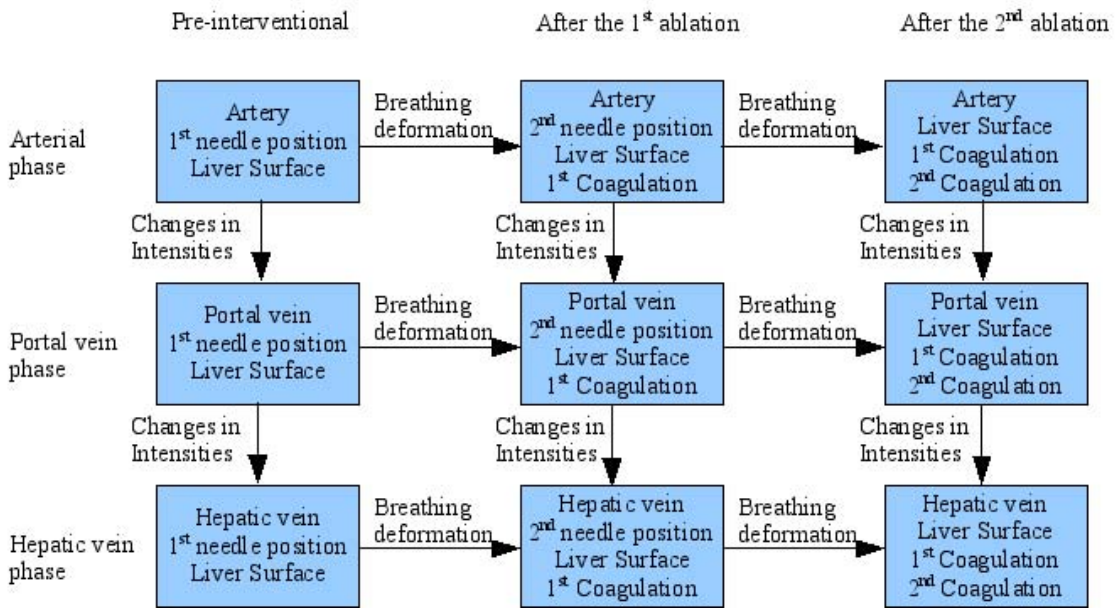

Figure 7.4: Relations between the 9 acquired CT image volumes and the respective registration conditions. On the left side the different scanning phases are listed, above different acquisition times in the intervention. The boxes show what is visible in respective CT image.

7.4 Image processing

For the validation study we took 9 images as shown in Figure 7.4. All 9 images hold specific information where a set of 3 images shows the complete liver at a specific point in time. Here segmentation was the engineering challenge. To gain a 3-image liver we segmented the three vessel trees out of the liver images that could be combined directly.

To look into the changes over time during the intervention and be able to combine information from different time steps the engineering challenge is registration. By combining information from the pre-interventional scan and the scan taken after the first ablation with the scan taken after the second ablation we were able to integrate needle positions and the resulting necrosis zone into one dataset. The result was a virtual liver model showing all the necessary information for our validation study.

7.4.1 Segmenting images from one timestep

We evaluated the image protocol for a sequence of three images by comparison of segmentation results with results achieved on standard data sets from clinical routine using the same segmentation methods. Results showed that typically up to ten times more vessels can be extracted and the surface accuracy is improved.

The post processing algorithms and techniques applied have to be oriented towards avoiding segmentation errors. Semi-automatic methods producing good results are preferred over fully automatic methods that may produce errors. However, user interaction should be kept as low as possible. Having more than one vessel tree highlighted in the same image makes connecting vessel fragments in post processing difficult in situations where two vessel trees cross or lie close by.

From the three volumetric datasets the liver itself and the different vessel trees are segmented as outlined in Figure 7.5. The liver itself is clearly visible in each of the datasets and had to be segmented only in one of the datasets, while the different vessel trees were only imaged optimally in the right phase of the contrast agent distribution and segmented in the according dataset.

For segmentation of the liver the semi-automatic method of Unger et al. [151] was used. The method is based on a 3D global optimal surface finding method embedded as a total variation formulation that allows for an efficient GPU based implementation. The tool requires specification of object and background seeds and adapts the segmentation to boundaries in the image domain separating these seed regions. The method allows for full control over the segmentation result, but typically requires only minimal user inter-

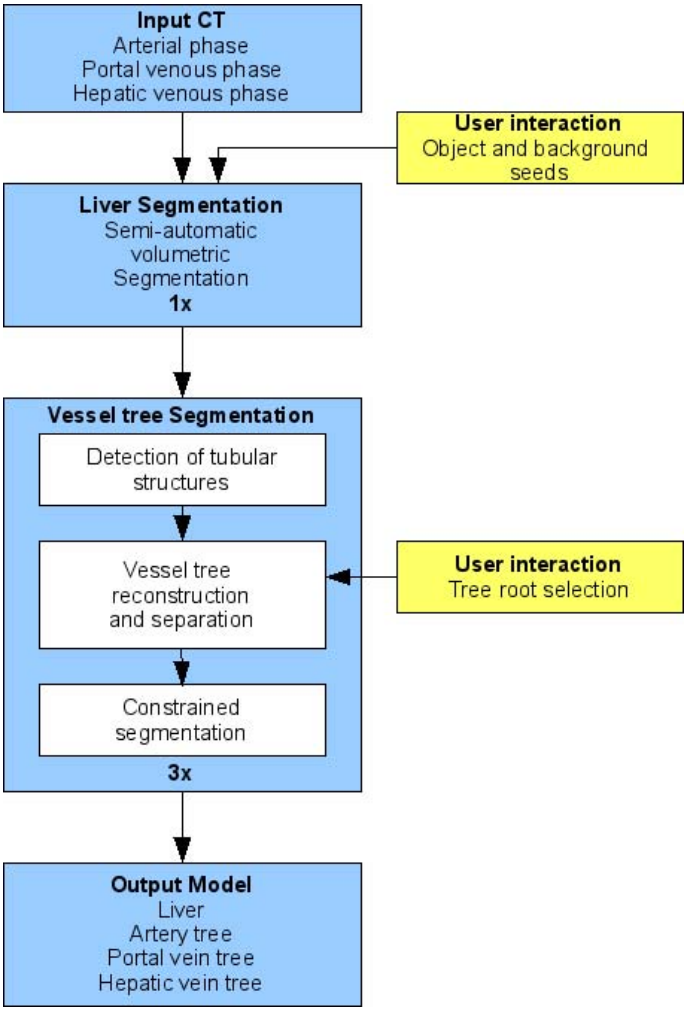

Figure 7.5: The image processing chain for segmenting vessel trees in the liver: We used three images that imaged the vessel trees with as much separation as possible. First the liver surface was segmented semi-automatically to limit the space in which vessels were searched. This required a minimum of user interaction for marking object and background. The step can be applied once for all three images, as there is no deformation in between three phases taken in breath-hold. Next we segmented one vessel tree by detecting tubular structures, selecting a root for the tree, and performing a constraint segmentation. This had to be performed once per vessel tree. Finally we obtained the output as one liver surface and all three vessel trees.

action. In an evaluation performed by Unger et at. [151] on a publicly available database for segmentation of liver CT datasets with manually generated reference segmentations (`http://sliver07.isi.uu.nl`) average root-mean-squared surface distance of 1.93 mm was achieved with this method. This value is comparable to the inter-user variance of trained observers and also competitive with other methods specifically developed for liver segmentation [71].

For segmentation of the vessel trees an approach based on previous work of our institute [125] was used. The approach initially identifies all tubular structures in the dataset in a fully automatic fashion. In a subsequent step, a user can select the roots of the different vessel trees and the associated vessel systems are reconstructed based on anatomical knowledge about the structure and the branching pattern of vessel trees. This allows separating multiple interwoven vessel system and generation of completely connected skeletons. In the last step, the derived information is used as a shape prior to constrain in the actual segmentation. The method has been evaluated on clinical datasets based on an assessment by an experienced radiologist who verified the method's ability to identify all visible vessels successfully, to separate and to accurately segment the different vessel trees correctly. Details of the method and the evaluation can be found in [17].

For evaluation, we present results achieved with these segmentation methods on CT dataset of human livers that were acquired with standard imaging acquisition protocols as used in clinical practice and compare them to results achieved with the proposed imaging acquisition protocol on pig livers. The protocol also allows optimal imaging of all three vessel trees as shown in Figure 7.7.

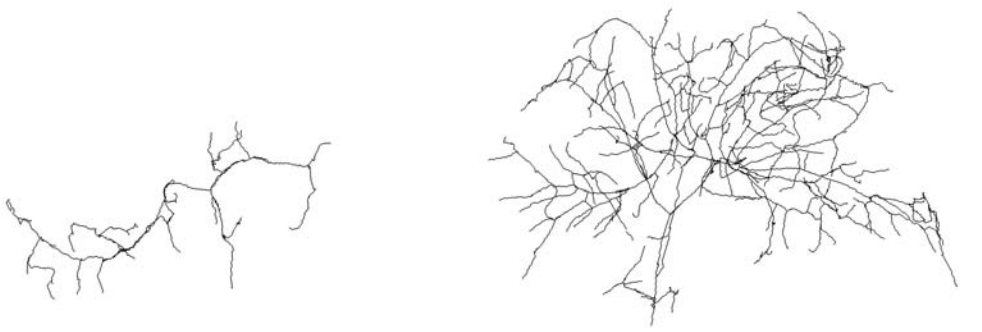

Figure 7.6: Extracted portal vein center lines for a low contrast and low resolution CT dataset of a human liver (left) and a pig liver imaged with the presented protocol (right)

To account for the different anatomy of humans and pigs we compared the percentage of segmented vascular volume relative to the segmented liver volume. We are able to identify typically up to ten times more vessels with our protocol on pigs compared to a standard protocol applied to patients. The difference can be clearly seen on the portal vein tree example in Figure 7.6. While this Figure shows one example dataset results would be comparable for other datasets acquired with the same protocol. The segmentation results have been judged by Prof. Dr. Portugaller to be typical results for the image acquisition protocol. Still segmenting these datasets is time consuming and therefore neglected here. The imaging protocol presented also allows us to generate much smoother and detailed liver surfaces shown in Figure 7.8. The accuracy of that surface is a central requirement to guarantee a reasonable simulation within the liver.

Figure 7.7: The protocol presented allows reconstruction of all three vessel trees in detail.

Our method would allow a fully automatic processing if a better control over the bolus timing could be achieved. The aim would be to take really separate images for all three vessel trees which also should be homogeneously highlighted and completely connected. Unfortunately, pig perfusion is too fast to obtain the images homogeneous in brightness and clearly separated between the portal venous phase and hepatic venous phase.

Alhonnoro et al. [4] evaluated their vessel segmentation algorithm, which was developed in the context of the IMPPACT project, on images taken according to the protocol. The algorithm is able to extract 97 % of the relevant vessels for RFA computational simulation (vessels with a 3-mm diameter or wider). Accuracy is better than the reasonable resolution for finite element modeling and therefore the algorithm is suitable for processing the acquired images for RFA simulation.

Figure 7.9 shows a pig with the complete data acquired from one point in time. For this example, we used the 3rd cycle. Due to the construction of the radiological imaging protocol the data can be reconstructed with all three vessel trees without any registration.

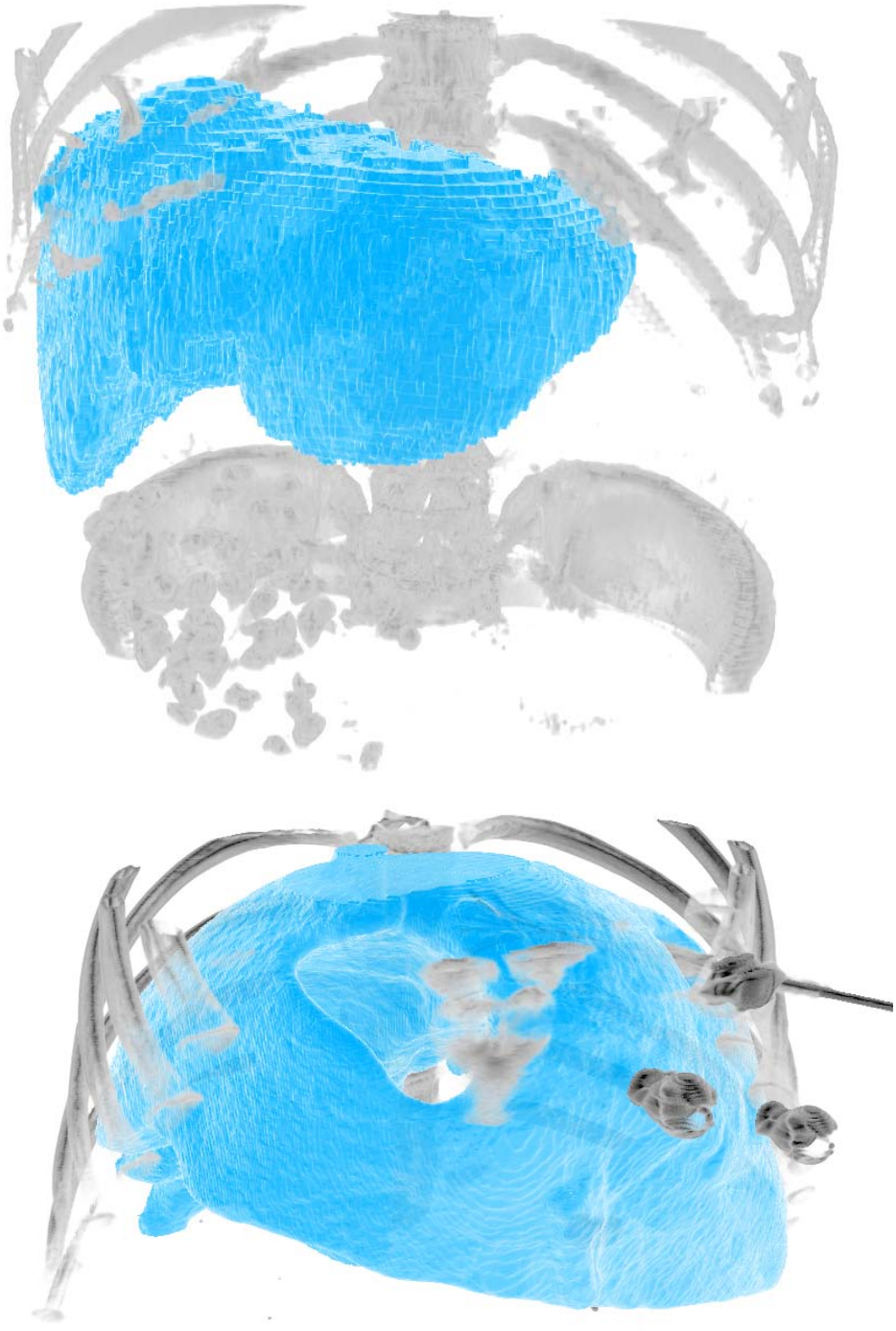

Figure 7.8: Comparison of segmented livers for one example dataset from (top) a low contrast and low resolution (3 mm) CT dataset of a human and (bottom) a high contrast and high resolution (0.5 mm) CT of a pig. In the pig dataset the hole in the liver results from the gall bladder and stomach that were not considered during segmentation. Additionally, a part of an ablation needle and an optical tracking target are visible.

The three vessel trees were already acquired in the same coordinate system as guaranteed by the CT scanner. As the pigs in the animal study were held under general anesthesia they cannot move where any residual movement would lead to motion artifacts in the CT images.

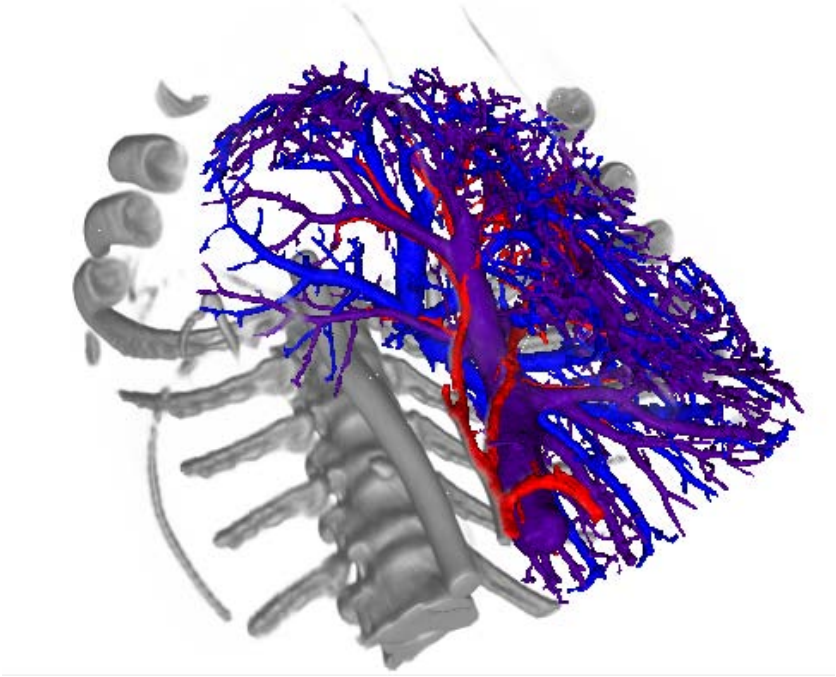

Figure 7.9: A sample CT reconstruction of a pig with 3 segmented vessel trees. Due to the imaging protocol this reconstruction can be performed without any registration of the image volumes. This is possible for every dataset acquired with the discussed imaging protocol but was performed only on a very limited number of datasets, as segmentation is time consuming. The red vessel tree is the hepatic artery, the purple one the portal vein, and the blue one the hepatic vein.

7.4.2 Registration of subsequent images

Images acquired at different time steps in the imaging protocol are deformed due to pig breathing in between the image acquisition times. As each set of images is always acquired under held breath and always in the same breathing state, deviations that need compensation by registration were kept small. Nevertheless, the deformations demand a non-rigid

registration. The liver surface could be a hint for the performed deformation, but positions of inner structures, like vessels, are also relevant to compute the inner deformation. Figure 7.10 shows the deformation from one cycle to the next for the same breathing state by overlaying the vessel information acquired in two subsequent images.

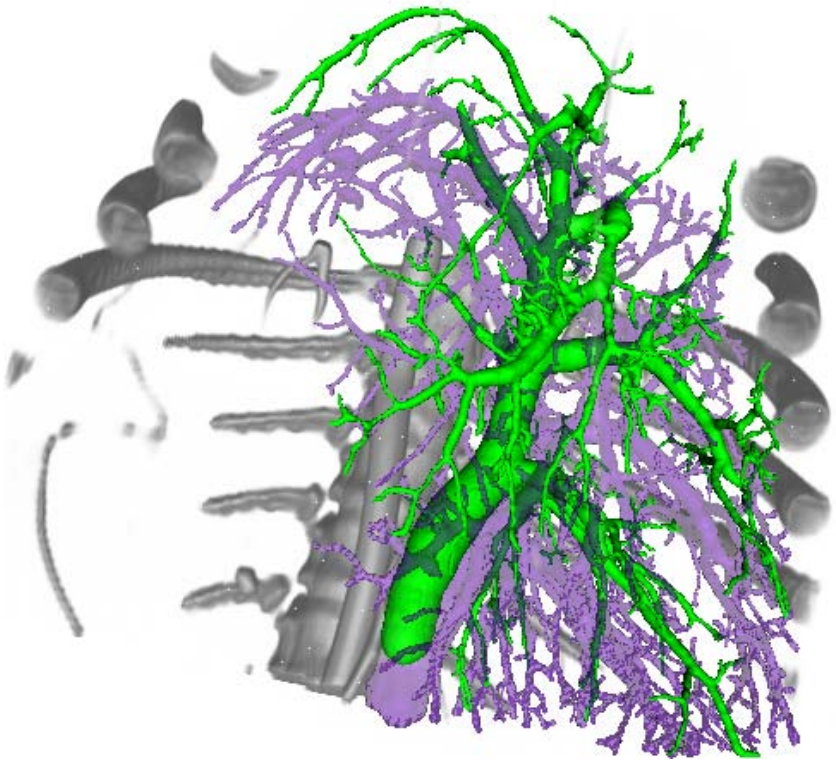

Figure 7.10: Breathing deformation for a pig liver: the bones and the purple portal vein are shown as acquired in the 3rd cycle. The superimposed green portal vein was segmented from images taken in the 2nd cycle. The visual differences show the need for registration in between two cycles.

Figure 7.11 shows the available information per CT image stack. All image stacks show the liver surface and for each imaging phase the respective vessel tree is imaged. This information is redundant through the respective images and is therefore used for registration. The first two image sets hold the needle positions as unique information. The last image set is the only one not holding a needle but showing all the coagulations.

For the simulation we need the following information

- needle position
- vessels (relevant to the heat sink effect)

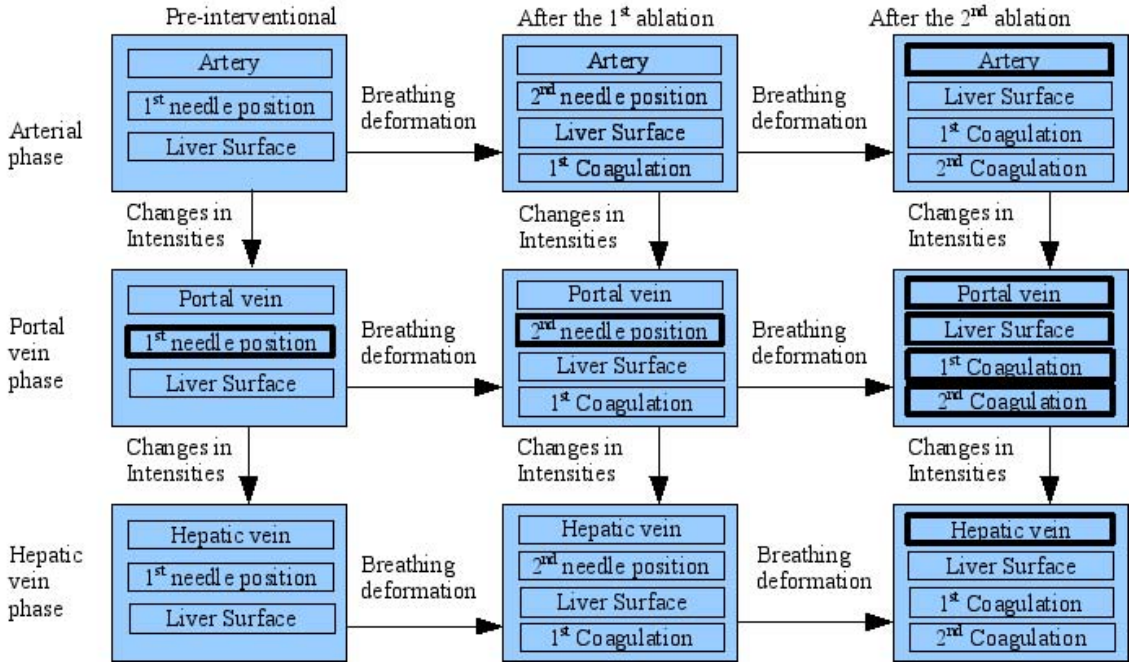

Figure 7.11: The complete information from the images. Every box presents one image stack acquired at a specific point in time. While columns present image stacks acquired as a sequence with no deformation rows present the same type of image acquired at three different points in time with breathing deformation in between. The thick borders present the information acquired uniquely in specific images. The thin borders show features which are redundant between different images.

- coagulation as result of the intervention

To evaluate the result of the intervention together with the input situation the position of the needle and the coagulation have to be fused. The position of the needle in the first and second data set have to be transferred to the third dataset. So the desired registration fuses information along the time axis in Figure 7.11.

Taking a look at new and redundant information we see, that all relevant information can be processed relying on 5 out of the 9 CT image stacks. We chose the CT images acquired for the portal vein phase for deducting the needle position as these show the most vessel trees in one CT image stack and therefore work best for registration. The 4 additional image stacks can be used to enhance accuracy by recomputing the needle position and taking the average over the positions, as well as for judging the accuracy of the registration.

In the first two datasets the most important information is the position of the needle.

Unfortunately the needle introduces artifacts in the CT image stack as shown in Figure 7.12. The needle lights up like a star and blocks correct reconstruction of the area behind the needle. The effects arise due to the needle material: metal with easily moving electrons in an imaging modality based on X-rays. So the vessels around the needle are not perfectly imaged.

Figure 7.12: CT scans which hold the needle show artifacts. The white shining needle overlays any information close to the needle. Furthermore, black shadows result from errors in the reconstruction of the measured x-rays in the area behind the needle.

The artifacts hindered segmentation of the vessel trees in these images. A segmentation does not find vessels in close proximity to the needle. This can be seen in Figure 7.10 where the green vessel tree, appearing to sit in front, was acquired from an image which was taken with the needle in place and therefore shows much less detail especially on the left-hand side, where the needle sits. So the first idea to register already segmented vessel trees to each other cannot produce the required information. We therefore took the information on vessel trees from the third image set. These vessel trees definitely include all vessels participating in the heat sink effect (as these are still visible after tissue coagulation), but possibly do not show smaller coagulated vessels. For two pigs we therefore took an additional image set with the same contrast phases pre-interventionally before needle

placement to be able to judge which vessels had been destroyed in the process.

The same artifacts that render segmentation difficult also hinder registration oriented on similar features within an image. Even an algorithm orientation on similar features and working on complete image stacks, cannot rely on the information in close proximity to the needle tip and therefore has to orient stronger on farther away pixels. As changes in images due to registration are kept small, possible errors introduced in the registration step are also kept small even with a nonsophisticated algorithm. We used the publicly available registration tool *airwc* [9] to register nonrigidly the CT images from subsequent cycles. Figure 7.13 shows the result of an example registration using *airwc*.

Figure 7.14 shows the registration step in more detail. Here we see axial slices of the CT scans. We compare slices close to the needle position to see the effects of the registration. On the left the original second scan showing the second needle positioning is presented. On the right slices from the last scan showing the created lesion are presented. The middle column shows slices equivalent to the left column but in the target coordinate system. As this also means a shift in the axial direction the equivalent features are now shown in different slices. So the left column shows slices #106–#126 but the middle column and the right column show slices #91–#111.

Unfortunately, *airwc* performs insufficiently in the area around the needle due to the needle artifacts. So for one example (pig # 37) we computed the distance of the needle tip position to the respective point in the coagulation (where the needle tip was obviously sitting) for all three phases and both lesions. In this example one coagulation was very clearly visible, one was hardly visible. Table 7.2 shows the resulting computed differences.

The distance between the needle tip and the respective coagulation point extended up to a maximum of 17.0 mm in a case where the lesion was barely visible. So we can see the manual postprocessing step is necessary. We used the *point based registration* filter implemented in *MITK* [95], [161] to push the needle into a position aligned with the visible area of coagulation. The manual processing step allows the accuracy be determined by the human user. We believe that an accuray of 3 mm is resonable for clicking one spot in the *MITK* implementation. The result of the registration procedure would be easily judgable by visualizing comparison images like Figure 7.13 in 3D. This unfortunately requires time consuming segmentation of vessel trees.

Another error source is the possibility of the needle tip and needle prong bending when the needle is inserted. However, bending is not pronounced as the prongs are only extended to a position for 3 cm images. Any deviation from bending needle prongs produces less

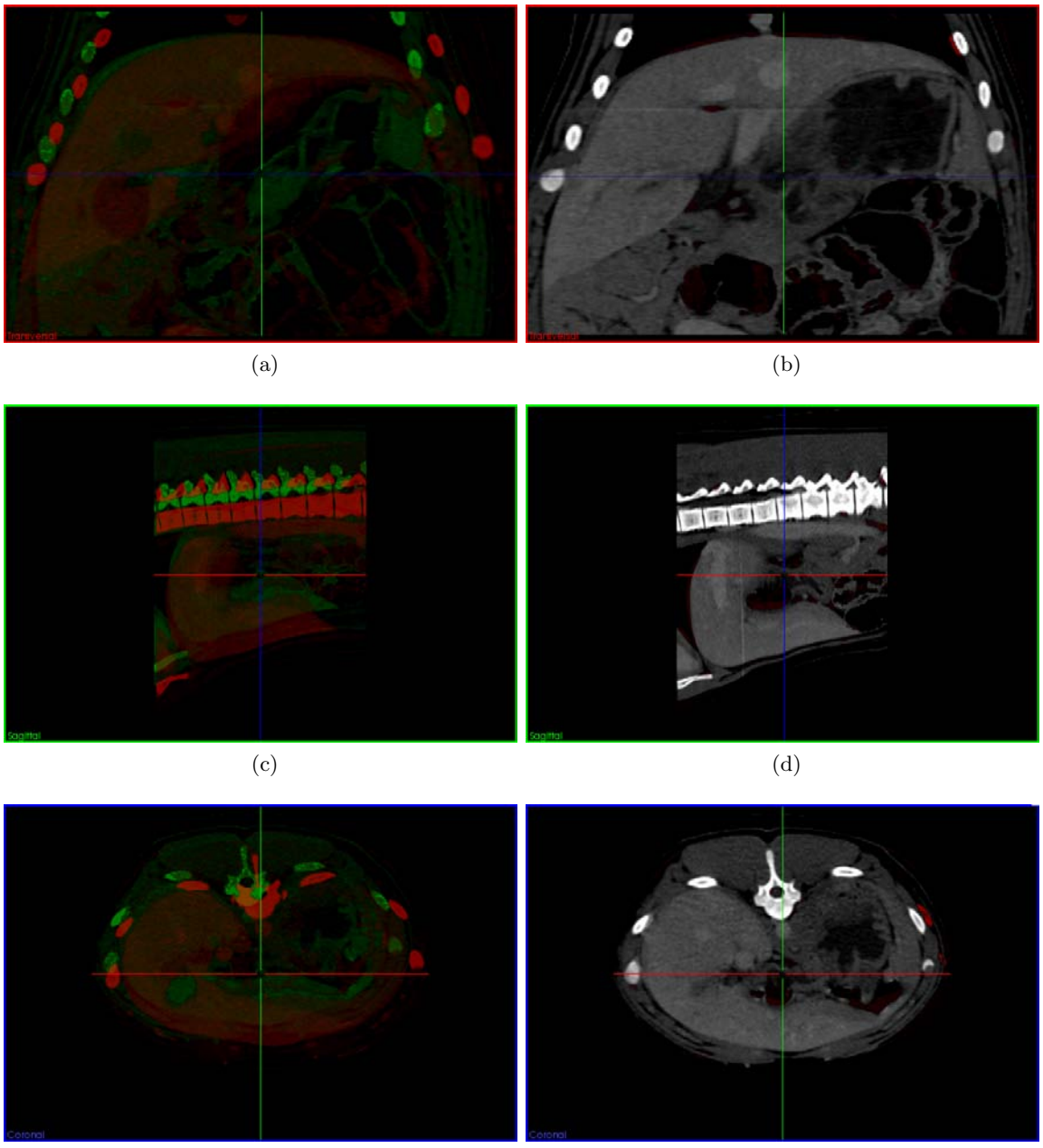

(a) (b)

(c) (d)

(e) (f)

Figure 7.13: Registration to compensate for breathing deformations using airwc. Images are presented overlayed shown in green/red. On the left side (a, c, and e) we present unregistered data sets. The right side figures (b, d, and f) show the result of the registration step using *airwc*. We see that most prominent features fit. Only in f can we see two red ribs where *airwc* did not work correctly. This example used data from pig #37 acquired in the hepatic venous phase.

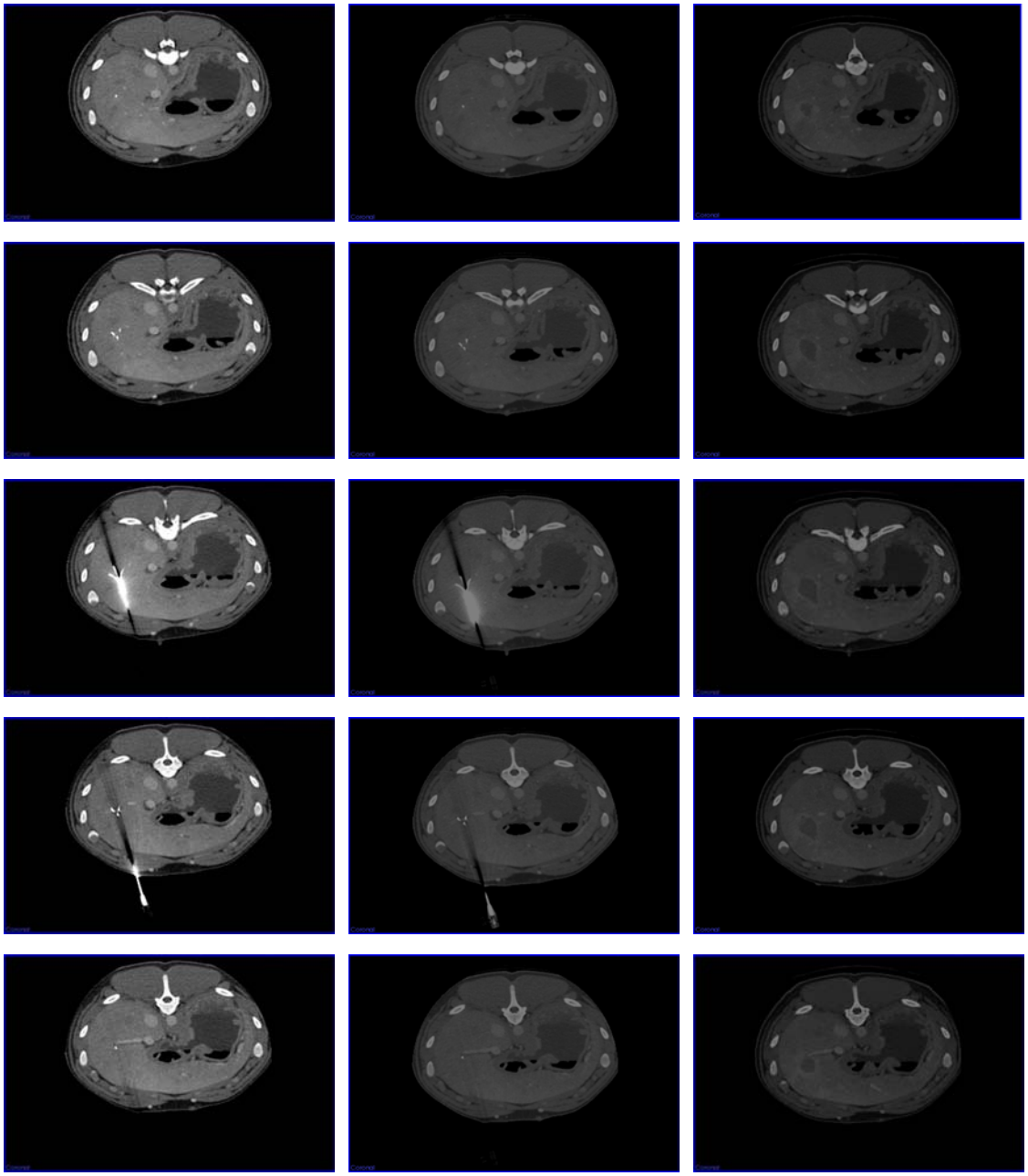

Figure 7.14: We see samples for of the registration procedure, i.e., CT scan slices from pig #37 acquired in the portal venous phase. On the left, the original CT scan showing the second needle position is presented. The needle is shown as white spots in the liver. On the right, the registration target scan, i.e. the original CT scan after the intervention with the lesion but without the needle is shown. A darker area can be seen in the same position as the needle in the other scans. The middle slices are equivalent to the left column but after registration to the final scan. Slide numbers are shifted to account for axial changes in the registration procedure.

Lesion #	Phase	needle position [mm]			respective coagulation position [mm]			manually refined distance [mm]
1	Arterial	91.7	−105.2	79.9	95.7	−106.5	76.4	5.4
1	Portal Venous	92.1	−229.8	83.8	95.7	−232.0	89.1	6.7
1	Hepatic Venous	93.4	−106.5	82.2	93.4	−118.7	74.1	14.6
2	Arterial	66.4	−89.9	106.3	77.3	−98.5	96.5	17.0
2	Portal Venous	68.9	−210.4	108.0	74.9	−208.4	99.0	11.1
2	Hepatic Venous	67.5	−91.8	110.3	72.7	−94.2	104.6	8.1

Table 7.2: Processing variances for the registration procedure: We see different measurements for the position of the needle tip and the starting point of the coagulation zone for pig # 37. The distance varies from 5.4 mm in a case where the lesion is highly visible in the image to 17.0 mm in a case where the lesion is barely visible. The same detailed variance measurement can be performed for all 12 datasets, but due to the manual processing step is time consuming.

error than the lack of accuracy from non-ideal image registration and is therefore negelcted here.

7.5 Virtual physiological liver

With the applied image processing the virtual liver model is complete. Due to the specific data acquisition method it shows all the relevant inner structure completely and correctly. As the process of RFA is not completely understood in the sciences describing the basic ground truth it cannot be modeled by combining theoretically derived equations. A description has to be found empirically and the created virtual liver model allows testing of empirical simulation results.

A total of 46 experiments were performed in the context of the IMPPACT project up till August 12th 2010. Out of 46 pigs 12 were imaged with sufficient quality (not too many artifacts, good separation between contrast phases) to be suitable for image processing with an available common purpose registration program. Table 7.3 gives an overview over the processed data and the needle positions found. For all these pigs registered images are available. So for every pig a 5-liver virtual pig can be reconstructed.

For understanding shortcomings in any given RFA simulation model, human users need to think about the result, meaning visualization of the acquired data is essential. We visualized the created virtual liver model using the system described in Section 5. The system is able to show both polygonal surfaces and volumetric radiological images

Pig #	Earmark	RFA Date	Needle position 1st lesion [mm]			Needle position 2nd lesion [mm]		
			x	y	z	x	y	z
18	61	4/27/2009	111.2	−169.0	−35.4	76.5	−148.3	−20.4
20	73	4/28/2009	129.1	−156.6	27.0	50.4	−143.0	−41.4
26	78	5/13/2009	73.6	−136.8	−131.4	93.6	−55.1	−106.0
27	76	5/13/2009	21.8	−27.4	−172.8	62.6	−81.0	−55.8
31	96	6/24/2009	101.8	−161.8	−118.3	71.0	−187.9	−99.3
32	88	6/26/2009	116.2	−192.3	−84.8	75.7	−147.9	−90.2
36	87	3/29/2010	83.6	−289.0	101.1	47.4	−171.1	124.1
37	86	3/29/2010	95.7	−232.0	89.1	74.9	−208.4	99.0
40	38	5/17/2010	158.5	−131.3	−29.4	81.4	−107.5	−53.8
41	39	5/17/2010	135.2	−308.0	100.3	60.8	−173.8	166.4
42	66	6/8/2010	90.5	−117.5	−33.0	145.7	−125.8	−18.4
43	65	6/8/2010	92.6	−113.1	−36.6	85.1	−97.7	−51.7

Table 7.3: From the 46 animals used in animal studies the best 12 have been processed using freely available image processing tools. The table shows the computed needle positions for both lesions per pig.

together. So every structure could be seen directly in the volume by adjusting a grey value window or editing a transfer function. At the same time every structure that has been segmented can be visualized as a surface. Figure 7.15 shows such a virtual liver for one performed ablation. The liver model is therefore constructed from the information of 4 acquired images focused on the time slot after the first ablation. Inclusion of the 5th image would show a second ablation area and a second needle, thereby leading to confusion over which ablation process is currently being examined. It is therefore omitted here.

Close up observation of the virtual liver shows the extended prongs of the needle, see Figure 7.16. The figure also shows the measurements from the RITA needle. The needle prongs are colored according to the measurement line in the RITA plot to allow us to match the recorded measurement line with the respective needle prong.

Physiological values are mainly interesting for simulation purposes. They can be taken from the literature. However, the ablation protocol shows power, efficiency and temperature measurements recorded for this needle and this specific pig. Those values were measured during the study and are visualized together with the volumetric data in Figure 7.16.

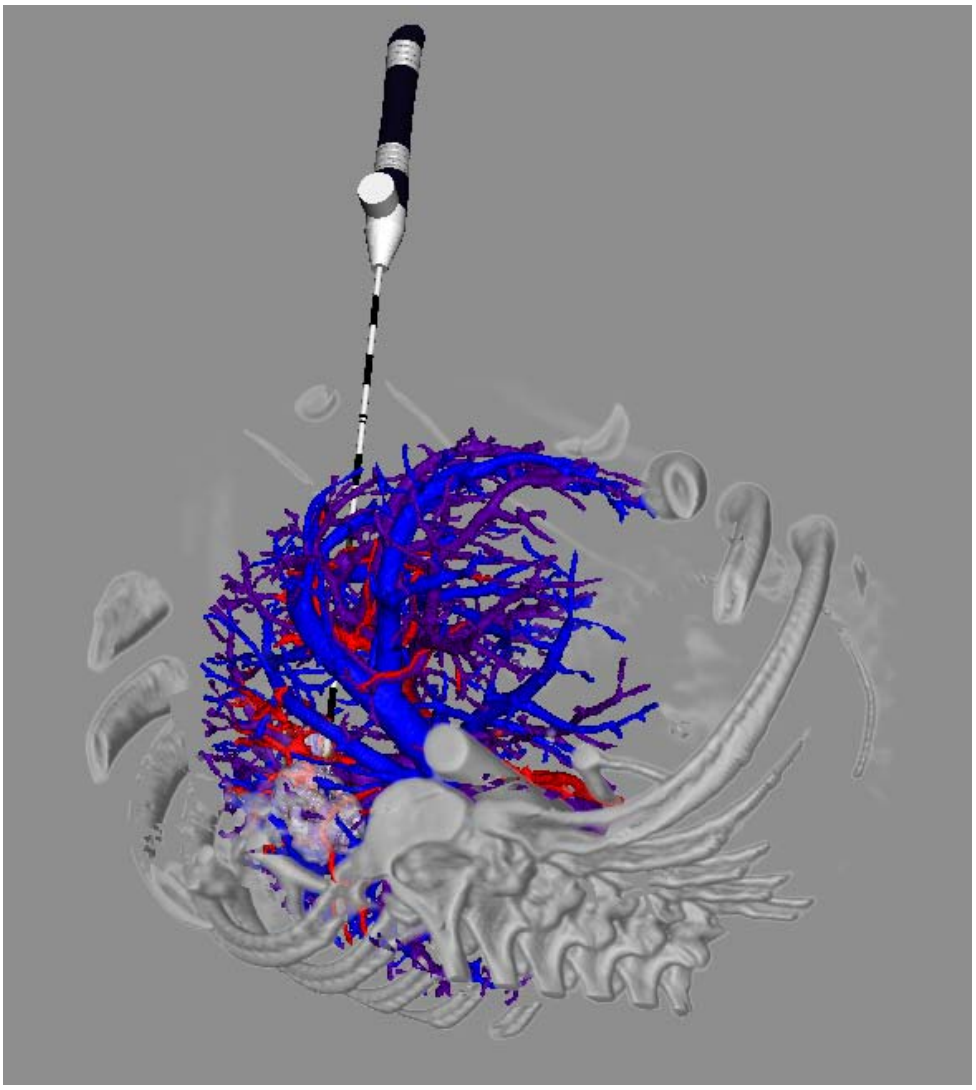

Figure 7.15: Virtual physiological liver, reconstructed from 4 CT-scans: The image shows a pig after the intervention. Vessel trees as well as the coagulations have been segmented. The artery vessel tree is shown in red, the portal vein in purple, the hepatic vein in blue. The coagulation is presented as a partially transparent white volume.

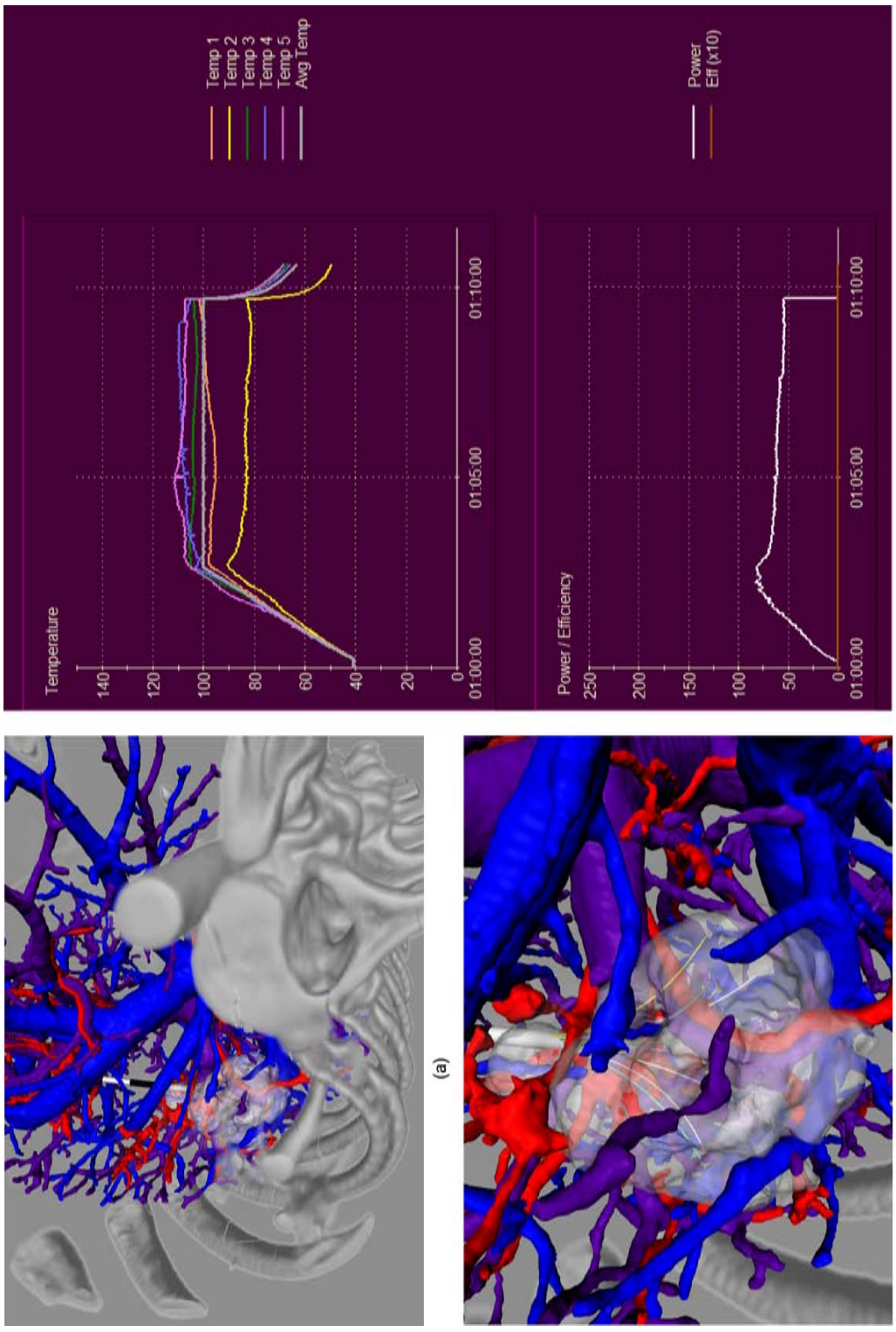

Figure 7.16: Close-ups of the virtual physiological liver and its RITA protocol: (a) shows the same virtual physiological liver as in Figure 7.15. zoomed in and (b) even more zoomed in to the coagulation directly. The needle prongs are colored to show which measured line in the RITA protocol shown in (c) belongs to which needle tip.

The virtual liver model is highly permeated with blood vessels. So the shape of the coagulation is difficult to see. Figure 7.17 therefore shows the coagulation with the needle without any surrounding vessel or bone information. We can see that the coagulation shows holes where blood vessels cooled the process enough to hinder coagulation. Again the colored needle prongs allow us to match the prongs to the measurement line in the RITA data plot. We can see a possibility for a necessary shift between the needle and the coagulation by 1 or 2 mm. This is the remaining possible registration error.

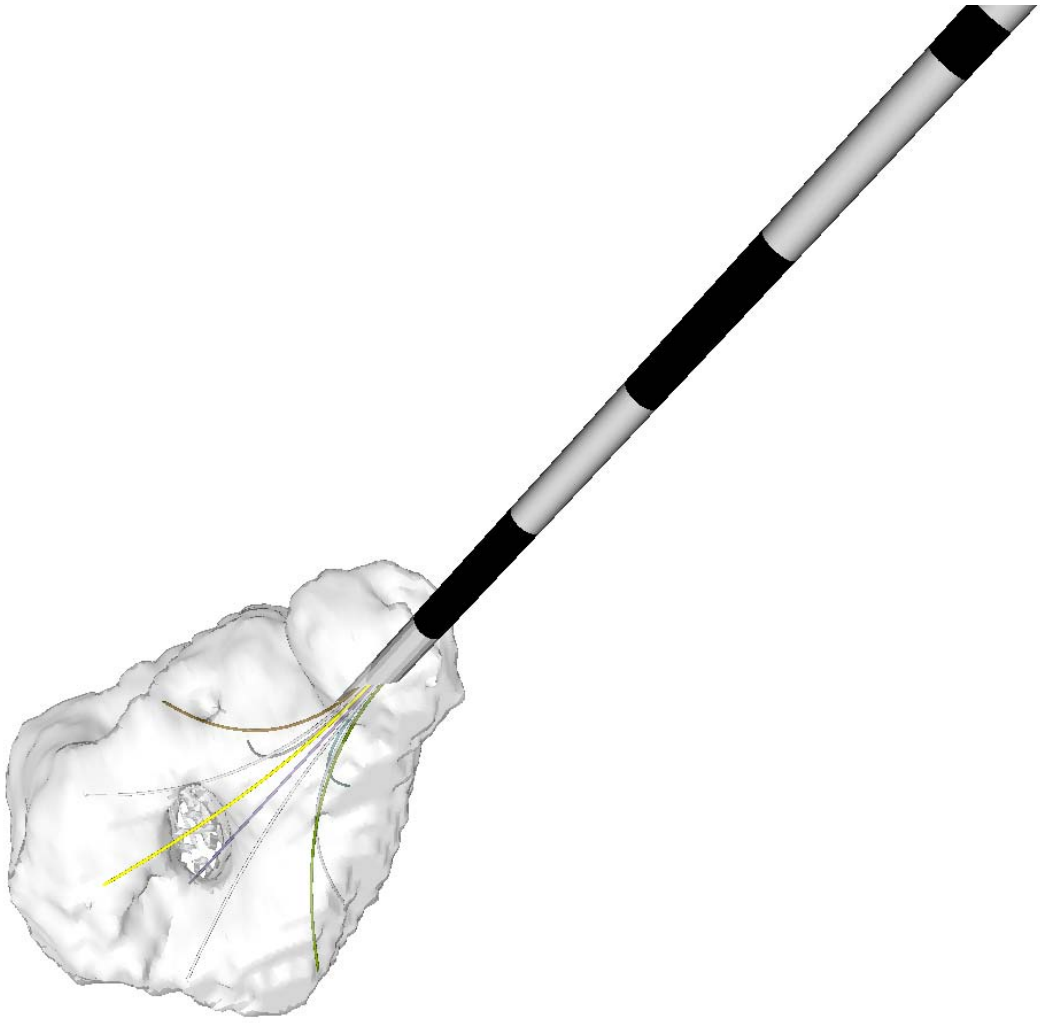

Figure 7.17: The same coagulation as in Figure 7.15 is shown here, but from a different view point and without other surrounding information such as bone structures or vessel trees. We can see holes in the coagulation where blood vessels hindered coagulation by cooling.

7.6 Simulation evaluation

By fusing all acquired data from the pig experiments visually the evaluation of simulations is now possible for the data set described above. Within the IMPPACT project two simulations were created. The simulation elaborated with the author's help was described in detail in Chapter 6. It is based on Kroeger's RFA model [80], but oriented on reflecting the experimental situation as achieved in the pig experiment of the IMPPACT project. In the following paragraphs we refer to this model as the TUG model.

Another model was created by the biomedical expert in the IMPPACT project and implemented by the numerical expert, the Oxford-Numa-Model. It shows more advanced equations and differs from the TUG model in four important details:

- Instead of implementing the electromagnetic tissue response and with it heating the tissue around the needle, direct heat sources in the form of heated dots along the needle are implemented. The dots follow the needle prongs and have approximate the needle geometry.
- Microperfusion is implemented using the model described in [113], modeling the liver as a porous sponge.
- This model handles vessels using their shape description and blood flow in the vessels along the vessel geometry, while the TUG model describes blood flow as a tissue property for the grid cells. So the Oxford-Numa-model is able to show effects along the vessel surfaces.
- The Oxford-Numa-model implements cell death as arising from heating. The cell death model was created from results from cell studies. It is integrated into the RFA model for reaching the temperature conditions which were seen to be lethal in the cell study.

The third point explained above influences the data processing and the creation of the test datasets significantly. As the TUG model does not rely on watertight surfaces of vessel trees, but works on a pixelwise classification of images it works well without a reconstruction of the vessel trees from segmented images. The Oxford-Numa-model, however, is more accurate. With its need for watertight vessel surfaces the final result of the image processing chain always involves a reconstruction into water tight surfaces with a manual meshing refinement step to ensure the vessel trees do not intersect each other.

Still the Oxford-Numa-model is advanced in its prediction. Figure 7.18 shows results of the simulation for the Oxford-Numa-model together with real images which hold all the acquired data from a pig experiment.

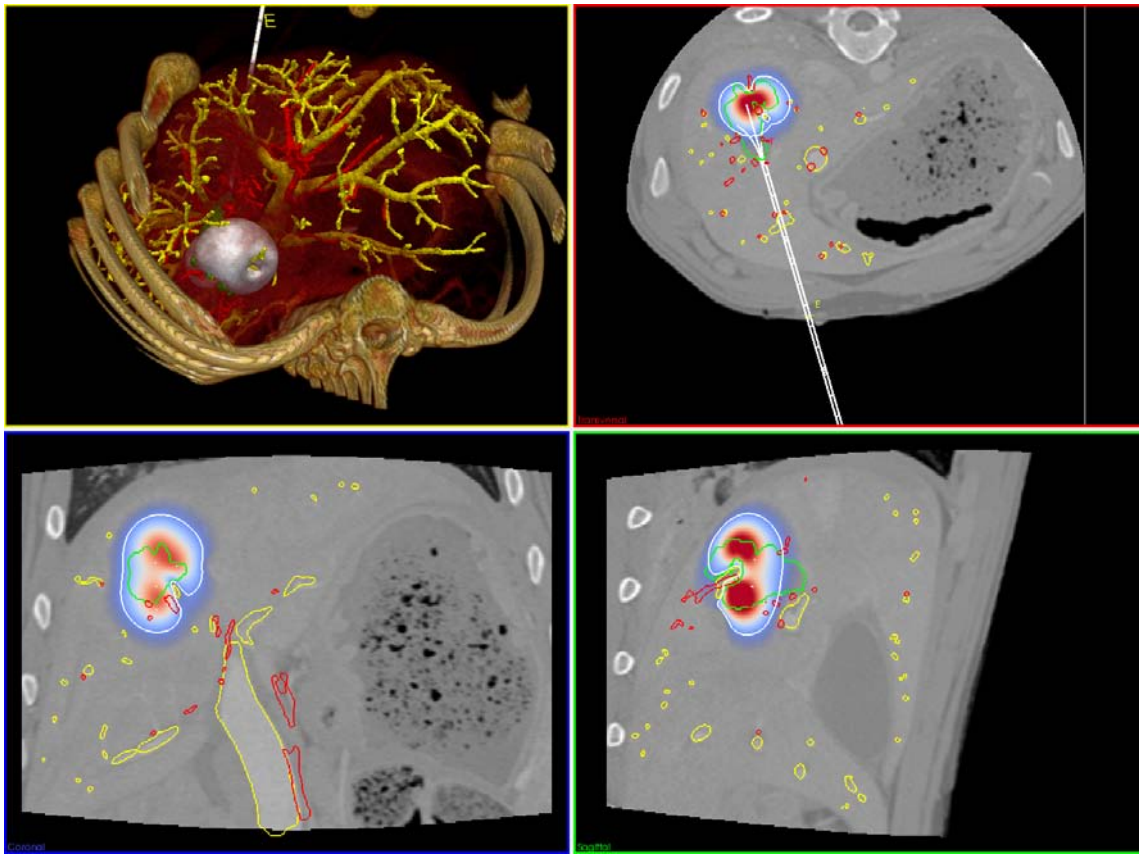

Figure 7.18: Integration of simulation and real data from the animal study. The upper left corner shows a raycasted model (using the system described in Chapter 5) the other three images show cutting planes through the datasets. The simulation is visualized in red/white/blue. The yellow and red contours show segmented surfaces of vessel trees (portal vein and artery), the white contour shows the predicted cell death area. The green contour denotes the segmentation of the imaged lesion as visible in the CT scan. The simulation was computed based on the model created by the numerics and biomedical engineering partner in the IMPPACT consortium. Visualization was performed at the Technical University Graz.

The visual comparison of the different aspects in the figure present a model prediction which shows the heat sink effect for the model prediction as well as for the real data. The prediction of cell death does not fit the area of enhancement in the CT image, which matches the results of several related publications where this difference has been seen in

reality (compare Chapter 2). A comparison of simulation and acquired CT data can now be performed visually and finally leads to an advanced simulation model. This step lies out of the scope of this thesis.

7.7 Conclusion and future work

While it is very important to model processes for predicting treatment in a validated manner, it is rarely done, because setting up the validation experiment is difficult. This is a crucial limiting factor of physiological treatment planning.

Main challenges in a validation study present the interfaces between computer science and medical sciences — so the data acquisition is oriented on a computer's needs and the presentation of the results oriented on medical experts' needs. The first data acquisition oriented on visual validation was presented here. We showed the results graphically in planar sections of the data as well as with the developed ray caster. Especially, our method of volume rendering allows us to show volumetric data and segmented surface data together. We showed a simulation overlayed with real data. This way the evaluation of the model and insights into its shortcomings can be observed and interpreted by modeling experts.

The resulting reconstructed liver is the first one oriented on model validation. It shows the liver with

- all its relevant inner structures
- in a resolution suitable for simulation computation and
- fuses all relevant data from different time steps together.

The necessary experiments were performed on 46 pigs in total, where 12 datasets have been suited for mostly error free processing by computer and allow usage of state of the art image processing tools to obtain the virtual liver model. Future challenges concern the use of the generated test data set to find a better advanced RFA model.

Chapter 8

Intervention results visible in histological examinations

Contents

Prior to the medical intervention information on patient anatomy is obtained from radiological images. On this information interventionalists base their decisions for procedures and plan the intervention. However, an image is only an image. To understand what lies behind this image, and what really happens in the body to give this image, one has to take a look at the tissue — the cells and their metabolic state.

8.1 Introduction

We are interested in dead and living cells as induced by RFA. This information can only be gained from histological images. At the same time the context of why certain cells are dead or alive relies on information which can only be achieved from radiological images. We therefore fuse information from histology with CT images on the level of fusing two reconstructed 3D volumes.

In our study, RFA was performed on domestic pigs and CT images acquired as described in Chapter 7. Following the intervention, the pigs were sacrificed and the tissues harvested. The area of interest was prepared as histological sections. For the radiological images the acquisition supports volume reconstruction implicitly. For the histological data we used semi-automatic registration techniques to reconstruct a volumetric model from the histological sections.

In the contrast enhanced CT scans taken at the end of the intervention the induced result shows up in a highlighted region (a dark spot). So the region of interest is visible in the CT scans. For data gained in histology only this region is prepared. Working on a reconstruction from the CT scans the highlighted area and the reconstructed histological volume are then fused, by finding correspondences, in natural features visible in both modalities. Figure 8.1 shows a scheme for the processing step.

The following sections deal with a multi-scale volume reconstruction of histological images and fitting CT data. This reconstruction allows fusion of both volumes in a semi-automatic approach. It consists of three main stages: first the histological data is acquired according to computer needs. In a second step a volume is reconstructed out of the set of histological sections. Finally, the reconstructed histological volume as well as the CT volume are both visualized in 3D and a semi-automatic procedure is applied to fuse both volumes.

8.2 Computer-oriented data acquisition of the liver

As explained in Chapter 7 in medical procedures and research, data are acquired according to standard procedures that are accepted as being valid and deliver the expected results. Computer vision, takes the data produced and applies algorithms to facilitate the same task that a human being could also do but with considerably more effort. This applies not only to radiological data but also to histological data. Computer vision alone often cannot accomplish the best result. So again acquisition techniques have to be oriented on the computers' needs.

At the same time, known acquisition techniques cannot be completely replaced without the need for reestablishing a user's confidence into the information acquired using a new method. For example, if a new staining was applied, the first step would be to obtain proof that the staining actually shows the classification intended, and the medical community had to be convinced of that. So our new procedure relies on established steps as far as possible. Changes are kept to a minimum to gain a wide acceptance within the community.

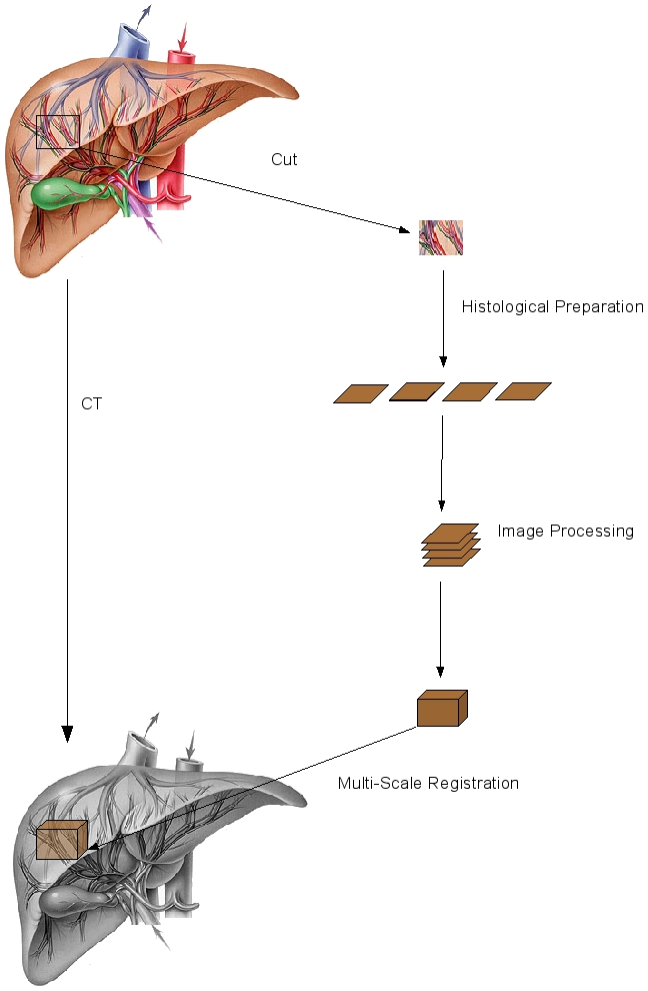

Figure 8.1: The multi-scale data fusion processing steps are shown here. A CT scan is taken of the complete liver. Then the tissue around the area of interest is cut out and microscopic sections are prepared. Using image processing the sections are stacked and the volume of the harvested tissue reconstructed in the original size. The volume can then be fused to the CT scan.

8.2.1 Imaging the liver as an organ

Imaging the vessel trees in the liver is done using contrast agents. The right imaging protocol applied in an animal study, is able to take images of all three vessel trees without breathing deformations and with high spatial resolution (0.5 mm) as shown in Chapter 7. Figure 8.2 shows a scheme for CT slices taken of the liver for example in axial orientation.

So the vessel trees can be segmented by applying computer vision algorithms, and a 3D model can be reconstructed for an animal specific 3D liver. Figure 7.9 shows a 3D

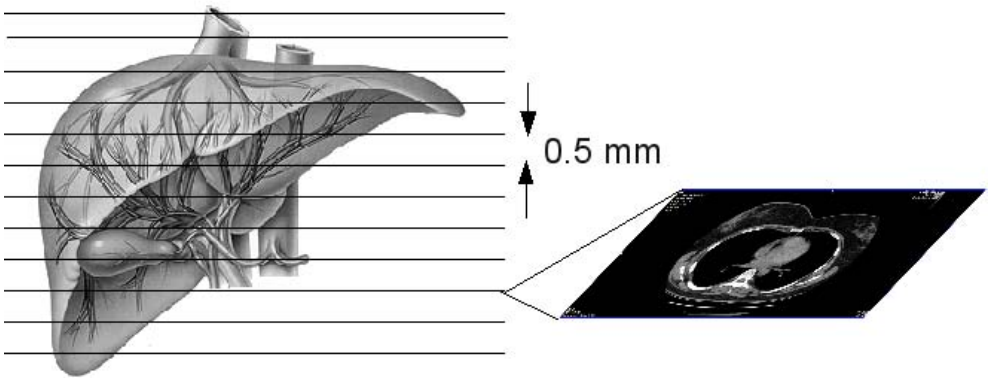

Figure 8.2: CT image acquisition: High resolution CT scans can image the liver with a slice distance of 0.5 mm

reconstructed image of a porcine liver with three segmented vessel trees. For this image the data acquisition followed the protocol described in Chapter 7 and therefore vessel trees can be seen in a high resolution.

The area of interest is visible in the CT scans. If the ablation covers up the nearby vessel structures, images from before and after the intervention can be registered to see where the vessel trees were located before the contrast agent highlighted the complete ablation. This process is shown as the left arrow in Figure 8.1. Reconstruction of the histological volume is much harder and needs many more steps to be accomplished successfully.

8.2.2 Imaging liver tissue on a microscopic scale

When viewing harvested liver tissue in a histological examination under the microscope the tissue is sliced in very thin sections down to a few micrometers in thickness. To be able to perform this slicing process, the tissue has to be prepared and fixed. The fixing procedure determines the stiffness and therefore the deformations introduced in the slicing procedure. Then the tissue can be observed under a microscope and the structures described in the previously presented scheme (Figure 1.2) are visible. Figure 8.3 shows a 3 μm section taken in the standard histological examination.

While on radiological images highlighted structures are made visible by contrast enhancement anatomical structure — for example enhanced blood vessels — on histological sections highlighting uses specific staining (colors) for different tissue characteristics. The staining gives information on the type of cell and whether the cell is dead of alive. Blood vessels appear to be holes in the sections, but not every hole is a blood vessel. A hole might also result from damage in processing the tissue sections. Arteries have thicker walls

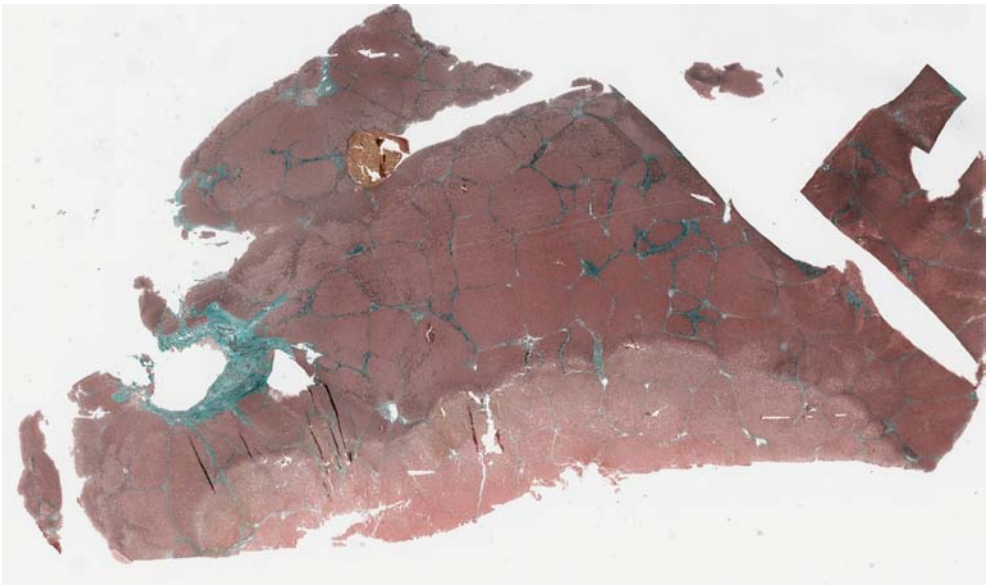

Figure 8.3: A section of liver tissue, sliced and stained according to standard procedure. The bluish tissue on the left is the surrounding of a vessel. Other holes are hard to characterize as they might also be damage from the slicing process.

than veins, and can therefore be identified more easily.

8.3 Computer-oriented acquisition of histological data

To reconstruct a histology volume, sections have to be stacked. This can be achieved by registering succeeding sections oriented on feature points visible in the sections. For automatic processing a high number of easily found feature points and small deformations is preferred.

8.3.1 Tissue fixation

The first step in tissue preparation is fixation and embedding of the harvested tissue. After stacking the sections, the reconstructed volume has to be fused with the CT scan. Again small deformations between both volumes and a high number of feature points is preferred for machine processing. The liver is therefore fixed by perfusion with Formalin to keep the organ in shape prior to excision.

We developed an optimized protocol for in situ perfusion of the liver in combination with immersions fixation, adapted from different standard protocols. Hereby the anes-

thetized, heparinised pig was flushed with 0.9% NaCl to avoid blood thrombi and the vessels were used to provide a fixative (4% formalin) to the organ (perfusion fixation). Afterwards the organ was explanted. Tissue blocks of interest (up to $3 \times 3 \times 5$ cm) were cut out of the liver tissue. These tissue blocks were stored in 4% formalin until the fixation was completed. This additional immersions fixation also made sure, that there was no change of macroscopical morphology in the tissue. A single RFA area contains 1 to 3 tissue blocks. Fixation, dehydration and embedding protocols were carefully optimized for these large tissue blocks. After dehydration the blocks were incubated in paraffin and then embedded.

8.3.2 Slicing and staining

Reconstructing a volume out of histological sections is done by stacking the sections oriented on the location of vessels as natural feature points. We are interested in the result of the intervention, which means dead and living cells in the final volume stack. Both features can be seen in histology, but not with the same staining.

We used chromotrop-anilinblue (CAB) trichrome and methylene blue for staining our sections. CAB solution stains collagen fibers, reticular fibers, and basal membranes (connective tissue as well as the vessel surface) blue. The cell nuclei are stained violet and the cytoplasm in different shades of blue. So this staining helps to distinguish between vessels or artefacts as a vessel has to have a blue area around the hole in the section. The coagulation of the surrounding area can be demonstrated in this staining but to distinguish between dead and living cells we used methylene blue. It stains only in blue, where the area of lesion is stained in a more intensive blue than around the surviving cells. So this staining gives us the information on the result of the intervention.

While one section cannot be stained in any number of colors, subsequent sections can be stained using different coloring. However, cutting the sections and staining them is a lot of manual work. So in our procedure not the whole block of tissue was processed. Instead we developed a protocol where we took three subsequent sections — two for the stainings and one as backup — and then removed a large block of 100 μm. Starting again after this block has been removed, three 2 μm sections are taken and so on. This way the tissue block is processed with less manual work. Figure 8.4 shows a scheme for taking sections in alternating distances.

According to the sampling theorem by Nyquist-Shannon the histology stack has to have at least twice the sampling rate of the CT scan so as not to lose information and be

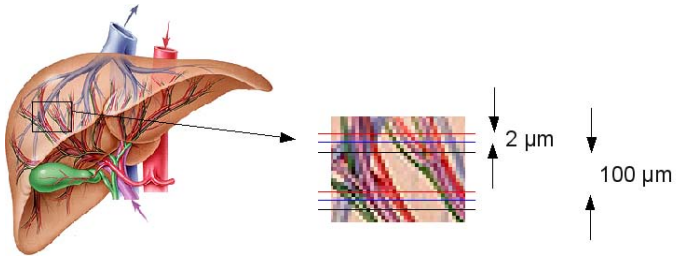

Figure 8.4: Slicing the liver for histological examination is done in a scheme of three at a time. Two sections are colored with different stainings. The third is backup in case a staining is not successful. Then a large part is skipped and the slicing applied again. More different stainings would lead to more subsequent sections acquired for every set. As long as the final cutting distance from one section to the next section of the same color does not exceed the maximum distance determined by the sampling theorem, more sections can be acquired.

able to fuse both volumes. As the CT images show a resolution of 0.5 mm = 500 μm, the tissue block must provide information with a resolution of not more than 250 μm. So our alternating slicing protocol is still oversampling the histological volume. At the same time missing out 100 μm blocks already reduces the manual work time from several months to two weeks for processing one tissue block. Image processing is easier if the tissue sections are taken closer to each other as the location of vessels (our natural feature points) is not very different in sections taken with smaller distances between them.

8.3.3 Scanning histological sections

The standard procedure for imaging histological sections relies on taking photographs through a microscope. Due to the unusual size of the carriers used in our preparation the standard medical equipment could not be used here. Unable to use a standard microscope we used an off-the-shelf digital desk scanner which provides a resolution of 4800dpi to get digital images from histology slices. The resulting images were of an approximate size of $10,000 \times 10,000$ pixels. To provide the necessary contrast for the segmentation, we use a combination of incident light and transmitted light. Even though desk scanners may provide a transmitted light source, they do not provide an option to use both transmitted light and incident light. To overcome this problem, we use a black diffuse reflector placed 15 mm from to the investigated histological section. This enabled us to use the incident light source also as a diffuse transmitted light source due to the reflector. Figure 8.5 clarifies this setup.

The differences in contrast are tremendous for CAB amd MB colored histologies com-

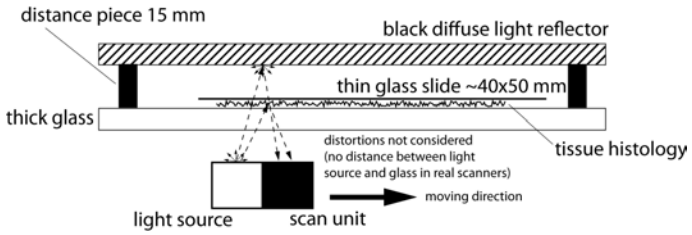

Figure 8.5: The combination of transmitted light and incident light with one light source is possible by placing a black diffuse reflector in a defined distance

pared to standard scan procedures (e.g. white direct reflector with no distance or transmitted light only). Figure 8.6 compared different standard scan methods to ours.

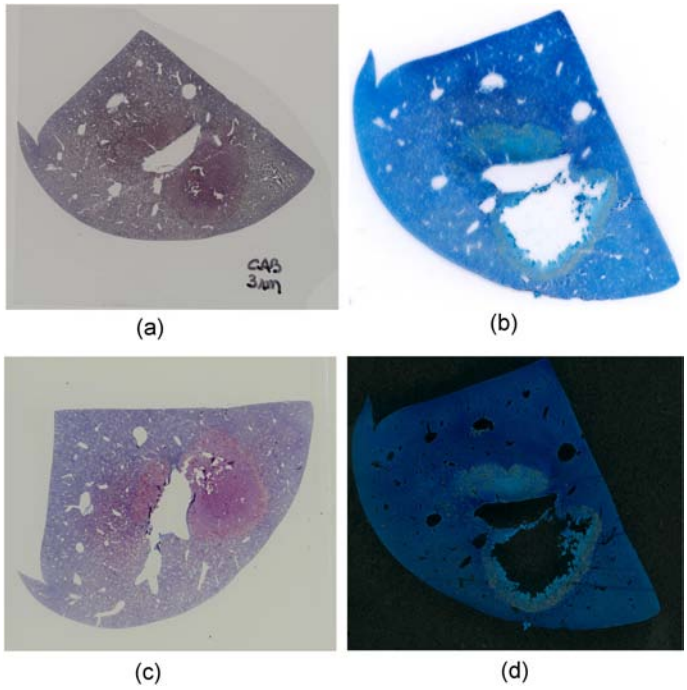

Figure 8.6: Different lighting conditions:

(a) Photograph of CAB colored section with 12 millions pixels,

(b) Scan of a MB colored section with transmitted light only,

(c) Scan of a CAB colored section with incident light only,

(d) Our method: Scan of a MB colored section with both, transmitted light and incident light.

8.4 Image processing of histological sections

With $10,000 \times 10,000$ pixels as the resolution, it is not possible to zoom in and see details inside the cell nucleus. However, the resolution gives a very good overview of the tissue at the level of multiple cells. So the lower resolution still shows all the structures necessary for judging cell death by staining. Using a higher resolution would be easily possible if the microscope could handle the large carriers. However, this demands out of core image processing and visualization techniques.

8.4.1 Non-rigid registration of sections

A complete volume is built by registering and stacking all sections acquired for one volume lesion. In the procedure, blood vessels serve as natural feature points. Histological sections are cut out of soft tissue, so the underlying transformation between the images is actually non rigid. We therefore chose control points manually and compared the result of a non-rigid registration with the unregistered stack. Figure 8.7 shows control points which were chosen manually on the surfaces of blood vessels and served as input for a 2D free form deformation algorithm.

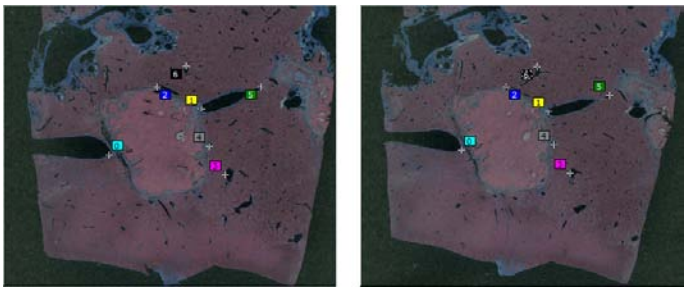

Figure 8.7: Control point assignment in two adjacent images to vessels around the lesion.

Figure 8.8 shows the result of a non-rigid deformation by free form deformation (lower part) compared to the unregistered original images (upper part). The single images in the figure show sections for a part of the stack, colored in CAB mode.

As we can see the free form deformation mainly rotates the input images. The expected overall deformation is limited to very little "stretching out the corners". So deformations inside the sections are in fact minor and are therefore not taken into account. Even a rigid registration is sufficient for a proper lesion reconstruction.

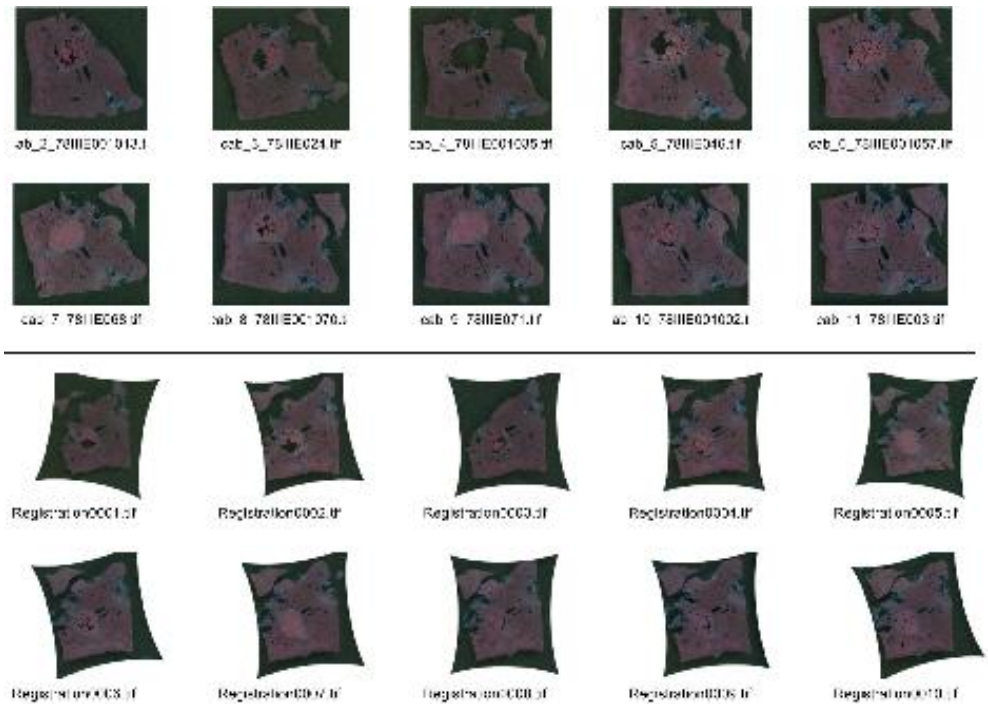

Figure 8.8: A part of a CAB colored stack of histological sections: The upper part shows unregistered images, the lower part the same sections after non-rigid registration based on manual chosen control points.

8.4.2 Combined segmentation and registration

Segmentation and registration both rely on the other algorithm's results. The segmented vessel candidates build the natural feature points for the registration algorithm. At the same time the probability of identifying a vessel candidate is higher if a neighboring section has candidates in the respective area too. We therefore developed a multi-resolution, semi-automatic, probabilistic algorithm for combined section-by-section segmentation and registration.

Formulating the joint segmentation and registration problem is computationally too demanding for the large data sets we use. The other approach is to divide the task into two independent sub-tasks: segmentation of tissue structures from 2D histology sections and registration of the 2D sections for reconstruction of the 3D model. We propose an algorithm combining ideas from both approaches: First, the histology sections are converted into feature images which describe the probability of each pixel belonging to a tissue type (Classification). Independent of that, neighboring sections are rigidly registered. Using the registration results, the probabilistic classification results are propagated to neighbor-

ing sections in order to strengthen cohesive tissue structures and eliminate noise. Those smoothened feature images are finally segmented into vessels, regions of dead and regions of living tissue by a standard level-set method. Instead of propagating the classification probability a volumetric probabilistic model could be built and then segmented using a 3D level-set. This approach would have been the preferred one for us but was computationally not feasible because of our large data set.

Although, the histology processing and image acquisition is tailored to the needs of automatic processing, neighboring sections can vary considerably in form and structure. Cutting and staining of sections is an invasive process and can result in damaged tissue. Therefore, the developed algorithm is specifically tailored to be robust against such noise. For classification of tissue types we use an unsupervised standard mixture of Gaussians (GMM) classifier which is widely applied in color image segmentation tasks. As tissue and stainings differ considerably between sets of acquired data the algorithm is furthermore adaptable to varying tissue appearances. Ultimately, manual refinement of the segmentation may be necessary.

The combined segmentation and registration algorithm is based on variations of three basic algorithms:

1. Probabilistic classification of tissue type

2. Section-by-section registration using a standard multi-resolution registration framework implemented in ITK with rigid transformations, normalized mutual information and a genetic optimization algorithm.

3. Segmentation of tissue structures is based on the classification in the current section and its neighboring sections

As the algorithm has to process large data sets (typically 200 sections of $10,000 \times 10,000$ pixel), it processes the data on two resolution levels with an almost identical work flow. The main difference is that on the low resolution level the whole sections are processed and, subsequently, regions of interest (ROI) are extracted. The full resolution sections are processed only in those ROIs to refine the results of the low resolution level. So the overall processing time per stack is kept low. Figure 8.9 shows the result of the single steps on one sample CAB section.

The next step is to fuse the pair of CAB and MB sections which belong together into one segmented section. Typically, the segmentation results are very similar for both

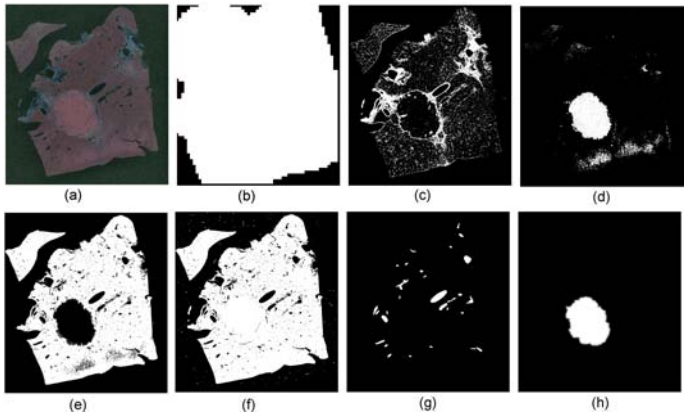

Figure 8.9: Processing of a CAB section with the implemented algorithm in the low resolution level.

(a) Low resolution CAB section,

(b) Coarse foreground mask,

(c) Connecting tissue classification (white is probability 1, black is probability 0),

(d) Dead tissue classification,

(e) Living tissue classification,

(f) Foreground classification,

(g) Vessel candidates after level set,

(h) Dead tissue after level set

sections and the fusion is trivial. In the other case, the segmentation result which fits best into the model measured as the quality of registration is retained.

The final result of the image processing consists of transformation matrices for all the images acquired from histological sections as well as segmentations (vessels and dead or living regions) as shown in Figure 8.9.

8.4.3 Reconstructing volume information from histological images

Through the image processing orientations of histological sections are determined. The image stack can now be easily transformed into a volumetric file format like Analyze 7.5 or DICOM. As our histology slicing method, explained in Section 8.3.2, generates sections with different distances to each other. So, the standard volume formats either have to deal only with a complete set of one specific staining, or else the standard format has to be extended to encompass differing distances in at least one dimension and different

stainings.

The area of interest is either segmented as well or visualized together with the model in direct volume rendering. Figure 8.10 shows an example volume reconstructed from a few histological sections and visualized using raycasting.

Figure 8.10: A small histological volume with different representations visualized using raycasting: On the left side a stack of histological sections is presented. The dark spots in the stack are holes, large blood vessels, that reach all through the block of sections. In the middle the same stack is shown, this time holes are colored and the tissue is suppressed. The large vessels are accompanied by a lot of rather small vessel candidates. The more transparent view of sections on the right side allows us to see the different appearances of cells, the lesion, inside the block.

8.5 Fusion of histological and radiological data

Fusing histological data with radiological data would allow us to draw conclusions of what is visible in the radiological image compared to the histological findings. This step has often been wished for from many sides. Still it is difficult due to the very different scales and very different acquisition techniques. Our method benefits from a 3D reconstructed histological volume which needs to be fused to a high resolution CT volume. After taking a look at the state of the art for fusion of histological images to radiological ones the benefits and drawbacks of our approach are discussed.

8.5.1 Fusing the histology stack with CT images

The stack of processed histological images holds a size optically comparable to a region in the CT scan. Moreover, the region of interest can be spotted in the CT scan as well. While

the histological volume is still distorted compared to the CT volume, both show the same natural feature points, blood vessels, which are very large on the scale of histological images and very tiny in diameter on the scale of CT images. This allows fusion of information from both images oriented on these natural feature points.

Still, the histological volume shows structures in poor quality with false positive splatter. So equivalence between structures in the histological volume and structures in the CT volume have to be found manually. If enough feature points can be identified both volumes can be registered. Figure 8.11 shows the histological volume and the CT volume side by side.

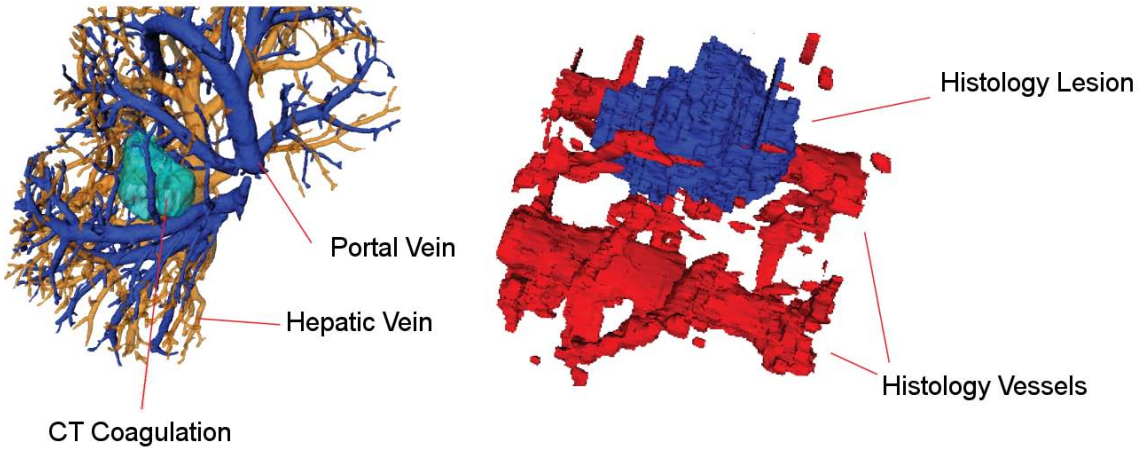

Figure 8.11: CT and histology volume side by side: while in the CT scan the vessel trees are clearly visible and can be identified the respective structure in the reconstruction from histology looks far more cluttered and distorted.

The reconstructed histological volume consists of stacked slices as they were cut from the block. Still the block was dissected from soft tissue and can be deformed in many different ways. The tissue block can be distorted in different directions, bent, or even irregularly shrunken. As the block is sliced after the deformation and the cutting process again applies further deformation structures that lie nearby in the CT volume or even on the same histological section do not necessarily have to be on the same cutting plane through the deformed volume. Figure 8.12 shows examples of possible deformations. Our example tissue block underwent a complex combination of a free-form deformation.

From an image processing point of view, fusion of both volumes demands a free-form-deformation. This optimization technique works on a high number of degrees of freedom and therefore demands a high number of feature points. Figure 8.13 shows the result of

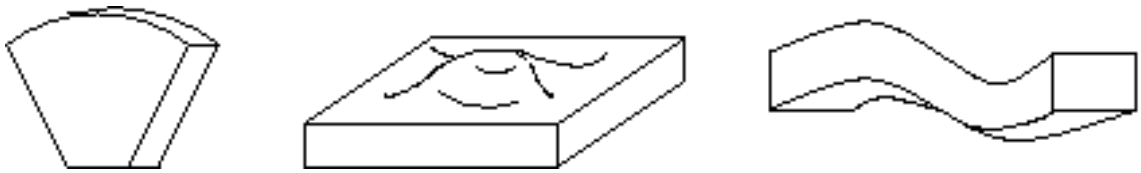

Figure 8.12: Example schematics for volume deformations: the tissue block underwent an unknown deformation before the slicing. What is sliced as parallel planes has not been parallel planes in the CT image. A free-form deformation has to be computed to undo these distortions before the reconstructed volume can be fused with the CT scan.

an attempt to use manually selected feature points and a standard automatic non-rigid registration.

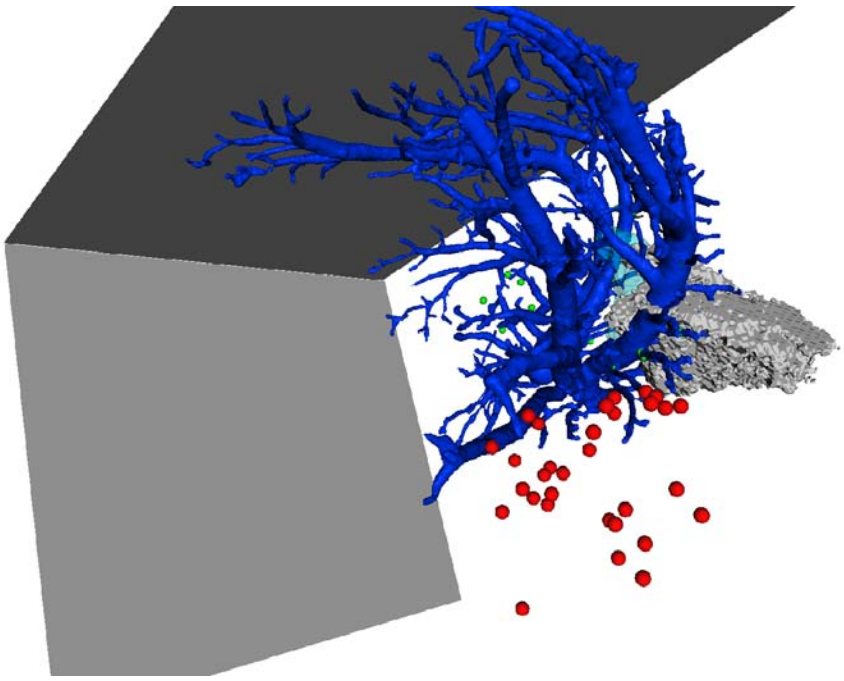

Figure 8.13: Fusion of the 3D reconstruction from histology to the CT scan: the tissue block doesn't show vessels on the outer side of the lesion. As there is no limiting point in this direction the registration algorithm pushes the lesion out of the liver tissue.

Figure 8.13 chooses feature points only on blood vessel junctions. As the processed lesion is peripheral and the applied registration method is a very general one, the algorithm optimizes fitting by unrestricted growing into the peripheral space and therefore pushes the lesion out of the liver. This can be restricted if feature points in this direction are identified and chosen. Figure 8.14 shows the result of a fusion, which also incorporated

the surface of the lesion. One can clearly see the spatial correlation for both volumes. Still the registration error is high. Furthermore, selecting feature points on the surface of the lesion renders the validation invalid, as the algorithm forcefully computes a fitting size and shape.

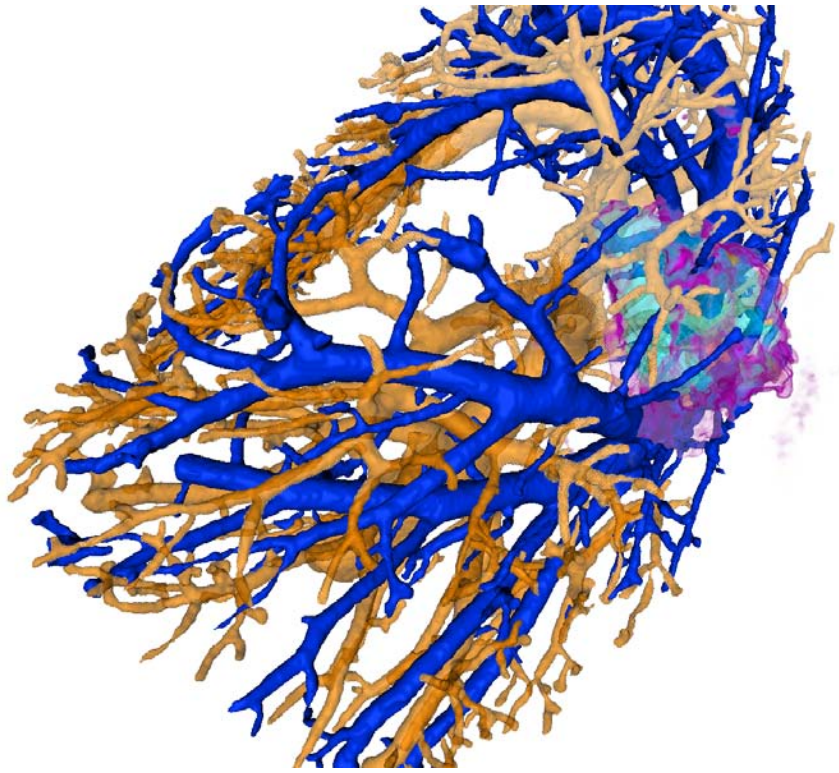

Figure 8.14: Fusion of histology and CT with control points on the lesion's surface. By putting control points into the otherwise uncovered area, the lesion can be forced to overlap. Unfortunately this is a bad validation, as the volume is distorted until an overlap is forced. No similarity, size, shape or location information can be derived from this registration.

Figure 8.15 shows the corresponding feature points that lead to this better registration. The feature points are selected around vessels to give an impression of the vessel size. Some feature points also sit on the surface of the lesion to limit the movement of this structure outside of the liver.

The source of the errors are found in both medical registration components: the corresponding feature points are chosen manually and error prone. Choosing the right points demands a skilled assistant to observe both datasets carefully and understand the corresponding structures. A large error is introduced if the wrong vessel tree junctions are

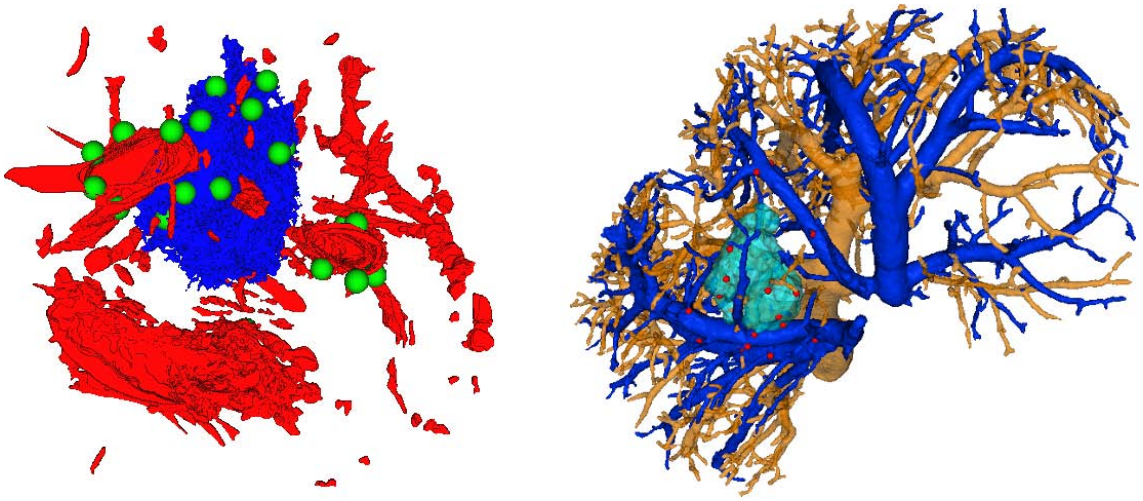

Figure 8.15: Point picking for CT and histology fusion: on the left the histology volume shows green dots where control points were chosen, the corresponding dots are red spots in the CT reconstruction on the right. Spots on the lesion surface deliver the better result, but render it invalid for validation purposes.

chosen. Choosing exactly the right position for a correspondence point is a matter of manual skills, but small deviations from the perfect placement only lead to small deviations for the result of the registration. The second error source is the automatic non-rigid deformation of the volume. Improving this step is a clear computer vision research question and left for future work.

The more interesting question is the measurement of registration quality. The information to be deduced is the correspondence for radiological images and histological appearance for the result of an RFA intervention. So this correspondence cannot be taken as a presumption — neither for the processing step, nor as validation quality measurement. The match for the secondary structure — the blood vessels and their junctions — needs to be evaluated numerically or at least has to be visually convincing. The major deficiencies in image processing for our prototype solution make this impossible right now. The other less optimal solution would be to gain a convincing impression for the lesion. This again demands a good visualization technique as the created data structure is not a native representation in any existing discipline and therefore no experts with previous experience exist to judge this result.

8.5.2 Numerical evaluation

When relying only on blood vessel junctions as control points for the registration, the achieved fusion of histology and CT lesions shows insufficient congruence. The assumption of feature points on the lesions surface rectifies these errors but is not a valid assumption, as with this correction any volume can be made to fit any other volume of the same topology. A numerical evaluation of the registration step therefore only makes sense for the case relying on blood vessel junctions. It can be achieved with different error metrics. An overview over various metrics and their respective specifics can be found in [60] and [111]. We orient our measurements on these publications and use the following metrics to describe our case:

Volume size: The size of the lesion volume.

Volumetric overlap error: The number of voxels in the intersection of both lesion volumes (CT and histology) devided by the number of voxels in the union of both volumes, subtracted from 1 and multiplied by 100. This value describes the overlap as a percentage and is 0 for a perfect match.

Relative volume difference: Difference of the CT lesion volumes to the histology lesion volume divided by the histological lesion volume. For a perfect match this number is 0.

Maximum surface distance: The border voxels of both lesion volumes (the voxels that have at least one of their 18 neighbors outside the lesion) are determined. For each voxel along one border, we look for the closest voxel along the other border. Here, unsigned Euclidean distance is used. the distances reflect real world measurements and are therefore independent of resolution differences. The maximum of the border voxel distances found is our error metric. Ideally this value is 0.

Average surface distance: The same border voxel distances are computed as for the maximum surface distance. Here the average instead of the maximum is computed. Without any distances this value is 0.

Average root mean square surface distance: For the same border voxels as above the distances are each squared, added together, and the square root taken for the sum to build the average. Here also 0 would be expected for a perfect overlap.

Tab. 8.1 shows the respective computed errors for the described metrics.

Metric	Value
Volume of CT lesion	9.2 ml
Volume of histology lesion	1.6 ml
Volumetric overlap error	85.87%
Relative volume difference	472.39%
Maximum surface difference	25.3 mm
Average surface difference	5.9 mm
Average root mean square surface difference	8.5 mm

Table 8.1: Numerical error for the fusion of CT and histological volume. The comparisons concern the segmented lesions in both modalities.

8.5.3 Expert opinion

The fusion of CT images and histological images is definitely interesting to people modeling the process. To them, what is most important is a comparison of the simulation as computed on a radiological image (as this is the prediction) to the histological image showing the result of dead and living tissue in a histological examination. However, the same should be interesting to an expert performing this treatment in clinical practice. An interview with an interventional radiologist brought new insights into the evaluation of the elaborated and presented facts. We conducted an Expert Interview with Prof. Dr. Portugaller [126]:

Question: Who would be interested in a 3D volume created from histological sections?

Answer: Radiologists are interested in the result. They would want to know about the exact extension of the necrosis zone and what the tissue looks like in close proximity to blood vessels. Usual examinations of histological sections are performed by pathologists.

Question: Would a radiologist be able to evaluate results in the prepared tissue?

Answer: Sure, after an introduction by a pathologist even looking at subsequent sections and building the volume in their own mind could be done. So the Volume of histological sections is already very interesting even without a registration to the CT image.

Question: Is the classification into dead/living tissue by coloring and also into blood vessels important?

Answer: As a radiologist has to learn the classification of tissue from a pathologist this is important. Coloring allows distinction by areas.

Question: How is navigation in this 3D data performed? Are proximity or exact distance to some feature or structure important?

Answer: Radiologists lern to construct a 3D volume from subsequent sections in their mind. This is a question of training/routine. So exact distances are not uninteresting but not enough. Navigation is performed due to structures not due to selected feature points.

Question: What would be most important to be seen in a variant that is correctly registered to the CT scan?

Answer: Most interesting would be the extension of the necrosis zone in relation to surrounding structures. Does it reach the vessels completely or are cells surviving? Does it reflect the area visible in a contrast enhanced CT scan? What do the borders look like?

So pathologists usually look at single sections. We invented a new data format — the 3D histology — which could be used later on by pathologists and which the interested radiologist is able to handle with an introduction. It is still a new data format which is not normally in use. So there is no expert available for processing this type of data specifically.

As navigation aims at finding the location of interesting structures or areas relative to another structure or area, the exact distance between two such features is not sufficient information. To a radiologist it is rather interesting, if the zone of dead tissue reaches the blood vessel or not. This is also visible in the 3D histology data without fusion to a CT. So the intermediate step is already helpful. Still the question for equivalence between CT lesion and histological lesion cannot be answered due to bad registration. Existing related work and future work will have to look into this information.

8.6 Conclusions

In our method, we describe a solution for fusing histological data with CT scans. Our method is able to deal with soft tissue organs of arbitrary size. The only requirement

is that the area of interest is visible in the CT scan and surrounded by structures that serve as natural feature points. This would also be applicable for example in tumor examinations. The histological sections used for the visualization are fixed and acquired in biological standard procedures which are specifically oriented on image processing needs. As every single step in the preparation of the medical data consists of standard laboratory techniques medical research can interpret this kind of data, if the right visualization and information presentation is chosen. This is a computer graphics research topic to be examined in future.

Registration errors are high — so we have a proof of principle, but not a working solution for everyday. Image processing needs to be improved and specific adaptions found for this problem at hand.

With our method we are able to compare simulation results computed on radiological images with intervention results visible in histological examinations. Our image processing methods deviate only minimally from the state of the art. So the result still suffers from a high registration error. The output is therefore not suitable enough to be used in a validation experiment. The challenges here are multi-factorial: changing positions of the liver in the abdomen, changing positions of the liver segments to each other, and tissue distortion in the fixation hinder a successful approach. Though computer oriented data acquisition methods are very successful they need to be further explored. Moreover, advanced image processing solutions need to be found to cope with the still existing large registration errors.

Chapter 9

Summary, Conclusion and future work

Contents

The research topic discussed in this thesis is very relevant as it tackles a medical challenge and is directly applicable in real life. At the same time, this makes the solution highly interdisciplinary in nature and demands progress in many different disciplines. We present concepts and tools to attack the question of building a validated prediction application for the RFA intervention.

9.1 Summary

First we examined how to form an interdisciplinary approach fitting the interdisciplinary challenge is best laid out. We saw, that the necessarily participating academic disciplines conduct their research according to very different methodologies and with very different criteria for good research. A systematical examination showed especially wide discrepancies between medical and engineering disciplines. Large differences in terminology but also in methodology are best bridged with visual presentation of the respective research results.

After identifying the necessary research disciplines for building a validated RFA prediction, the Imppact project was created to facilitate strong collaboration among experts

from every discipline. For every participant the challenges and the novelty of the expected results were identified and a way to work together for the interdisciplinary goal was described. A special emphasis here lay on the described experimental cycle. Data was acquired, processed, for prediction as well as visualization purposes. From watching differences in results between the prediction and the real intervention result adjustments to the prediction had to be elaborated.

The validation paradigm behind the creation of the intervention result prediction relies on visualization of results. Firstly, this is a common language understood by all participating disciplines. Secondly, deviations in prediction results and real outcome of the procedure can be discussed easily when they are visualized. This way, an understanding for missing information or wrong assumptions can be found by interpreting the nature of the deviation. We attacked the problem of validation through visualization by building a research tool which allows visualization of multi-* datasets at interactive frame rates.

A look into existing prediction models shows the dilemma of an engineering approach trying to cope with a medical topic: the complete physiology is far too complex to be understood in every detail and a living organism cannot be assembled from parts. An overview from knowledge of the RFA procedure from an engineering perspective and the respective deficiencies explains why a validated prediction has to be found empirically and oriented on the phenomena to predict — not on the details leading to the overall phenomena. We created a respective prediction application for the RFA device used later in our animal study. Applying this prediction to a common, though strongly simplified, situation shows how a small deviation from an optimum needle placement leads to a potentially non-optimum ablation.

Taking a look at the image acquisition of radiological images, we easily found why images acquired in clinical practice are not suitable for a validation experiment. Too many overlaying effects are induced in the same location. By sorting the necessary and important parts of the intervention from the ones hindering insight we defined a protocol for an animal study, which performs a tailored version of the intervention. Image acquisition in this procedure is oriented on computer needs and therefore delivers the best possible results. Errors from computer processing of acquired data are suppressed as far as possible. The resulting virtual model is suited as a reference model — an intervention specific virtual organ suited for solving prediction computations in a validation study.

Finally, the result of the intervention cannot be reliably imaged radiologically. To understand which tissue region is dead, which one is still alive, and possibly how these

regions evolve over time we have to take a look at histological examinations. Since the most interesting aspects of our study are size, shape, and location of the generated necrosis zone, we reconstructed a fixed tissue block from histological sections cut out of the tissue at this position. Ideally the block has to be fused back with the acquired radiological image, as the computation prediction of the intervention result can only be achieved from radiological images. This has been tried many times in the biomedical engineering community. Our method allows a manual fusion step, but registration errors are high. Suitability as a tool for validation is therefore questionable. A weaker validation which can easily be achieved is the prediction of the coagulated area which does not take up the contrast agent in an image following the intervention. This is not necessarily the area where cell death is ensured, but it is derived from the same image and the same imaging scale, removing the difficult registration procedures from the validation step.

9.2 Contributions of the thesis

The main contribution of the thesis is judged by comparing the research results with the hypothesis defined in the introduction:

Hypothesis: *For a physiological intervention, such as RFA in the liver, where the result cannot be imaged or assembled from complete knowledge of single effects, the result can be predicted and the prediction validated by visually comparing the computational prediction with findings in an animal study.*

The tools created in the context of this thesis show for every necessary step in the validation pipeline a first step implementation. So the overall approach to the research topic is successful. Finding the correct simulation model lies out of the scope of this thesis and remains unsolved. In detail the following part contributions have been elaborated:

An interdisciplinary collaboration: the project Imppact provided the necessary cooperation to solve the research tasks in a suitable interdisciplinary collaboration environment.

The multi-* raycaster: our implementation of a realtime volume rendering tool allows combination of multiple volumes and polygons in an encompassing approach. We are able to perform CSG operations on volumes, which builds a strong backbone for all visualization tasks.

RFA solver for the RITA system: the solver implemented at TU Graz extends an existing model for RFA prediction by all terms necessary to deal with the RITA RFA system. Our application shows tolerance to deficiencies in needle placement.

Computer oriented radiological data acquisition: our imaging protocol delivers results suitable for computation in a validation study by avoiding computer vision difficulties and errors. We are able to reconstruct a virtual organ suitable for validation of the intervention prediction. The acquisition protocol allows handling data with minimal user interaction and therefore enables us to process a statistically relevant amount of data.

3D reconstruction from histologies: again by adapting the data acquisition to computer needs as far as possible and applying reliable computer vision techniques, we are able to reconstruct a 3D volume of a tissue block from histological sections.

We therefore conclude, that validation by a visual comparison of computer simulation results with the real intervention is possible. The respectively created tools allow researchers to adjust their model prediction phenomenologically to findings in reality without justification for every detail in the far too complex medical situation.

9.3 Direction for future work

The work presented here opens up a lot of possibilities for future research questions. Of course, the overall research goal — finding a validated model to predict the outcome of RFA intervention — will evolve further.

9.3.1 Future work in IMPPACT

The project IMPPACT as described in Chapter 4 will now apply the created validation chain to validate the currently best fitting RFA model. With our imaging protocol we are able to construct a statistically relevant amount of test data sets. So the project will go on refining the model and every step will be tested to comply with the validation data set. The comparison to histological data will be refined further and allow testing computations on cell death with the validation chain.

The validation will be extended towards patients. Here normal CT data, acquired in clinical practice, and therefore with more artifacts, less contrast, less resolution and more deformations build the basis for computations. The treatment result can only be

compared to MRI data acquired the day after the procedure. Still this data will allow us to perform the step from pig to man.

Furthermore, the validated model will be incorporated into the IPS (intervention planning system). The system will allow radiologists to load preinterventional CT scans from patients, to process these images, and then to plan the needle placement. The computed simulation will predict the RFA procedure based on the eleborated planned model. So for the first time RFA will be patient specific plannable.

The IPS will be acompanied by an augmented reality simulator. Here training on handling the IPS and performig the fitting RFA procedure will be supported. The radiologist will therefore have a tool to train handling the IPS and work on treatment planning before actually performing this step in a real life procedure.

9.3.2 Extending volume visualization

Besides the overall progress in the project the single tools in the validation tool chain could also be enhanced. The aim of the created tool is to support understanding of the prediction function by visual evaluation and adapting it to meet the real function. Suitable visualization techniques based on the created multi-* raycaster are therefore the next goal in extending the developed tool chain.

The simulation functions in our context are not digital (is the tissue coagulated or not) but rather showing temperature on a continuous analog scale, or probabilities. So we aim at a visualization for overlapping fuzzy zones, which should never give the impression of providing a clear boundary. Any geometric surface presentation that allows us to zoom to a point where the surface is visible as a surface, gives the wrong impression.

For the envisioned multiple overlapping zones in the medical procedure or simulation, it is most important to identify clearly which interpretation belongs to which overlapping zone. Also highly important are the visualizing proximities between structures (for example blood vessels) as these proximities are essential for finding the correct simulation equations.

If the designed modeling function is not a constant or linear function, the user is most likely not aware of the functions behavior at a large distance from the point of interest. In other words, computed values for example for temperature might induce a computational decision for a probability of coagulation in close proximity, but they might also raise the temperature of neighboring tissue at a distance. So the visualization needs to address both — results of the simulation at a close distance to an induced event but also at greater

distances.

Furthermore, questions on the user interface and HCI have to be addressed. An application like the validation application also, of course, presents the typical problems of how to lead the users attention to the important factors. Zooming in and out of visualized data will be a research issue in the same way as navigation in space and time. The visualized process is an ultra-scale computation in space and time, with data acquired in clinical practice in 3D space at multiple times as well. The ultra-scale step in space dimensions concerns navigation and visualization of probabilities derived from a large set of different characteristic parameters. Multi-scale steps in time lead to event driven visualizations which attach one discontinuity to another. Even a parallel presentation of more than one view in different windows would be possible and lead to further requirements on the software system as well as on the perception and interaction levels.

9.3.3 Macroscopic modeling of the RFA process

Establishing the next, better prediction model by using the tool chain suggests diving into physiological modeling. Starting with a macroscopic approach oriented on phenomena, the importance and tolerance for accuracy in macroscopic properties have to be determined in particular. Those include physical properties such as blood pressure and temperature, but also tissue properties such as the degree of cirrhosis. The aim of this step is to identify the accuracy of measurement required for the correct prediction of treatment results.

In the next step, results of combinations of different aspects from the first two steps have to be visualized together with corresponding probabilities to gain a better understanding of tolerable cumulative errors. At the same time, visualization of variations in the models parameters in the ablation algorithm should be researched. By providing visual comparison of the results from RFA simulations with varying timing and power, one can better investigate the impact of different parameters on the ablation outcome.

Curve fitting for resulting coagulations and necrosis is the next approach to develop empirical models for different ablations in identical tissue properties as well as across tissue properties. In this step models are developed empirically by approximation of measurement results with formulas without biophysical background, as the background lies on the microscopic scale.

9.3.4 Validation against histological data

So far the fusion of the reconstructed histological volume with the CT volume is difficult and results in a heavy registration error. This should be tackled on both image processing steps in the procedure. First a better alignment of the respective single sections gave a better impression of the resulting 3D reconstruction. A better automatic adaption to different staining results furthermore gave more tolerance to this step and led to easier support laboratory work. Finally, a filter to remove more of the false positive blood vessels gave a better impression of the reconstructed histology volume.

To make the fusion step easier more constraints between both volumes need to be found. For example, fitting blood vessels should have a similar diameter in both volumes. Junction points should be a similar distance apart from each other, and, last but not least, incorporating physical properties into the deformation algorithm possibly gives a better chance on solving this fusion task. We are looking at a very detailed and specifically optimized solution for this fusion challenge. This is often the case when dealing with medical computer vision and presents a research challenge to a computer vision expert.

The work presented in this thesis lays down a strong framework for a lot of future research in all participating research disciplines. While a lot of work can be invested into developing better computer vision algorithms and better biomedical equations, the interdisciplinary approach also holds open opportunities for purely medical research as well as mathematical or computer graphics challenges. Even meeting only a subset of them is a challenge not easily met.

Appendix A

Acronyms and Symbols

List of Acronyms

2D	2 dimensional
3D	3 dimensional
CAB	Chromotrop Anilinblue
CL	Cirrhotic liver
CSG	Constructive solid geometry
CUDA	Compute unified device architecture
CT	Computed tomography
DICOM	Digital imaging and communications in medicine
DNA	Deoxyribonucleic acid
DS	Degree of vascualar stasis
DVR	Direct volume rendering
EU	European Union
FEM	Finite element method
GMM	Mixture of Gaussians
GPU	Graphics processing unit
HCC	Hepatocellular carcinoma
IMPPACT	Image-Based Multiscale Physiological Planning for Ablation Cancer Treatment
IPS	Intervention planing system
ISBN	International Standard Book Number
ITK	Segmentation and registration toolkit
HCI	Human computer interaction

MB	Methylene blue
MH	Metastasis with high perfusion
MITK	Medical imaging interaction toolkit
ML	Metastasis with low perfusion
MR	Magnetic resonance
MRI	Magnetic resonance imaging
PDE	Partial differential equation
RAM	Randam access memory
RF	Radiofrequency
RFA	Radiofrequency ablation
RGB	Red green blue
RNA	Ribonucleic acid
ROI	Region of interest
SIMD	Single instruction multiple data
TU	technical University
US	United States
USA	United States of America
VPH	Virtual Physiological Human

List of Symbols

$O(n)$	order of (O-notation)
$\mathbb{Z}$	integer
$>>$	much larger than
∂	partial derivation
∂_t	partial derivation with respect to t
∇	Nabla operator

Bibliography

[1] abcam (2010). Perfusion fixation protocol - PERFUSION FIXATION. Technical report, Abcam.

[2] Ahmed, M. and Goldberg, S. N. (2005). Image-Guided tumor ablation: Basic science. In vanSonnenberg, E., McMullen, W., and Solbiati, L., editors, *Tumor Ablation: Principles and Practice*, pages 23–40. Springer Science+Business Media, Inc.

[3] Aila, T., Miettinen, V., and Nordlund, P. (2003). Delay streams for graphics hardware. *ACM Transactions on Graphics*, 22(3):792–800.

[4] Alhonnoro, T., Pollari, M., Lilja, M., Flanagan, R., Kainz, B., Muehl, J., Mayrhauser, U., Portugaller, H., Stiegler, P., and Tscheliessnigg, K. (2010). Vessel segmentation for ablation treatment planning and simulation. In *Medical Image Computing and Computer-Assisted Intervention*, LNCS, page accepted. Springer Verlag.

[5] Altrogge, I., KrÃ¶ger, T., Preusser, T., BÃ¼skens, C., Pereira, P. L., Schmidt, D., Weihusen, A., and Peitgen, H. O. (2006). Towards optimization of probe placement for radio-frequency ablation. In *Medical Image Computing and Computer-Assisted Intervention*, volume 4190 of *LNCS*, pages 486–493, CeVis-Center for Complex Systems and Visualization, University of Bremen, Germany. Springer Verlag.

[6] AngioDynamics (2010a). *RFA for Liver Tumor Protocol, Abbreviated from the complete instructions for use for the RITA System User's Guide*. AngioDynamics, 150-102874 rev 02 edition.

[7] AngioDynamics (2010b). *RITA 1500X User's guide and service manual*. AngioDynamics, 160-103990 rev. 03 edition.

[8] AngioDynamics (2010c). *Starburst XL Promotional Literature*. AngioDynamics.

[9] Ansorge, R. E., Sawiak, S. J., and Williams, G. B. (2009). Exceptionally fast non-linear 3D image registration using GPUs. In *2009 IEEE Nuclear Science Symposium Conference Record (NSS/MIC)*, pages 4088–4094, Orlando, FL, USA.

[10] Arkin, H., Xu, L. X., and Holmes, K. R. (1994). Recent developments in modeling heat transfer in blood perfused tissues. *Biomedical Engineering, IEEE Transactions on*, 41(2):97–107.

[11] Arrhenius, S. (1889). Ueber die reaktionsgeschwindigkeit bei der inversion von rohrzucker durch saeuren. *Zeitschrift fÃ¼r Physikalische Chemie*, 4:226–248.

[12] Auer, M., Regitnig, P., and Holzapfel, G. (2005). An automatic nonrigid registration for stained histological sections. *IEEE Transactions on Image Processing*, 14(4):475–486.

[13] Avila, R. S., Sobierajski, L. M., and Kaufman, A. E. (1992). Towards a comprehensive volume visualization system. In *Proc. IEEE Visualization '92*, pages 13–20, Boston, Massachusetts.

[14] Baek, S., Wells, P. B., Rajagopal, K. R., and Humphrey, J. D. (2005). Heat-induced changes in the finite strain viscoelastic behavioir of a collaagenous tissue. *Journal of Biomechanical Engineering*, 127(4):580–586. PMID: 16121527.

[15] Bangerth, W., Hartmann, R., and Kanschat, G. (2007). deal.II: a general-purpose object-oriented finite element library. *ACM Trans. Math. Softw.*, 33(4):24.

[16] Barr, A. H. (1984). Global and local deformations of solid primitives. *ACM SIGGRAPH Computer Graphics*, 18(3):21–30.

[17] Bauer, C., Pock, T., Sorantin, E., Bischof, H., and Beichel, R. (2010). Segmentation of interwoven 3d tubular tree structures utilizing shape priors and graph cuts. *Medical Image Analysis*.

[18] Bavoil, L., Callahan, S. P., Lefohn, A., Comba, J. L. D., and Silva, C. T. (2007). Multi-fragment effects on the GPU using the k-buffer. In *Proc. ACM symposium on interactive 3D graphics and games*, pages 97–104.

[19] Bavoil, L. and Myers, K. (2008). Order independent transparency with dual depth peeling. Tech. rep., NVIDIA.

[20] Beers, B. E. V., Leconte, I., Materne, R., Smith, A. M., Jamart, J., and Horsmans, Y. (2001). Hepatic perfusion parameters in chronic liver disease: dynamic CT measurements correlated with disease severity. *AJR. American Journal of Roentgenology*, 176(3):667–673. PMID: 11222202.

[21] Berber, E., Herceg, N. L., Casto, K. J., and Siperstein, A. E. (2004). Laparoscopic radiofrequency ablation of hepatic tumors: Prospective clinical evaluation of ablation size comparing two treatment algorithms. *Surgical Endoscopy*, 18(3):390–396.

[22] Bhattacharya, A. and Mahajan, R. L. (2003). Temperature dependence of thermal conductivity of biological tissues. *Physiological Measurement*, 24(3):769–783.

[23] Bischof, H. P. D. (2010). Forschungsbeschreibung computer vision.

[24] Borland, D., Clarke, J., Fielding, J., and Taylor, R. (2006). Volumetric depth peeling for medical image display. In *Proc. of SPIE Visualization and Data Analysis*, pages 1–11.

[25] Bowen, R. (2006). Hepatic histology: The acinus. In *Pathophysiology of the Digestive System*. Colorado State University.

[26] Brace, C. L. (2008). Temperature-dependent dielectric properties of liver tissue measured during thermal ablation: Toward an improved numerical model. In *Engineering in Medicine and Biology Society, 2008. EMBS 2008. 30th Annual International Conference of the IEEE*, pages 230–233.

[27] Braumann, U., Kuska, J., Einenkel, J., Horn, L., LÃ¶ffler, M., and HÃ¶ckel, M. (2005). Three-dimensional reconstruction and quantification of cervical carcinoma invasion fronts from histological serial sections. *IEEE Transactions on Medical Imaging*, 24(10):1286–1307. PMID: 16229416.

[28] Brecheisen, R., Platel, B., Vilanova, A., and ter Haar Romenij, B. (2008). Flexible GPU-based multi-volume ray-casting. In *Proc. Vision, Modelling and Visualization*, pages 1–6.

[29] Breen, M. S., Breen, M., Butts, K., Chen, L., Saidel, G. M., and Wilson, D. L. (2007). MRI-guided thermal ablation therapy: Model and parameter estimates to predict cell death from MR thermometry images. *Annals of Biomedical Engineering*, 35(8):1391–1403.

[30] Breen, M. S., Lancaster, T. L., and Wilson, D. L. (2005). Correcting spatial distortion in histological images. *Computerized Medical Imaging and Graphics: The Official Journal of the Computerized Medical Imaging Society*, 29(6):405–417. PMID: 16006097.

[31] Breen, M. S. and Wilson, D. L. (2003). Three-dimensional comparison of interventional MR radiofrequency ablation images with tissue response. In *MICCAI 2003, LNCS 2879*, pages 24–31. Springer-Verlag Berlin Heidelberg 2003.

[32] Bricault, I., Kikinis, R., Morrison, P. R., vanSonnenberg, E., Tuncali, K., and Silverman, S. G. (2006). Liver metastases: 3D shape-based analysis of CT scans for detection of local recurrence after radiofrequency ablation. *Radiology*, 241(1):243–250.

[33] Bricault, I., Kikinis, R., vanSonnenberg, E., Tuncali, K., and Silverman, S. G. (2004). 3D analysis of Radiofrequency-Ablated tumors in liver: A Computer-Aided diagnosis tool for early detection of local recurrences. In *MICCAI 2004, LNCS 3217*, pages 1042–1043. Springer-Verlag Berlin Heidelberg.

[34] Brieger, J., Pereira, P. . L., TrÃ$\frac{1}{4}$benbach, J., Schenk, M., KrÃ¶ber, S., Schmidt, D., Aube, C., Claussen, C. D., and Schick, F. (2003). In vivo efficiency of four commercial monopolar radiofrequency ablation systems: a comparative experimental study in pig liver. *Invest Radiol*, 38(10):609–616.

[35] Brown, L. G. (1992). A survey of image registration techniques. *ACM Comput. Surv.*, 24(4):325–376.

[36] Butz, T., Warfield, S. K., Tuncali, K., Silverman, S. G., van Sonnenberg, E., Jolesz, F. A., and Kikinis, R. (2000). Pre- and intra-operative planning and simulation of percutaneous tumor ablation. In *MICCAI '00: Proceedings of the Third International Conference on Medical Image Computing and Computer-Assisted Intervention*, pages 317–326, London, UK. Springer-Verlag.

[37] Callahan, S. P. and Comba, J. L. D. (2005). Hardware-assisted visibility sorting for unstructured volume rendering. *IEEE Transactions on Visualization and Computer Graphics*, 11(3):285–295.

[38] Carlis, J. V. (2002). Pitfalls and paths to success in interdisciplinary scientific database research. *IEEE Engineering in Medicine and Biology Magazine: The Quarterly Magazine of the Engineering in Medicine & Biology Society*, 21(6):117–122. PMID: 12613220.

[39] Carpenter, L. (1984). The A-buffer, an antialiased hidden surface method. *ACM SIGGRAPH Comput. Graph.*, 18(3):103–108.

[40] Carr, N., Mech, R., and Miller, G. (2008). Coherent layer peeling for transparent high-depth-complexity scenes. In *Proc. SIGGRAPH/EUROGRAPHICS symposium on graphics hardware*, pages 33–40.

[41] Cassot, F., Lauwers, F., Fouard, C., Prohaska, S., and Lauwers-Cances, V. (2006). A novel three-dimensional computer-assisted method for a quantitative study of microvascular networks of the human cerebral cortex. *Microcirculation (New York, N.Y.: 1994)*, 13(1):1–18. PMID: 16393942.

[42] Chen, C. R., Miga, M. I., and Galloway, R. L. (2006). Optimizing needle placement in treatment planning of radiofrequency ablation. In Cleary, K. R. and Galloway, R. L. J., editors, *Visualization, Image-Guided Procedures, and Display*, volume 6141 of *Presented at the Society of Photo-Optical Instrumentation Engineers (SPIE) Conference*, pages 632–638.

[43] Chen, X., Barkauskas, K. J., Nour, S. G., Duerk, J. L., Abdul-Karim, F. W., and Saidel, G. M. (2007). Magnetic resonance imaging and model prediction for thermal ablation of tissue. *Journal of Magnetic Resonance Imaging*, 26(1):123–132.

[44] Consiglieri, L., Santos, I., and Haemmerich, D. (2003). Theoretical analysis of the heat convection coefficient in large vessels and the significance for thermal ablative therapies. *Physics in Medicine and Biology*, 48(24):4125–4134.

[45] Coquillart, S. (1990). Extended free-form deformation: a sculpturing tool for 3D geometric modeling. In *Proceedings of the 17th annual conference on Computer graphics and interactive techniques - SIGGRAPH '90*, pages 187–196, Dallas, TX, USA.

[46] Cosman, E. R. J. and Cosman, E. R. S. (2005). Electric and thermal field effects in tissue around radiofrequency electrodes. *Pain Medicine*, 6(6):405–424.

[47] de Ryk, J., Weydert, J., Christensen, G., Thiesse, J., Namati, E., Reinhardt, J., Hoffman, E., and McLennan, G. (2007). Three-dimensional histopathology of lung cancer with multimodality image registration. In Pluim, J. P. W. and Reinhardt, J. M., editors, *Medical Imaging 2007: Image Processing*, volume 6512, pages 65122F–8, San Diego, CA, USA. SPIE.

[48] Dercksen, V. J., Bruess, C., Stalling, D., Gubatz, S., Seiffert, U., and Hege, H. (2007). Towards automatic generation of 3D models of biological objects based on serial sections. In *Visualization in Medicine and Life Sciences*, volume I of *Mathematics and Visualization*, pages 3–25. Springer Berlin Heidelberg.

[49] dos Santos, I., Haemmerich, D., da Silva Pinheiro, C., and da Rocha, A. F. (2008). Ef-

fect of variable heat transfer coefficient on tissue temperature next to a large vessel during radiofrequency tumor ablation. *BioMedical Engineering OnLine*, 7:21. PMC2500024.

[50] Doyle, S., Rodriguez, C., Madabhushi, A., Tomaszeweski, J., and Feldman, M. (2006). Detecting prostatic adenocarcinoma from digitized histology using a multi-scale hierarchical classification approach. *Conference Proceedings: ... Annual International Conference of the IEEE Engineering in Medicine and Biology Society. IEEE Engineering in Medicine and Biology Society. Conference*, 1:4759–4762. PMID: 17947116.

[51] Duck, F. A. (1990). *Physical Properties of Tissues: A Comprehensive Reference Book*. Academic Pr.

[52] Ehrhardt, J., Schmidt-Richberg, A., and Handels, H. (2007). A variational approach for combined segmentation and estimation of respiratory motion in temporal image sequences. In *2007 IEEE 11th International Conference on Computer Vision*, pages 1–7, Rio de Janeiro, Brazil.

[53] Everitt, C. (2001). Interactive order-independent transparency. Tech. rep., NVIDIA.

[54] Fiume, E., Fournier, A., and Rudolph, L. (1983). A parallel scan conversion algorithm with anti-aliasing for a general-purpose ultracomputer. In *ACM SIGGRAPH Comp. Graph.*, pages 141–150.

[55] Frich, L. (2006). Non-invasive thermometry for monitoring hepatic radiofrequency ablation. *Minim Invasive Ther Allied Technol*, 15(1):18–25.

[56] Frich, L., BjÃ¸rnerud, A., Fossheim, S., Tillung, T., and Gladhaug, I. (2004). Experimental application of thermosensitive paramagnetic liposomes for monitoring magnetic resonance imaging guided thermal ablation. *Magnetic Resonance in Medicine: Official Journal of the Society of Magnetic Resonance in Medicine / Society of Magnetic Resonance in Medicine*, 52(6):1302–9. PMID: 15562487.

[57] Frich, L., Hagen, G., Brabrand, K., Edwin, B., Mathisen, O., AalÃ¸kken, T. M., and Gladhaug, I. P. (2007). Local tumor progression after radiofrequency ablation of colorectal liver metastases: evaluation of ablative margin and three-dimensional volumetric analysis. *J Vasc Interv Radiol*, 18(9):1134–1140.

[58] Frich, L., Mala, T., and Gladhaug, I. P. (2006). Hepatic radiofrequency ablation using perfusion electrodes in a pig model: effect of the pringle manoeuvre. *Eur J Surg Oncol*, 32(5):527–532.

[59] Gao, L., Heath, D. G., Kuszyk, B. S., and Fishman, E. K. (1996). Automatic liver segmentation technique for three-dimensional visualization of CT data. *Radiology*, 201(2):359–364. PMID: 8888223.

[60] Gerig, G., Jomier, M., and Chakos, M. (2001). Valmet: A new validation tool for assessing and improving 3D object segmentation. In *Lecture Notes in Computer Science (2001)*, volume 2208 of *Lecture Notes in Computer Science*, pages 516–523. Springer.

[61] Goldberg, S. N. and Dupuy, D. E. (2001). Image-guided radiofrequency tumor ablation: challenges and opportunities–part i. *J Vasc Interv Radiol*, 12(9):1021–1032.

[62] Goldberg, S. N., Gazelle, G. S., Compton, C. C., Mueller, P. R., and Tanabe, K. K. (2000). Treatment of intrahepatic malignancy with radiofrequency ablation: radiologic-pathologic correlation. *Cancer*, 88(11):2452–2463.

[63] Goldberg, S. N., Grassi, C. J., Cardella, J. F., Charboneau, J. W., Dodd, G. D., Dupuy, D. E., Gervais, D., Gillams, A. R., Kane, R. A., Lee, F. T., Livraghi, T., McGahan, J., Phillips, D. A., Rhim, H., and Silverman, S. G. (2005). Image-guided tumor ablation: standardization of terminology and reporting criteria. *Radiology*, 235(3):728–739. PMID: 15845798.

[64] Gooch, J. (2005). The dynamics and challenges of interdisciplinary collaboration: a case study of "Cortical depth of bench" in group proposal writing. *Professional Communication, IEEE Transactions on*, 48(2):177–190.

[65] Greene (1996). Hierarchical polygon tiling with coverage masks. In *ACM SIGGRAPH Comp. Graph.*, pages 65–74.

[66] Grimm, S., Bruckner, S., Kanitsar, A., and Gröller, M. E. (2004). Flexible direct multi-volume rendering in interactive scenes. In *Proc. Vision, Modeling, and Visualization*, pages 386–379.

[67] Haemmerich, D. (2004). Hepatic radiofrequency ablation - an overview from an engineering perspective. *Conf Proc IEEE Eng Med Biol Soc*, 7:5433–5436.

[68] Haemmerich, D., Santos, I., Schutt, D. J., Webster, J. G., and Mahvi, D. M. (2006). In vitro measurements of temperature-dependent specific heat of liver tissue. *Medical Engineering & Physics*, 28(2):194–197.

[69] Haemmerich, D. and Webster, J. (2005). Automatic control of finite element models for temperature-controlled radiofrequency ablation. *BioMedical Engineering OnLine*, 4(1).

[70] Haemmerich, D. and Wood, B. J. (2006). Hepatic radiofrequency ablation at low frequencies preferentially heats tumour tissue. *International Journal of Hyperthermia*, 22(7):563–574.

[71] Heimann, T., van Ginneken, B., Styner, M. A., Arzhaeva, Y., Aurich, V., Bauer, C., Beck, A., Becker, C., Beichel, R., Bekes, G., Bello, F., Binnig, G., Bischof, H., Bornik, A., Cashman, P. M. M., Chi, Y., Cordova, A., Dawant, B. M., Fidrich, M., Furst, J. D., Furukawa, D., Grenacher, L., Hornegger, J., KainmÃ$\frac{1}{4}$ller, D., Kitney, R. I., Kobatake, H., Lamecker, H., Lange, T., Lee, J., Lennon, B., Li, R., Li, S., Meinzer, H., Nemeth, G., Raicu, D. S., Rau, A., van Rikxoort, E. M., Rousson, M., Rusko, L., Saddi, K. A., Schmidt, G., Seghers, D., Shimizu, A., Slagmolen, P., Sorantin, E., Soza, G., Susomboon, R., Waite, J. M., Wimmer, A., and Wolf, I. (2009). Comparison and evaluation of methods for liver segmentation from CT datasets. *IEEE Transactions on Medical Imaging*, 28(8):1251–1265. PMID: 19211338.

[72] Hildebrand, P., Leibecke, T., Kleemann, M., Mirow, L., Birth, M., Bruch, H., and BÃ$\frac{1}{4}$rk, C. (2006). Influence of operator experience in radiofrequency ablation of malignant liver tumours on treatment outcome. *European Journal of Surgical Oncology*, 32(4):430–434.

[73] Hou, Q., Zhou, K., and Guo, B. (2008). BSGP: bulk-synchronous GPU programming. *ACM Trans. Graph.*, 27(3):1–12.

[74] Huang, W. and He, K. (2009). A new heuristic algorithm for cuboids packing with no orientation constraints. *Computers & Operations Research*, 36(2):425–432.

[75] Huang, X., Huang, X., Wang, B., Wang, B., Huang, S., Ju, Y., Min, X., and Wang, X. (2007). Registration of different phases of Contrast-Enhanced liver CT data. In *Bioinformatics and Biomedical Engineering, 2007. ICBBE 2007. The 1st International Conference on*, pages 774–777.

[76] Jain, M. K. and Wolf, P. D. (2000). A three-dimensional finite element model of radiofrequency ablation with blood flow and its experimental validation. *Ann Biomed Eng*, 28(9):1075–1084.

[77] Kaebisch, M. (2001). Sprachlogische einheitskonzeptionen der wissenschaft und sprachvielfalt der disziplinen. ueberlegungen zu theoretischen und praktischen ansaetzen von interdisziplinaritaet. In *Interdisciplinaritaet*, pages 13–33. Leipziger Universitaetsverlag GmbH, Leipzig.

[78] Khan, M. A. and Angus, B. M. (1980). Histochemical acitivity of acid phosphatase in rat liver after perfusion fixation. *Acta Anatomica*, 106(3):327–329. PMID: 6769288.

[79] Koestenbauer, S. D. (2010). Forschung in molekular biologie.

[80] Kroeger, T., Altrogge, I., Preusser, T., Pereira, P. L., Schmidt, D., Weihusen, A., and Peitgen, H. O. (2006). Numerical simulation of radio frequency ablation with state dependent material parameters in three space dimensions. In Larson, M. N. R., editor, *Medical Image Computing and Computer-Assisted Intervention*, volume 9 of *LNCS 4191*, pages 380–388, CeVis–Center for Complex Systems and Visualization, University of Bremen, Germany. kroeger@cevis.uni-bremen.de. Springer-Verlag Berlin Heidelberg.

[81] Kruger, J. and Westermann, R. (2003). Acceleration techniques for GPU-based volume rendering. In *Visualization, 2003. VIS 2003. IEEE*, pages 287–292.

[82] Lampe, B., KÃ$\frac{1}{4}$rzl, R., and Hantschmann, P. (1994). Prognostic factors that predict pelvic lymph node metastasis from endometrial carcinoma. *Cancer*, 74(9):2502–2508. PMID: 7923007.

[83] Lange, T., Wenckebach, T. H., Lamecker, H., Seebass, M., HÃ$\frac{1}{4}$nerbein, M., Eulenstein, S., Gebauer, B., and Schlag, P. M. (2005). Registration of different phases of contrast-enhanced CT/MRI data for computer-assisted liver surgery planning: evaluation of state-of-the-art methods. *The International Journal of Medical Robotics + Computer Assisted Surgery: MRCAS*, 1(3):6–20. PMID: 17518386.

[84] Ledergerber, C., Guennebaud, G., Meyer, M., Baecher, M., and Pfister, H. (2008). Volume MLS ray casting. *IEEE Transactions on Visualization and Computer Graphics*, 14(6):1372–1379.

[85] Lee, J. P., Carr, D., Grinstein, G., Kinney, J., and Saffer, J. (2002). The next frontier for bio- and cheminformatics visualization. *IEEE Comput. Graph. Appl.*, 22(5):6–11.

[86] Lencioni, R., Cioni, D., Lera, J., Rocchi, E., Pina, C. D., and Crocetti, L. (2005). Radiofrequency ablation: Principles and technique. In *Focal Liver Lesions*, pages 307–315. Springer-Verlag Berlin Heidelberg.

[87] Levoy, M. (1988). Display of surfaces from volume data. *IEEE Comput. Graph. Appl.*, 8(3):29–37.

[88] Li, W., Mueller, K., and Kaufman, A. (2003). Empty space skipping and occlusion clipping for texture-based volume rendering. In *Proc. IEEE Visualization*, pages 317–324.

[89] Liu, B., Wei, L.-Y., and Xu, Y.-Q. (2006). Multi-layer depth peeling via fragment sort. Technical Report MSR-TR-2006-81, Microsoft Research Asia.

[90] Lobik, L., Leveillee, R. J., and Hoey, M. F. (2005). Geometry and temperature distribution during radiofrequency tissue ablation: an experimental ex vivo model. *J Endourol*, 19(2):242–247.

[91] Lorensen, W. E. and Cline, H. E. (1987). Marching cubes: A high resolution 3D surface construction algorithm. *ACM SIGGRAPH Comput. Graph.*, 21(4):163–169.

[92] Losee, J. (1977). *Wissenschaftstheorie: eine historische EinfÃ¼hrung*. Beck'sche ElementarbÃ¼cher. C.H. Beck, MÃ¼nchen.

[93] Lu, D. S., Raman, S. S., Vodopich, D. J., Wang, M., Sayre, J., and Lassman, C. (2002). Effect of vessel size on creation of hepatic radiofrequency lesions in pigs: assessment of the "heat sink" effect. *AJR Am J Roentgenol*, 178(1):47–51.

[94] Mahr, A., LevegrÃ¼n, S., Bahner, M. L., Kress, J., Zuna, I., and Schlegel, W. (1999). Usability of semiautomatic segmentation algorithms for tumor volume determination. *Investigative Radiology*, 34(2):143–150. PMID: 9951794.

[95] Maleike, D., Nolden, M., Meinzer, H., and Wolf, I. (2009). Interactive segmentation framework of the medical imaging interaction toolkit. *Computer Methods and Programs in Biomedicine*, 96(1):72–83.

[96] Mark, W. R. and Proudfoot, K. (2001). The F-buffer: a rasterization-order FIFO buffer for multi-pass rendering. In *Proc. SIGGRAPH/EUROGRAPHICS workshop on graphics hardware*, pages 57–64.

[97] Marsalek, L., Hauber, A., and Slusallek, P. (2008). High-speed volume ray casting with CUDA. In *Proc. IEEE Symposium on Interactive Ray Tracing*, page 185.

[98] McCreedy, E. S., Cheng, R., Hemler, P. F., Viswanathan, A., Wood, B. J., and Mcauliffe, M. J. (2006). Radio frequency ablation registration, segmentation, and fusion tool. *Information Technology in Biomedicine, IEEE Transactions on*, 10(3):490–496.

[99] McGahan, J. P. and van Raalte, V. A. (2005). History of ablation. In vanSonnenberg, E., McMullen, W., and Solbiati, L., editors, *Tumor Ablation: Principles and Practice*, pages 3–16. Springer Science+Business Media, Inc.

[100] Mehandjiev, N., Layzell, P., Brereton, P., Lewis, G., Mannion, M., and Coallier, F. (2002). Thirteen knights and the seven-headed dragon: an interdisciplinary software engineering framework. In *Software Technology and Engineering Practice, 2002. STEP 2002. Proceedings. 10th International Workshop on*, pages 46–54.

[101] Meyer, C. R., Moffat, B. A., Kuszpit, K. K., Bland, P. L., Mckeever, P. E., Johnson, T. D., Chenevert, T. L., Rehemtulla, A., and Ross, B. D. (2006). A methodology for registration of a histological slide and in vivo MRI volume based on optimizing mutual information. *Molecular Imaging: Official Journal of the Society for Molecular Imaging*, 5(1):16–23. PMID: 16779966.

[102] Miles, K. A., Leggett, D. A., Kelley, B. B., Hayball, M. P., Sinnatamby, R., and Bunce, I. (1998). In vivo assessment of neovascularization of liver metastases using perfusion CT. *The British Journal of Radiology*, 71(843):276–281. PMID: 9616236.

[103] Modersitzki, J., Schmitt, O., and Wirtz, S. (2006). Registration of histological serial sectionings. In *Mathematical Models for Registration and Applications to Medical Imaging*, pages 63–80. Springer Berlin Heidelberg.

[104] Moran, J. (2002). *Interdisciplinarity*. The new critical idiom. Routledge, London.

[105] Morimoto, M., Sugimori, K., Shirato, K., Kokawa, A., Tomita, N., Saito, T., Tanaka, N., Nozawa, A., Hara, M., Sekihara, H., Shimada, H., Imada, T., and Tanaka, K. (2002). Treatment of hepatocellular carcinoma with radiofrequency ablation: Radiologic-histologic correlation during follow-up periods. *Hepatology*, 35(6):1467–1475.

[106] Mulier, S., Ni, Y., Jamart, J., Ruers, T., Marchal, G., and Michel, L. (2005). Local recurrence after hepatic radiofrequency coagulation: multivariate meta-analysis and review of contributing factors. *Ann Surg*, 242(2):158–171.

[107] Munzner, T., Johnson, C., Moorhead, R., Pfister, H., Rheingans, P., and Yoo, T. S. (2006). NIH-NSF visualization research challenges report summary. *IEEE Computer Graphics and Applications*, 26(2):20–24.

[108] Nadeau, D. R. (2000a). Volume scene graphs. In *Proceedings of the 2000 IEEE symposium on Volume visualization*, pages 49–56, Salt Lake City, Utah, United States. ACM.

[109] Nadeau, D. R. (2000b). Volume scene graphs. In *Proc. IEEE symposium on volume visualization*, pages 49–56.

[110] Neumann, R. A., Knobler, R. M., Leonhartsberger, H., BÃ¶hler-Sommeregger, K., and Gebhart, W. (1991). Histochemical evaluation of the coagulation depth after argon laser impact on a port-wine stain. *Lasers in Surgery and Medicine*, 11(6):606–615. PMID: 1753855.

[111] Niessen, W. J., Bouma, C. J., Vincken, K. L., and Viergever, M. A. (1998). Error metrics for quantitative evaluation of medical image segmentation. In *Theoretical Foundations of Computer Vision, TFCV on Performance Characterization in Computer Vision*, pages 275 – 284.

[112] NVIDIA (2008). *NVIDIA CUDA Programming Guide 2.0*. NVIDIA Corporation.

[113] O'Neill, D. P., Peng, T., and Payne, S. J. (2009). A two-equation coupled system model for determination of liver tissue temperature during radio frequency ablation. *Conference Proceedings: ... Annual International Conference of the IEEE Engineering in Medicine and Biology Society. IEEE Engineering in Medicine and Biology Society. Conference*, 2009:3893–3896. PMID: 19963608.

[114] Organ, L. W. (1976). Electrophysiologic principles of radiofrequency lesion making. *Appl Neurophysiol*, 39:69–76.

[115] O'Rourke, A. P., Lazebnik, M., Bertram, J. M., Converse, M. C., Hagness, S. C., Webster, J. G., and Mahvi, D. M. (2007). Dielectric properties of human normal, malignant and cirrhotic liver tissue: in vivo and ex vivo measurements from 0.5 to 20 GHz using a precision open-ended coaxial probe. *Physics in Medicine and Biology*, 52(15):4707–4719. PMID: 17634659.

[116] Oshiro, T., Sinha, U., Lu, D., and Sinha, S. (2002). Reduction of electronic noise from radiofrequency generator during radiofrequency ablation in interventional MRI. *Journal of Computer Assisted Tomography*, 26(2):308–316.

[117] Ou, Y., Shen, D., Feldman, M., Tomaszewski, J., and Davatzikos, C. (2009). Non-rigid registration between histological and MR images of the prostate: A joint segmentation and registration framework. In *Computer Vision and Pattern Recognition Workshop*, pages 125–132, Los Alamitos, CA, USA. IEEE Computer Society.

[118] Ourselin, S., Bardinet, E., Dormont, D., Malandain, G., Roche, A., Ayache, N., TandÃ©, D., Parain, K., and Yelnik, J. (2010). Fusion of histological sections and MR images: Towards the construction of an atlas of the human basal ganglia. In *Medical Image Computing and Computer-Assisted Intervention - MICCAI 2001*, pages 743–751. Springer.

[119] Patidar, S. and Narayanan, P. J. (2008). Ray casting deformable models on the GPU. In *Sixth Indian Conference on Computer Vision, Graphics & Image Processing*, pages 481–488.

[120] Patterson, E. J., Scudamore, C. H., Owen, D. A., Nagy, A. G., and Buczkowski, A. K. (1998). Radiofrequency ablation of porcine liver in vivo: effects of blood flow and treatment time on lesion size. *Annals of Surgery*, 227(4):559–565. PMID: 9563546.

[121] Payne, S. D. (2010). Research in biomedical engineering.

[122] Peng, T., O'Neill, D. P., and Payne, S. J. (2009). 1-D steady state analysis of a two-equation coupled system for determination of tissue temperature in liver during radio frequency ablation. *Conference Proceedings: ... Annual International Conference of the IEEE Engineering in Medicine and Biology Society. IEEE Engineering in Medicine and Biology Society. Conference*, 2009:3385–3388. PMID: 19963799.

[123] Pennes, H. H. (1948). Analysis of tissue and arterial blood temperatures in the resting human forearm. *J Appl Physiol*, 1(2):93–122.

[124] Plate, J., Holtkaemper, T., and Froehlich, B. (2007). A flexible Multi-Volume shader framework for arbitrarily intersecting Multi-Resolution datasets. *IEEE Transactions on Visualization and Computer Graphics*, 13(6):1584–1591.

[125] Pock, T. G., Graz, T. U., Prof, V., Dr, D., and Bischof, H. (2004). *Magisterarbeit Robust Segmentation of Tubular Structures in 3D Volume Data*. TU Graz - ICG.

[126] Portugaller, H. R. P. D. (2010a). Expert interview - 3D histologie.

[127] Portugaller, H. R. P. D. (2010b). Research in medicine - radiology.

[128] Prakash, P., Converse, M. C., Mahvi, D. M., and Webster, J. G. (2006). Measurement of the specific heat capacity of liver phantom. *Physiological Measurement*, 27(10):N41–N46.

[129] Raman, S. S., Lu, D. S., Vodopich, D. J., Sayre, J., and Lassman, C. (2000). Creation of radiofrequency lesions in a porcine model: correlation with sonography, CT, and histopathology. *AJR Am J Roentgenol*, 175(5):1253–1258.

[130] Reinholt, L. E., Burrows, A. M., Eiting, T. P., Dumont, E. R., and Smith, T. D. (2009). Brief communication: histology and micro CT as methods for assessment of facial suture patency. *American Journal of Physical Anthropology*, 138(4):499–506. PMID: 19170212.

[131] Roessler, F., Botchen, R. P., and Ertl, T. (2008). Dynamic shader generation for GPU-based multi-volume ray casting. *IEEE Computer Graphics and Appllications*, 28(5):66–77.

[132] Rossler, F., Botchen, R., and Ertl, T. (2008). Dynamic shader generation for GPU-Based Multi-Volume ray casting. *Computer Graphics and Applications, IEEE*, 28(5):66–77.

[133] Rueckert, D., Sonoda, L. I., Hayes, C., Hill, D. L., Leach, M. O., and Hawkes, D. J. (1999). Nonrigid registration using free-form deformations: application to breast MR images. *IEEE Transactions on Medical Imaging*, 18(8):712–721. PMID: 10534053.

[134] Schmalstieg, D. P. D. (2010). Research in computer graphics.

[135] Schutt, D. J. and Haemmerich, D. (2008). Effects of variation in perfusion rates and of perfusion models in computational models of radio frequency tumor ablation. *Medical Physics*, 35(8):3462–3470. PMID: 18777906 PMCID: 2673648.

[136] Sederberg, T. W. and Parry, S. R. (1986). Free-form deformation of solid geometric models. *ACM SIGGRAPH Computer Graphics*, 20(4):151–160.

[137] Seiler, L., Carmean, D., Sprangle, E., Forsyth, T., Abrash, M., Dubey, P., Junkins, S., Lake, A., Sugerman, J., Cavin, R., Espasa, R., Grochowski, E., Juan, T., and

Hanrahan, P. (2008). Larrabee: a many-core x86 architecture for visual computing. *ACM Trans. Graph.*, 27(3):1–15.

[138] Selle, D., Preim, B., Schenk, A., and Peitgen, H. (2002). Analysis of vasculature for liver surgical planning. *IEEE Transactions on Medical Imaging*, 21(11):1344–1357. PMID: 12575871.

[139] Sheu, T. W. H., Chou, C. W., Tsai, S. F., and Liang, P. C. (2005). Three-dimensional analysis for radio-frequency ablation of liver tumor with blood perfusion effect. *Computer Methods in Biomechanics and Biomedical Engineering*, 8(4):229 – 240.

[140] Soler, L., Delingette, H., Malandain, G., Montagnat, J., Ayache, N., Koehl, C., Dourthe, O., Malassagne, B., Smith, M., Mutter, D., and Marescaux, J. (2001). Fully automatic anatomical, pathological, and functional segmentation from CT scans for hepatic surgery. *Computer Aided Surgery: Official Journal of the International Society for Computer Aided Surgery*, 6(3):131–142. PMID: 11747131.

[141] Stegmaier, S., Strengert, M., Klein, T., and Ertl, T. (2005). A simple and flexible volume rendering framework for graphics-hardware-based raycasting. In *Volume Graphics, 2005. Fourth International Workshop on*, pages 187–241.

[142] Stein, T. (2001). *Untersuchungen zur Dosimetrie der hochfrequenzstrominduzierten interstitiellen Thermotherapie in bipolarer Technik*. Ecomed.

[143] Summers, D. (1987). Dictionary of contemporary english.

[144] Tabar, L. and Dean, P. B. (2003). Mammography and breast cancer: the new era. *International Journal of Gynaecology and Obstetrics: The Official Organ of the International Federation of Gynaecology and Obstetrics*, 82(3):319–326. PMID: 14499978.

[145] Tan, Y., Hua, J., and Dong, M. (2007). FEATURE CURVE-GUIDED VOLUME RECONSTRUCTION FROM 2D IMAGES. In *Biomedical Imaging: From Nano to Macro, 2007. ISBI 2007. 4th IEEE International Symposium on*, pages 716–719.

[146] Termeer, M., Bescós, J. O., and Telea, A. (2006). Preserving sharp edges with volume clipping. In *Proc. Vision, Modeling and Visualization*, pages 341–348.

[147] Thomas, J. J. and Cook, K. A. (2006). A visual analytics agenda. *Computer Graphics and Applications, IEEE*, 26(1):10–13.

[148] TrueGrid (2006). *TrueGrid User's Manual*. TrueGrid, ver. 2.3 edition.

[149] Tsushima, Y., Funabasama, S., Aoki, J., Sanada, S., and Endo, K. (2004). Quantitative perfusion map of malignant liver tumors, created from dynamic computed tomography data. *Academic Radiology*, 11(2):215–223. PMID: 14974597.

[150] Tungjitkusolmun, S., Staelin, S. T., Haemmerich, D., Tsai, J., Cao, H., Webster, J. G., Lee, F. T., Mahvi, D. M., and Vorperian, V. R. (2002). Three-dimensional finite-element analyses for radio-frequency hepatic tumor ablation. *Biomedical Engineering, IEEE Transactions on*, 49(1):3–9.

[151] Unger, M., Pock, T., Trobin, W., Cremers, D., and Bischof, H. (2008). TVSeg - interactive total variation based image segmentation. In *British Machine Vision Conference 2008*, Leeds, Uk.

[152] Villard, C., Baegert, C., Schreck, P., Soler, L., and Gangi, A. (2005a). Optimal trajectories computation within regions of interest for hepatic RFA planning. *Med Image Comput Comput Assist Interv Int Conf Med Image Comput Comput Assist Interv*, 8(Pt 2):49–56.

[153] Villard, C., Soler, L., and Gangi, A. (2005b). Radiofrequency ablation of hepatic tumors: simulation, planning, and contribution of virtual reality and haptics. *Comput Methods Biomech Biomed Engin*, 8(4):215–227.

[154] Villard, C., Soler, L., Papier, N., Agnus, V., Gangi, A., Mutter, D., and Marescaux, J. (2003a). RF-Sim: a treatment planning tool for radiofrequency ablation of hepatic tumors. In *IV '03: Proceedings of the Seventh International Conference on Information Visualization*, Washington, DC, USA. IEEE Computer Society.

[155] Villard, C., Soler, L., Papier, N., Agnus, V., Thery, S., Gangi, A., Mutter, D., and Marescaux, J. (2003b). Virtual radiofrequency ablation of liver tumors. In *Surgery Simulation and Soft Tissue Modeling*, volume LNCS 2673, pages 366–374. Springer.

[156] Ward, M. O. (2002). A taxonomy of glyph placement strategies for multidimensional data visualization. *Information Visualization*, 1(3/4):194–210.

[157] Weihusen, A., Ritter, F., Kroeger, T., Preusser, T., Zidowitz, S., and Pleitgen, H. (2007). Workflow oriented software support for image guided radiofrequency ablation of focal liver malignancies. In *SPIE Symposium on Medical Imaging 2007*, San Diego.

[158] Weiskopf, D., Engel, K., and Ertl, T. (2003). Interactive clipping techniques for texture-based volume visualization and volume shading. *IEEE Transactions on Visualization and Computer Graphics*, 9(3):298–312.

[159] Welp, C., Siebers, S., Ermert, H., and Werner, J. (2006). Investigation of the influence of blood flow rate on large vessel cooling in hepatic radiofrequency ablation. *Biomedizinische Technik. Biomedical Engineering*, 51(5-6):337–346. PMID: 17155870.

[160] Wexler, D., Gritz, L., Enderton, E., and Rice, J. (2005). GPU-accelerated high-quality hidden surface removal. In *Proc. SIGGRAPH/EUROGRAPHICS conference on graphics hardware*, pages 7–14.

[161] Wolf, I., Vetter, M., Wegner, I., BÃ¶ttger, T., Nolden, M., SchÃ¶binger, M., Hastenteufel, M., Kunert, T., and Meinzer, H. (2005). The medical imaging interaction toolkit. *Medical Image Analysis*, 9(6):594–604.

[162] Wright, A. S., Sampson, L. A., Warner, T. F., Mahvi, D. M., and Lee, F. T. (2005). Radiofrequency versus microwave ablation in a hepatic porcine model. *Radiology*, 236(1):132–139. PMID: 15987969.

[163] Wu, Y., Yang, X., and Chan, K. L. (2003). Unsupervised color image segmentation based on gaussian mixture model. In *4th international Conference on Information, Communications, and Signal Processing*, volume 1, pages 541–544.

[164] Wust, P., Gellermann, J., Beier, J., Wegner, S., Tilly, W., TrÃ¶ger, J., Stalling, D., Oswald, H., Hege, H. C., Deuflhard, P., and Felix, R. (1998). Evaluation of segmentation algorithms for generation of patient models in radiofrequency hyperthermia. *Physics in Medicine and Biology*, 43(11):3295–3307. PMID: 9832017.

[165] Yang, D., Converse, M. C., Mahvi, D. M., and Webster, J. G. (2007). Expanding the bioheat equation to include tissue internal water evaporation during heating. *IEEE Transactions on Bio-Medical Engineering*, 54(8):1382–1388. PMID: 17694858.

[166] Yoshimoto, T., Kotoh, K., Horikawa, Y., Kohjima, M., Morizono, S., Yamashita, S., Enjoji, M., and Nakamuta, M. (2007). Decreased portal flow volume increases the area of necrosis caused by radio frequency ablation in pigs. *Liver International: Official Journal of the International Association for the Study of the Liver*, 27(3):368–372. PMID: 17355459.

[167] Yushkevich, P. A., Avants, B. B., Ng, L., Hawrylycz, M., Burstein, P. D., Zhang, H., and Gee, J. G. (2006). 3D mouse brain reconstruction from histology using a Coarse-to-Fine approach. In *Biomedical Image Registration*, volume 4057 of *LNCS*, pages 230–237. Springer-Verlag Berlin Heidelberg.

[168] Zaglmayr, S. D. (2010). Forschung an finiten elementen.

[169] Zahlten, C., JÃ$\frac{1}{4}$rgens, H., Evertsz, C. J., Leppek, R., Peitgen, H. O., and Klose, K. J. (1995). Portal vein reconstruction based on topology. *European Journal of Radiology*, 19(2):96–100. PMID: 7713095.

[170] Zhan, Y., Ou, Y., Feldman, M., Tomaszeweski, J., Davatzikos, C., and Shen, D. (2007). Registering histologic and MR images of prostate for image-based cancer detection. *Academic Radiology*, 14(11):1367–1381. PMID: 17964460.

[171] Zhang, Q., Chung, Y. C., Lewin, J. S., and Duerk, J. L. (1998). A method for simultaneous RF ablation and MRI. *J Magn Reson Imaging*, 8(1):110–114.

[172] ZitovÃ¡, B. and Flusser, J. (2003). Image registration methods: a survey. *Image and Vision Computing*, 21(11):977–1000.